The Optimal Transportation Method in Solid Mechanics

Thesis by

Bo LI

In Partial Fulfillment of the Requirements

for the Degree of

Doctor of Philosophy

California Institute of Technology

Pasadena, California

2009

(Defended May 6th, 2009)

© 2009

Bo LI

All Rights Reserved

To my parents

To Yingying

Acknowledgements

This work would not have been possible without the general support and expert guidance of my advisor, Prof. Michael Ortiz. A few lines are too short to express my deep and sincere gratitude to Michael. His profound knowledge and insightful new ideas are essential to the accomplishment of my graduate study. It has been a great honor and privilege to work with him and I am looking forward to continue listening more to his instructions in the future. I would also like to thank the members of my examining committee, Prof. Guruswami Ravichandran, Prof. Nadia Lapusta and Prof. Chiara Daraio for taking time to read my thesis and for the many help and comments.

My special thanks go to Julian Rimoli, my officemate and best friend in the US since the first day I arrived to Caltech, with whom I shared many nice moments and worked hard together to fulfill our dreams in the US. Many thanks to Tamer El Sayed, Alejandro Mota and Fernando Fraternali, who have acted as mentors for me in many ways. I expect to continue our collaboration and friendship in the future. Many thanks to Marcial Gonzalez and Gabriela Venturini for lots of fruitful and profound discussions about this work. Many thanks also to my colleagues in the Computational Solid Mechanics group: Matias Zielonka, Qiang Yang, Ercan Gürses,

Benjamin Hansen, Leonard Lucas, Feras Habbal, Celia Reina Romo, Daniel Hurtado and Luigi Perotti. A very warm thank you also to Lydia Suarez, Prof. Michael Ortiz's administrative assistant, and Marta Kahl, our computer system administrator, for all their support and encouragement.

Finally, I would like to extend my whole-hearted gratitude to my parents for their unconditional support and encouragement in my whole life, and to Yingying for her love and sincere care, for making my life at Caltech more enjoyable, for helping me in fulfilling my dreams and reminding me what is truly important in my life.

Abstract

This dissertation is concerned with the development of a robust and efficient meshless method, the *Optimal Transportation Method* (OTM), for general solid flows involving extremely large deformation, fast,transient loading and hydrodynamic phenomena. This method is a Lagrangian particle method through an integration of optimal transportation theory with meshless interpolation and material point integrations. The theoretical framework developed in this thesis generalized the Benamou-Brenier differential formulation of optimal transportation problems and leads to a multi-field variational characterization of solid flows, including elasticity, inelasticity, equation of state, and general geometries and boundary conditions. To this end, the accuracy, robustness and versatility of OTM is assessed and demonstrated with convergence and stability test, Taylor anvil test and a series of full three-dimensional simulations of high/hyper-velocity impact examples with the aid of a novel meshless dynamic contact algorithm presented in this thesis.

Contents

List of Figures

Chapter 1

Introduction

1.1 Overview

Over past few decades, conventional grid-based numerical methods such as finite elements, finite volume or finite difference methods have been well developed and successfully applied to a wide variety of boundary value problems in engineering and applied science. However despite the numerical advantages and great success, grid-based methods suffer from some inherent difficulties in many aspects when used for the analysis of problems of practical engineering interests, for instance the metal forming processes such as extrusion and molding, and high/hyper-velocity impact problems.

In grid-based numerical methods, mesh generation or discretization for the problem domain is a prerequisite for the numerical simulation. Based on the fundamental frames for describing the physical governing equations,i.e.,the Lagrangian description and the Eulerian description, there are two disparate kinds of grid of domain discretization: the Lagrangian grid and the Eulerian grid.

Most structural dynamics codes are Lagrangian, where the grid is embedded with

the material, consequently deforms together with the material. Lagrangian methods offer several advantages over the competition, see Herrmann [19]. But because of the grid distortion, the Lagrange codes face a lot of problems for large deformations and contact/impact problems. The severe distorted elements lead to serious problems: slow convergence, inaccurate results and even premature termination. In addition, the time step is based on the size of the smallest element in the grid, when the element size tends to zero, the time step tends to zero and may lead to the breakdown of the computation. The most general technique to overcome these problems is remeshing. However to obtain a good mesh in three dimensions for a complex geometry may be very tedious and time consuming, sometimes even impossible to implement. On the other hand the remeshing involves overlaying of a new, undistorted mesh on the old, distorted mesh, so that the follow-up computation can be performed on the new, undistorted mesh. The physical properties in the new mesh are approximated from the old mesh, which will introduce diffusion and error. Especially for the problems involving fast, transient loading, frequent remeshing turns out to be necessary to keep the simulation running in a Lagrangian code.

One of the alternative methods is the Eulerian code, in which the grid is fixed in space and with time, large deformations in the object do not cause any deformations in the mesh itself. But to use the Eulerian methods in solid flows, the fixed grid leads to many disadvantages. First of all, it is very difficult to analyze the time history of field variables at a fixed point on the material. Second since the Eulerian methods track the mass, momentum and energy flux across the mesh cell boundaries, the position of

free surfaces, deformable boundaries, and moving material interfaces are difficult to be determined accurately. Finally a complicated mesh generation procedure to convert the irregular geometry of problem domain into a regular computational domain is usually necessary; sometimes expensive numerical mapping is required.

All the difficulties and limitations listed above of the grid-based methods is because of the mesh. Recent strong interest has been focused on the development of the next generation of computational methods–meshless methods. The objective of meshless methods is to eliminate at least part of the reliance on a mesh by constructing the approximation entirely in terms of nodes. Some superior features of meshless methods to the conventional grid-based methods for many applications are

i) They can easily handle extremely large deformations because of the absence of a mesh. No mesh generation, no mesh distortion, no mesh alignment sensitivity and no remeshing during the calculation are necessary. *h-adaptivity* is comparably simple as only nodes have to be added. *p-adaptivity* is also conceptionally simpler than in mesh-based methods,since the support of the shape functions can be adjusted at run time.

ii) The shape functions may easily be constructed to have any desired order of continuity.

iii) Convergence results of the meshless methods are often considerably better than the results obtained by mesh-based shape functions.

iv) Volumetric locking may be alleviated by tuning the dilation parameters of the

kernel functions.

A number of meshless techniques has been proposed so far. The starting point, which seems to have the longest continuous history is the smooth particle hydrodynamics (SPH) method introduced by Lucy in 1977 [33],who used it for modeling astrophysical phenomena without boundaries such as exploding stars and dust clouds. Of late, various improvements of SPH have been developed through the years to fulfill the completeness of the shape functions and remove the so-called tensile instability first identified by Swelege [50], see section §2.1.1.

In comparison to SPH, a parallel but distinctly different path to constructing meshless approximations is the use of moving least square (MLS) approximations. The MLS technique was first introduced and studied by Lancaster and Salkauskas [27] in curve and surface fitting, and then in Solid Mechanics taken by Nayroles et al. [37] in the Diffuse Element Method (DEM) in a Galerkin form. Belytschko et al. [8] modified DEM and substantiated it with supportive examples from solid mechanics and heat conduction to call their implementation the Element-Free Galerkin (EFG) method. This class of method is consistent and has been applied to a wide range of problems in solid mechanics, with particular emphasis in the area of computational fracture mechanics. An improvement of the continuous SPH approximation by Liu et al. [32] is the so-called Reproducing Kernel Particle Method (RKPM). In order to increase the order of completeness of the SPH approximation, a correction function is introduced into the approximation. However the RKPM technique,although starting from a very different point, turns to be an equivalent procedure with the same result

as the MLS concept since the RKPM and EFG approximants are almost identical. Duarte and Oden [14] and Babuška and Melenk [3] recognize that these methods are specific instances of partition of unity (PU). A significant contribution to the mathematical structure and the understanding of meshless methods was put forth by these authors.Then the H-p clouds method [14] was proposed by Oden et al. In H-p clouds, local approximation spaces are constructed by multiplying a partition of unity by polynomials or other classes of functions,which offers great flexibility in the choice of local nodal basis functions that can be used to capture special properties of the partial differential equations.

Tow other paths in the evolution of meshless methods have been the development of generalized finite difference methods [39, 30] and particle in-cell methods [49]. Some excellent reviews on the meshless and particle methods can be found in the papers by Belytschko et al. [7],Li and Liu [29] and Huerta et al. [20].

Nevertheless most of the meshless approximations mentioned above may not be called interpolants since they do not verify the *Kronecker delta* property. In other words, the nodal parameters are not the nodal values approximated from the meshless shape functions. Consequently the meshless shape funtions associated with nodes located on the interior of the domain do not typically vanish on the boundary. This issue leads to complex imposition of essential boundary conditions and the application of point loads. An excellent paper discussing the various options for imposing essential boundary consitions with meshless methods is provided by Huerta et al. [20]. Arroyo and Ortiz [2] proposed the *local maximum-entropy approximation schemes*

(LME), which bridges continuously important limits: Delaunay triangulation [41] and maximum-entropy statistical inference [45]. The authors showed the LME approximation have a *weak Kronecker delta* property at the boundary. Thus imposing linear essential boundary conditions can be done as in finite elements. This appears to be a simple and elegant means to impose essential boundary conditions in meshless methods. More attractive advantages of the LME approximation will be discussed in §2.2.

Another important issue in the style of meshless Galerkin methods is the evaluation of integrals in the weak form. Absence of a mesh leads to difficulty for evaluating the numerical integrations. Several possibilities have been investigated in the literature: (1) Nodal integration [4]. To obtain the discrete form of the functional or the free energy, only the nodal fields are considered, but usually it results in the instability due to rank deficiency, and tensile instability for the usage of Eulerian kernels as well; (2) stress point integration [15, 43]. Field values are evaluated at additional stress points as extra integration points beside the nodes. The instability appears for Eulerian kernel functions; also rules have to be found to move the stress points and recalculate the weights at run time; (3) background mesh. A, not necessary regular, background mesh can be used to compute the integrals. However, in spite of large number of quadrature points needed to be evaluated in the course of computation, a significant source of error, the misalignment of the supports of the basis functions and the integration cells would induce numerical integration errors and affect the accuracy and convergence of meshless methods [13].

In this thesis we propose the *Optimal Transportation* method, which is a Galerkin particle method. By employing the *local max-ent approximation schemes* recently proposed by Arroyo and Ortiz [2], the *Optimal Transportation* method overcomes the two main barriers blocking the development of the meshless methods, i.e., the imposition of essential boundary conditions and numerical integration of the Galerkin weak form.

The aim of the present work is to develop Lagrangian scheme for the simulation of solid flows with extremely large deformation, fluid flows and fluid/solid coupled problems through an integration of optimal transportation theory (cf. [53] for a review) with meshless interpolation and material point integrations. The theoretical framework developed in this thesis generalized the Benamou-Brenier [9] differential formulation of optimal transportation problems and leads to a multifield variational characterization of solid flows, including inelasticity, equation of state, and general geometries in $\mathbb{R}^d$ and boundary conditions. The governing variational principle lends itself ideally to discretization by a combination of conforming interpolation of the velocity field and pointwise sampling of the local material state. The Euler's equation of motion for the solid flows may be verified as a gradient flow of a free energy proposed in §3.2 with respect to the optimal transportation structure. Hence a time discrete, iterative variational scheme whose solutions converge to the solution of the Euler's equation of motion can be constructed by following the strategy used by Jordan et al. [24]. The spatial discretization of the semi-discrete action is carried over by the insertion of material points into the semi-discrete Euler-Lagrange equation.

Then a fully discrete action for computations can be obtained. The used of meshless interpolation for the conforming interpolation of the velocity field is particularly attractive. We specifically use the *local max-ent approximation*. These shape functions reconstruct the velocity field from nodal values that are most local and least biased in an informational-theoretical sense. The interpolation of the fields is then inserted directly into the action, resulting in a discrete action in the sense of Rayleigh-Ritz. This confers the discretization scheme robust convergence properties.

1.2 Thesis Outline

A brief outline of this dissertation is as follows. In chapter 2, some of the most common approximations used for meshless methods are described and examined. The essential elements of the shape functions and their drawbacks are investigated. Particular emphasis is put on the construction of the *local max-ent approximation schemes*. An efficient and robust solution procedure is presented and some of its attractive advantages are outlined.

Chapter 3 briefly reviews the optimal transportation theory and the computational fluid mechanics solution to the Monge-Kantorovich mass transfer problem. A free energy functional is proposed such that the Euler's equation of motion of elastic solid flows can be recast in the formalism of gradient flows with respect to the optimal transportation differential structure. Further the Euler-Lagrange equations associated with the action is verified to be identical to the Euler's equations of motion and continuity equations. The time discretization is conducted following the strategy

in Optimal Transportation framework and the spatial discretization is carried over by insertion of material points. For inelastic solid flows, the variational structure introduced by Radovitzky and Ortiz [40] is adopted, and the total discrete action is constructed by replacing the free energy density for elastic solid flows by the incremental effective energy density. Algorithms for solving elastic and inelastic flows are proposed.

In chapter 4, we study the rate of convergence of the *Optimal transportation* method by a verification example with exact solution. An isothermal compressive shock wave problem is simulated in one, two and three dimensions. We compared the numerical results to the explicit solution obtained in [40]. By refinement of the nodal space in one dimension, we can obtain the rate of convergence of the velocity field and density field in the shock wave. In addition, stability is always an issue for meshless methods. A brief description of the von Neumann stability analysis in meshless method proposed by Betschko et al. [5] is given. Based on their statement, the stability of the *Optimal Transportation* method can be analyzed and one-dimensional elastic bar tension/compression test is employed to show the stability of our new meshless method.

Chapter 5 focuses on the application of the *Optimal Transportation* method for general solid flows with extremely large deformations. First the effectiveness and accuracy of the *Optimal Transportation* method for highly nonlinear inelastic solid flows is exhibited by investigating the standard Taylor anvil-impact benchmark example. A fully three-dimensional simulation is carried up to 80μs and an excellent agree-

ment between the numerical results from the method and Finite Element Method is obtained. Finally the capability of the *Optimal Transportation* method for handling problems involving fast, transient loading, hydrodynamic phenomena such as high/hyper velocity impact is showed by a series of three-dimensional (3D) numerical simulations. A novel meshless contact algorithm is proposed for the simulation of high/hyper-velocity impacts. By using the *Optimal Transportation* method with our new meshless contact algorithm, a test of an elastoplastic long-rod penetrator into an elastic-plastic plate without any erosion of material is simulated in a totally 3D meshless style, and the relationship between the Depth of Penetration and impact velocity of a deformable high velocity steel sphere into an elastic-plastic aluminum plate is studied by a series of totally 3D meshless simulations.

In chapter 6, a conclusion of some of the main results obtained in this work and contributions is presented, with some concluding remarks on the potential and promise of the *Optimal Transportation* method in Solid Mechanics.

Chapter 2

Local Maximum-Entropy Approximation

A multitude of different meshless methods has been published during the last three decades. Despite the variety of names of individual methods, there are significant similarities between many of these methods, and the major difference may be how to construct the approximation of a single function $u(\mathbf{x})$ in the domain based on a set of scattered nodes. In this chapter, the most common approximations used for meshless methods will be described and examined. Particular emphasis is put on the *local max-ent approximation scheme* (LME), an efficient and robust solution procedure is presented for the local max-ent shape funtions. Further the advantages of LME are outlined.

2.1 Meshless Approximations

2.1.1 Smooth Particle Hydrodynamics (SPH)

Smooth Particle hydrodynamics (SPH) introduced by Lucy [33] in 1977 and Gingold and Monaghan [18] is one of the earliest particle methods. The basic idea is to approximate a function $\mathbf{u}(\mathbf{x})$ on domain Ω by a convolution

$$\mathbf{u}_h(\mathbf{x}) = \int_\Omega C_\rho \phi(\frac{\mathbf{x}-\mathbf{y}}{\rho})\mathbf{u}(\mathbf{y})d\mathbf{y}\,, \tag{2.1}$$

where $\mathbf{u}_h$ is the approximation of $\mathbf{u}$, ϕ is a compactly supported function, usually called a *window function* or *weight* and *kernel function* and ρ is the so-called *dilation parameter*. C_ρ is a normalization constant such that

$$\int_\Omega C_\rho \phi(\frac{\mathbf{y}}{\rho})d\mathbf{y} = 1\,, \tag{2.2}$$

which is also called as the normality property of the window function. The discrete SPH form may be obtained using numerical quadratures

$$\mathbf{u}_h(\mathbf{x}) = \sum_a C_\rho \phi(\frac{\mathbf{x}-\mathbf{x}_a}{\rho})\mathbf{u}_a\omega_a\,, \tag{2.3}$$

where $\mathbf{x}_a$ and ω_a are the points or so-called particles in SPH and weights of the numerical quadrature, $\mathbf{u}_a \equiv \mathbf{u}(\mathbf{x}_a)$ is the value of the original function at particle $\mathbf{x}_a$.

We define the discrete window function as

$$w(\mathbf{x}-\mathbf{x}_a,\rho) = C_\rho \phi(\frac{\mathbf{x}-\mathbf{x}_a}{\rho})\,. \tag{2.4}$$

Therefore, the SPH meshless approximation can be defined as

$$\mathbf{u}_h(\mathbf{x}) = \sum_a N_a(\mathbf{x})\mathbf{u}_a\,, \tag{2.5}$$

with the approximation basis $N_a(\mathbf{x}) = w(\mathbf{x}-\mathbf{x}_a,\rho)\omega_a$.

The window function plays an important role in such meshless methods. According to Monaghan [35] the window function is required to satisfy the following conditions:

i) $w(\mathbf{x}-\mathbf{x}_a,\rho) > 0 \quad$ on a subdomain of $\Omega, \Omega_a\,,$ (2.6a)

ii) $w(\mathbf{x}-\mathbf{x}_a,\rho) = 0 \quad$ outside of the subdomain $\Omega_a\,,$ (2.6b)

iii) $w(\mathbf{x}-\mathbf{x}_a,\rho) \to \delta(\mathbf{x}-\mathbf{x}_a)$ the Dirac delta function, $\quad$ as $h \to 0\,,$ (2.6c)

iv) $w(\mathbf{x}-\mathbf{x}_a,\rho)$ is a monotonically decreasing function w.r.t. $||\mathbf{x}-\mathbf{x}_a||\,.$ (2.6d)

Three commonly used window functions are the cubic spline, Gaussian and quartic spline, for example, the window functions can be written as a function of the normalized radius r, where let $d_a = ||\mathbf{x}-\mathbf{x}_a||$ and $r = d_a/d_a^{\max}$ with $d_a^{\max}$ defined as the size

of the support of the ath particle,

$$\text{cubic spline:} \quad w(r) = \begin{cases} \frac{2}{3} - 4r^2 + 4r^3 & \text{for } r \leq \frac{1}{2} \\ \frac{4}{3} - 4r + 4r^2 - \frac{4}{3}r^3 & \text{for } \frac{1}{2} < r \leq 1 \\ 0 & \text{for } r > 1 \end{cases} \tag{2.7a}$$

$$\text{Gaussian:} \quad w(r) = \begin{cases} \frac{\exp(-(\alpha r)^2) - \exp(-\alpha^2)}{1 - \exp(-\alpha^2)} & \text{for } r \leq 1 \\ 0 & \text{for } r > 1 \end{cases} \tag{2.7b}$$

$$\text{quartic spline:} \quad w(r) = \begin{cases} 1 - 6r^2 + 8r^3 - 3r^4 & \text{for } r \leq 1 \\ 0 & \text{for } r > 1 \end{cases} \tag{2.7c}$$

It is evidenced easily while the continuous form of SPH meshless approximation is *zeroth-order* complete, and most kernel functions satisfy higher order consistency condition, the discrete SPH form cannot even reproduce constant fields, and hence is not a partition of unity. The following are the conditions for *zeroth-order* and *first-order completeness*

$$\sum_a N_a(\mathbf{x}) = 1\,, \tag{2.8a}$$

$$\sum_a N_a(\mathbf{x})\mathbf{x}_a = \mathbf{x}\,. \tag{2.8b}$$

Completeness or consistency is generally necessary for convergence, which directly contributes to the interpolation error. The later usually dictates the error between the exact solution and the numerical solution. Furthermore, the lack of consistency of

the interpolant is also one of the sources of the tensile instability in SPH method. Thus corrections must be made to the kernel functions for the convergence and accuracy of SPH method. Various improvements of SPH have been developed through the years to fulfill the completeness, which includes Monaghan's symmetrization [36] on derivative approximation, Johnson-Beissel correction[22], Randles-Libersky correction [42], and Krongauz-Belytschko correction [6]. However, so far most of the analysis related to the convergence, stability and accuracy properties of SPH are based on uniformly distributed particles, and sometimes only for one-dimensional cases, the results obtained by such analysis are often limited to idealized circumstances. For more general cases, especially those with large deformations and impulsive loadings where the particles are usually highly disordered, the obtained results may not always be reliable, as it is not yet very clear how the particle irregularity affects the accuracy of the solutions, especially in three dimension.

On the other hand, in general, the SPH approximation $\mathbf{u}_h(\mathbf{x}_a) \neq \mathbf{u}_a$,that means the shape functions are not interpolants, and they do not verify the *Kronecker delta property*

$$N_a(\mathbf{x}_b) \neq \delta_{ab}\,. \tag{2.9}$$

Thus special techniques are needed to impose essential boundary conditions and the application of point loads,which is critical for the use of meshless method in Solid Mechanics and the performance of computation.

2.1.2 Moving Least Squares (MLS)

The objective of the Moving Least Squares (MLS) is to obtain an approximation based on an array of nodes in the domain under consideration, but with high accuracy and high order of completeness. The MLS method was first introduced and studied by Lancaster and Salkauskas [27] in curve and surface fitting, and then in Solid Mechanics employed by Nayroles et al. [37] in the diffuse element method. Further studies and applications are made in the Element-Free Galerkin (EFG) methods by Belytschko et al. [8]. The basic idea of the MLS approach is to approximate $\mathbf{u}(\mathbf{x})$ through a polynomial of order m with nonconstant coefficients in the domain Ω,i.e.,

$$\mathbf{u}_h(\mathbf{x}) = \sum_i^m p_i(\mathbf{x}) a_i(\mathbf{x}) = \mathbf{p}^T(\mathbf{x})\mathbf{a}(\mathbf{x})\,, \tag{2.10}$$

where $p_0(\mathbf{x}) = 1$ and $p_i(\mathbf{x})$ are monomials in the space coordinates $\mathbf{x} = (x_1, \cdots, x_d)^T$ in $\mathbb{R}^d$ so that the basis is complete. For instance, in one dimension, a complete polynomial of order m

$$\mathbf{p}(x) = (1, \quad x, \quad x^2, \quad \cdots, \quad x^m)^T\,, \tag{2.11}$$

and $\mathbf{a}(x)$ is given by

$$\mathbf{a}(x) = \big(a_0(x), \quad a_1(x), \quad a_2(x), \quad \cdots, \quad a_m(x)\big)^T\,, \tag{2.12}$$

where the unknown parameters $a_i(x)$ at any given point are determined by minimizing the difference or a weighted discrete L_2 norm between the local approximation at that point and the nodal parameters $\mathbf{u}_I$ as follows

$$\begin{aligned} J &= \sum_I^n w(\mathbf{x}-\mathbf{x}_I)\big(\mathbf{u}_h(\mathbf{x}_I)-\mathbf{u}_I\big)^2 \\ &= \sum_I^n w(\mathbf{x}-\mathbf{x}_I)\big(\mathbf{p}^T(\mathbf{x}_I)\mathbf{a}(\mathbf{x})-\mathbf{u}_I\big)^2 , \end{aligned} \tag{2.13}$$

where $w(\mathbf{x}-\mathbf{x}_I)$ is a weight or window function with compact support as mentioned in SPH methods, n is the number of nodes in the neighborhood of $\mathbf{x}$ for which the weight function $w(\mathbf{x}-\mathbf{x}_I) \neq 0$, and $\mathbf{u}_I$ it the nodal value of $\mathbf{u}$ at $\mathbf{x}=\mathbf{x}_I$. The stationarity of J in equation (2.13) with respect to $\mathbf{a}(\mathbf{x})$ leads to the following linear relation between $\mathbf{a}(\mathbf{x})$ and $\mathbf{u}_I$

$$\mathbf{a}(\mathbf{x}) = \mathbf{A}^{-1}(\mathbf{x})\mathbf{B}(\mathbf{x})\mathbf{u}\,, \tag{2.14}$$

where

$$\mathbf{A}(\mathbf{x}) = \sum_I^n w_I(\mathbf{x})\mathbf{p}(\mathbf{x})\otimes\mathbf{p}(\mathbf{x})\,, \tag{2.15a}$$

$$\mathbf{B}(\mathbf{x}) = [w_1(\mathbf{x})\mathbf{p}(\mathbf{x}_1), \quad w_2(\mathbf{x})\mathbf{p}(\mathbf{x}_2), \quad \cdots, \quad w_n(\mathbf{x})\mathbf{p}(\mathbf{x}_n)]^T\,, \tag{2.15b}$$

$$\mathbf{u} = [\mathbf{u}_1, \quad \mathbf{u}_2, \quad \cdots, \quad \mathbf{u}_n]^T\,. \tag{2.15c}$$

Hence the approximation $\mathbf{u}_h(\mathbf{x})$ can be expressed as

$$\mathbf{u}_h(\mathbf{x}) = \sum_{I}^{n} N_I(\mathbf{x})\mathbf{u}_I \,, \tag{2.16}$$

where the shape function associated with node I at the point $\mathbf{x}$ is

$$N_I(\mathbf{x}) = \sum_{i}^{m} p_i(\mathbf{x})(\mathbf{A}^{-1}(\mathbf{x})\mathbf{B}(\mathbf{x}))_{iI} \,. \tag{2.17}$$

It has been shown that the MLS approximation exactly reproduces all the polynomials in $\mathbf{p}(\mathbf{x})$,that means the consistency of order m is satisfied by the MLS approximation if the basis is complete in the polynomials of order m. One of the major disadvantage of EFG is the efficiency. In order to obtain an accurate shape function and compute the inverse of matrix A,the number of nodes in the influence domain is usually much greater than the number of monomials in the polynomial basis.Especially in two and three dimensions, it becomes a bottleneck in performance. It should be noted that MLS does not satisfy the Kronecker delta criterion neither,therefore they are not interpolants. Consequently the nodal parameters $\mathbf{u}_I$ are not the nodal values of $\mathbf{u}_h(\mathbf{x}_I)$, the approximation on the boundary of the domain may depend on the nodal data of interior nodes. Again this property makes the imposition of essential boundary conditions more complicated than with finite elements.

2.1.3 Reproducing Kernel Particle Method (RKPM)

The Reproducing Kernel Particle Method (RKPM) by Liu et al. [32] is an improvement of the continuous SPH approximation. In order to increase the order of completeness of the approximation, a correction function $C(\mathbf{x}, \mathbf{y})$ is introduced into the approximation (2.1)

$$\mathbf{u}_h(\mathbf{x}) = \int_\Omega C(\mathbf{x}, \mathbf{y}) w(\mathbf{x} - \mathbf{y}, \rho) \mathbf{u}(\mathbf{y}) d\mathbf{y} \,, \tag{2.18}$$

where $K(\mathbf{x}, \mathbf{y}) = C(\mathbf{x}, \mathbf{y}) w(\mathbf{x} - \mathbf{y}, \rho)$ is defined such that the approximation is mth order consistent. Suppose $\mathbf{p}(\mathbf{x})$ is a complete array of monomials up to mth order, any mth order polynomials can be written as

$$\mathbf{u}(\mathbf{x}) = \mathbf{p}^T(\mathbf{x}) \mathbf{a} \,, \tag{2.19}$$

where $\mathbf{a}$ are unknown coefficients, then

$$\int_\Omega \mathbf{p}(\mathbf{y}) w(\mathbf{x} - \mathbf{y}, \rho) \mathbf{u}(\mathbf{y}) d\mathbf{y} = \big(\int_\Omega \mathbf{p}(\mathbf{y}) \mathbf{p}^T(\mathbf{y}) w(\mathbf{x} - \mathbf{y}, \rho) d\mathbf{y} \big) \mathbf{a} \,, \tag{2.20}$$

which is a system of equations for $\mathbf{a}$, can then be substituted back into the approximation $\mathbf{u}_h(\mathbf{x}) = \mathbf{p}^T(\mathbf{x})\mathbf{a}$, which yields

$$\mathbf{u}_h(\mathbf{x}) = \mathbf{p}^T(\mathbf{x}) \big(\int_\Omega \mathbf{p}(\mathbf{y}) \mathbf{p}^T(\mathbf{y}) w(\mathbf{x} - \mathbf{y}, \rho) d\mathbf{y} \big)^{-1} \int_\Omega \mathbf{p}(\mathbf{y}) w(\mathbf{x} - \mathbf{y}, \rho) \mathbf{u}(\mathbf{y}) d\mathbf{y} \,. \tag{2.21}$$

Thus the correction function can be obtained as

$$C(\mathbf{x},\mathbf{y}) = \mathbf{p}^T(\mathbf{x})\Big(\int_\Omega \mathbf{p}(\mathbf{y})\mathbf{p}^T(\mathbf{y})w(\mathbf{x}-\mathbf{y},\rho)d\mathbf{y}\Big)^{-1}\mathbf{p}(\mathbf{y}) = \mathbf{p}^T(\mathbf{x})\big(\mathbf{M}(\mathbf{x})\big)^{-1}\mathbf{p}(\mathbf{y})\,. \tag{2.22}$$

The discrete version of the RKPM approximation is given by evaluating the continuous expression at the numerical quadrature points,i.e.,

$$\begin{aligned}\mathbf{u}_h(\mathbf{x}) &= \sum_I^N C(\mathbf{x},\mathbf{x}_I)w(\mathbf{x}-\mathbf{x}_I,\rho)\mathbf{u}_I\omega_I \\ &= \mathbf{p}^T(\mathbf{x})\big(\mathbf{M}(\mathbf{x})\big)^{-1}\sum_I \mathbf{p}(\mathbf{x}_I)w(\mathbf{x}-\mathbf{x}_I,\rho)\mathbf{u}_I\omega_I\,.\end{aligned} \tag{2.23}$$

Numerical integration is also required to evaluate the moment matrix $\mathbf{M}(\mathbf{x})$

$$\begin{aligned}\mathbf{M}(\mathbf{x}) &= \int_\Omega w(\mathbf{x}-\mathbf{y},\rho)\mathbf{p}(\mathbf{y})\mathbf{p}^T(\mathbf{y})d\mathbf{y} \\ &= \sum_I^N w(\mathbf{x}-\mathbf{x}_I,\rho)\mathbf{p}(\mathbf{x}_I)\mathbf{p}^T(\mathbf{x}_I)\omega_I\,.\end{aligned} \tag{2.24}$$

Although the RKPM approximation can reproduce exactly mth order polynomials with a complete basis, therefore it is mth order consistent, due to the discretization procedure the so-called amplitude and phase error terms (APETs) [31] are introduced. The reproducing conditions and the criterion to derive the correction function are different from that of the continuous system, differing in the APETs. For the general case, the APETs decrease as the dilatation parameter increases, but the APETs cannot be eliminated from the reproducing precess. Another error term arises in the higher-order polynomial reproduction. This error is introduced by the higher-order

derivatives and is proportional to the dilatation. This means that a larger dilatation parameter will cause higher reproduction errors, while the APETs decrease. Analogously to the MLS approximation, it does not verify the Kronecker delta property either and thus special techniques are needed to impose essential boundary conditions.

2.2 Local Max-Ent Approximation Schemes (LME)

The Local Max-Ent approximation scheme (LME) has been developed by Arroyo and Ortiz [2], which represents a compromise between unbiased statistical inference, in the sense of information theory, and the desire to define shape functions of the least width. The resulting shape functions are non-negative, possess a *weak Kronecker-delta property* at the boundary, and reduce in the limit to piecewise affine interpolation over a Delaunay triangulation, whereas away from this limit the shape functions are smooth and analogous to those employed in MLS schemes.

2.2.1 Convex approximation

The approximation schemes are entirely defined by the node set and fall into the general class of *convex approximation schemes.*Consider a set of distinct nodes $X = \{\mathbf{x}_a, a = 1, \cdots, N\} \subset \mathbb{R}^d$,to be referred to as a node set, the convex hull of X is the set

$$\mathrm{conv}X = \{\mathbf{x} \in \mathbb{R}^d | \mathbf{x} = \sum_{a=1}^{N} \lambda_a \mathbf{x}_a, \lambda_a \in \mathbb{R}^+, \sum_{a=1}^{N} \lambda_a = 1\}, \tag{2.25}$$

where λ_a is the coefficients of convex combinations.For a real function $u(\mathbf{x}) : \text{conv}X \rightarrow \mathbb{R}$, the numerical approximation for $u(\mathbf{x})$ is written as

$$u(\mathbf{x}) = \sum_{a=1}^{N} p_a(\mathbf{x}) u_a \,, \tag{2.26}$$

where u_a is the known function values on the node set X,and $p_a : \text{conv}X \rightarrow \mathbb{R}$ will be the shape functions we are trying to construct. To guarantee the affine functions are exactly reproduced, the zeroth- and first-order consistency conditions may be enforced as constraints to the desired shape functions,i.e.,

$$\sum_{a=1}^{N} p_a(\mathbf{x}) = 1 \quad \forall \mathbf{x} \in \text{conv}X \,, \tag{2.27a}$$

$$\sum_{a=1}^{N} p_a(\mathbf{x}) \mathbf{x}_a = \mathbf{x} \quad \forall \mathbf{x} \in \text{conv}X \,. \tag{2.27b}$$

Furthermore, if the shape functions are required to be non-negative,

$$p_a(\mathbf{x}) \geq 0 \quad \forall \mathbf{x} \in \text{conv}X \,. \tag{2.28}$$

Then the shape functions may be interpreted as the coefficients of convex combinations in (2.25).In view of these constrains or properties, $u(\mathbf{x}) = \sum_{a=1}^{N} p_a(\mathbf{x}) u_a$ with $p_a \in \mathbb{P}(X)$ defined a general framework referred to as *convex approximation scheme*, where the domain of p_a,or feasible set,is

$$\mathbb{P}(X) = \{p_a \in \mathbb{R}^+ | \sum_{a=1}^{N} p_a(\mathbf{x}) = 1, \sum_{a=1}^{N} p_a(\mathbf{x}) \mathbf{x}_a = \mathbf{x}\} \,. \tag{2.29}$$

In [2],Arroyo and Ortiz have proved the feasible set $\mathbb{P}(X)$ is non-empty if and only if $\mathbf{x} \in \text{conv}X$, and if F is a face of conv$X$ and $\mathbf{x}_a \in F$,then $p_a = 0$ on F. A distinct advantage of this general convex approximation scheme over MLS and other meshless approximation is remarked by Arroyo and Ortiz [2] as the *weak Kronecker-delta property*, that is

$$p_a(\mathbf{x}_b) = \delta_{ab} \quad \mathbf{x}_a \in \text{vertex set of conv}X\,, \tag{2.30}$$

which greatly facilitates the imposition of essential boundary conditions, i.e., the boundary conditions can be simply applied to the boundary nodes like the way in Finite Element Method.

2.2.2 Maximum-Entropy approximation

In information theory, Shannon [45] introduced the notion of entropy as a measure of uncertainty,the Shannon entropy of a discrete probability distribution is

$$H(A) = H(p_1, \cdots, p_n) = -\sum_{a=1}^{N} p_a \log p_a, \tag{2.31}$$

with the extension by continuity:$0 \log 0 = 0$, where A is the set of events and the associated probabilities

$$A = \begin{pmatrix} A_1 & A_2 & \cdots & A_n \\ p_1 & p_2 & \cdots & p_n \end{pmatrix}. \tag{2.32}$$

The function $H(A)$ is non-negative,symmetric,continuous,and strictly concave and possesses a number of properties that are expected of a measure of uncertainty. In particular, $H(A) = 0$ if and only if one of the probabilities is one and all the others are zero,and attains its maximum for the probabilities $p_1 = p_2 = \cdots = p_n = 1/n$,which may be regarded as the most uncertain or random distribution.Furthermore $H(p_1, p_2, \cdots, p_n, 0) = H(p_1, p_2, \cdots, p_n)$, that means adding an impossible event does not change the level of uncertainty.

According to Jaynes' principle of maximum entropy [21], the least-biased probability distribution is that which maximizes entropy subject to all known constraints. Thus, from a purely information-theoretical viewpoint, the optimal, or least biased, convex approximation schemes are solutions of the program:

$$\begin{aligned} \text{(MaxEnt)} \quad \text{maximize:} \quad & H(p_1, \cdots, p_N) = -\sum_{a=1}^{N} p_a \log p_a \,, \\ \text{subject to} \quad & p_a \geq 0, \quad a = 1, \cdots, N \,, \\ & \sum_{a=1}^{N} p_a = 1 \,, \\ & \sum_{a=1}^{N} p_a \mathbf{x}_a = \mathbf{x} \,. \end{aligned} \tag{2.33}$$

In one-dimensional case this problem gives the *max-ent* solution of the classical problem of moments. Examples of max-ent schemes in the plane are shown in Figure 2.1. Figure 2.1(a) shows a max-ent shape function for a point set consisting of the vertices of a convex pentagon, which illustrates the *Kronecker delta property* of the max-ent shape functions, and the property that the restriction of the max-ent shape functions

to the edges of the pentagon is linear. Thus, max-ent approximation schemes provide a basis for construction conforming elements in the shape of arbitrary convex polyhedra. Figure 2.1(b) shows the max-ent shape function of an interior node for a larger node set. As expected, the shape function vanishes at the boundary.

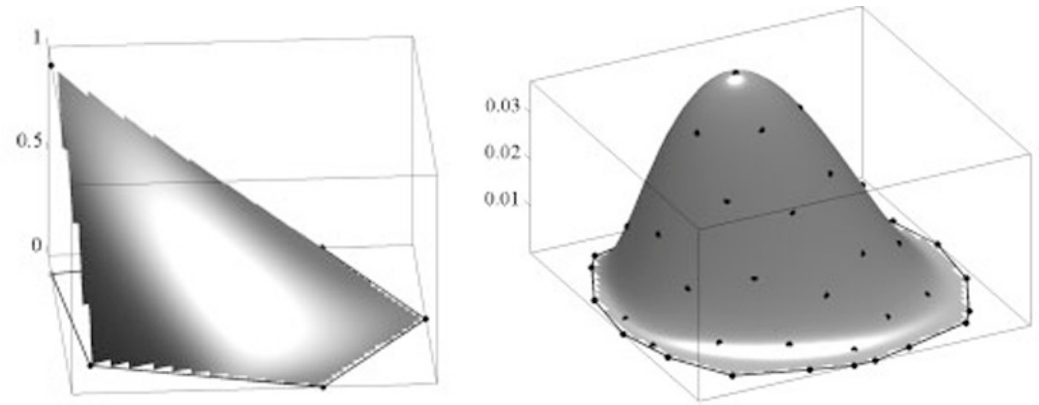

(a) shape function for the vertex of a pentagon

(b) shape function for an interior node

Figure 2.1: Examples of *Max-Ent* approximation schemes in the plane.

2.2.3 Local Max-Ent approximation as a Pareto set

However, the support of the max-ent shape function introduced in preceding section is highly non-local and extends to the entire convex hull of the nodes set.In addition the value of the shape function at its corresponding node differs greatly from unity. Consequently the max-ent approximation is far from interpolating in the interior and results in a very poor fit to the data as illustrated in Figure 2.2. Thus control over the degree of locality of max-ent approximation schemes is required, that is the degree to which the value of a function at $\mathbf{x}$ is correlated to nearby nodal values. Correspondingly, the control of the width of the shape functions and their decay with

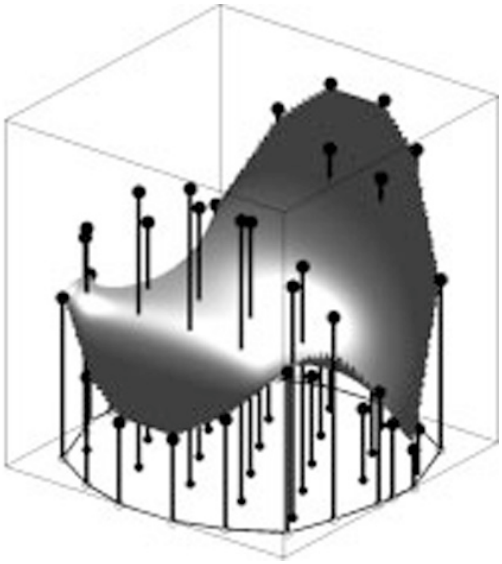

Figure 2.2: *Max-Ent* approximation from scattered data.

distance away from their corresponding nodes is desired. In [2], Arroyo and Ortiz defined the width of a shape function p_a as

$$w(p_a) = \int_\Omega p_a(\mathbf{x})|\mathbf{x} - \mathbf{x}_a|^2 d\mathbf{x}\,, \tag{2.34}$$

where Ω is the conv$X$. Thus the most local approximation scheme is now that which minimizes the total width of the shape functions

$$W(p_1, \cdots, p_N) = \sum_{a=1}^{N} w(p_a) = \int_\Omega \sum_{a=1}^{N} p_a(\mathbf{x})|\mathbf{x} - \mathbf{x}_a|^2 d\mathbf{x}\,, \tag{2.35}$$

subject to the constrains in (2.33). Since functional (2.35) does not involve shape function derivatives, its minimization can be performed point wise, this results in the

Rajan's optimization problem for the *Delaunay triangulation* [41].

$$\begin{aligned} \text{(RAJ) For fixed } \mathbf{x} \text{ minimize} \quad & U(\mathbf{x}, p_1, \cdots, p_N) = \sum_{a=1}^{N} p_a |\mathbf{x} - \mathbf{x}_a|^2 \,, \\ \text{subject to} \quad & p_a \geq 0, \quad a = 1, \cdots, N \,, \\ & \sum_{a=1}^{N} p_a = 1 \,, \\ & \sum_{a=1}^{N} p_a \mathbf{x}_a = \mathbf{x} \,. \end{aligned} \tag{2.36}$$

Rajan showed that if the nodes are in general positions, then (RAJ) has a unique solution corresponding to the piecewise affine shape functions supported by the unique Delaunay triangulation associated with the node set X. (RAJ) may be referred to the convex approximation scheme as *Rajan convex approximation schemes*, and the approximants corresponding to the piecewise affine shape functions supported by a Delaunay triangulation as *Delaunay convex approximants*. Therefore, Rajan's result states that for nodes in general positions, the Delaunay convex approximation scheme coincides with the unique Rajan convex approximation scheme, that is optimal in the sense of the width (2.34).

Thus far there are criteria for selecting convex approximation schemes:maximum entropy and maximum locality. But in general the entropy maximization and total width minimization are competing objective functions. A standard device for harmonizing such competing objectives is to seek a *Pareto optima*, which results in the

definition of the *Local max-ent approximation scheme*,

$$\text{(LME) For fixed } \mathbf{x} \text{ minimize}: \quad f_\beta(\mathbf{x},\mathbf{p}) \equiv \beta \sum_{a=1}^{N} p_a |\mathbf{x}-\mathbf{x}_a|^2 + \sum_{a=1}^{N} p_a \log p_a \quad , \tag{2.37a}$$

$$\text{subject to}: \; p_a \geq 0, \quad a = 1,\ldots,N\,, \tag{2.37b}$$

$$\sum_{a=1}^{N} p_a = 1\,, \tag{2.37c}$$

$$\sum_{a=1}^{N} p_a \mathbf{x}_a = \mathbf{x}\,. \tag{2.37d}$$

where $\mathbf{p} = (p_1,\ldots,p_N)^T$ is the vector of shape functions, and $\beta \in (0,+\infty)$ is Pareto optimal. (LME) can be viewed as optimal trade-offs or compromises between information-theoretical optimality and locality. When $\beta \to +\infty$, Rajan's problem is obtained, and $\beta = 0$ recovers the max-ent approximation.Since for $\beta \in [0,+\infty)$ the function $f_\beta(\mathbf{x},\mathbf{p})$ is continuous and strictly convex in $\mathbb{P}(X)$, an argument identical to that in the general convex optimization class shows that (LME) has a unique solution $\mathbf{p}(\mathbf{x})$ if and only if $\mathbf{x} \in \text{conv}X$.

The local max-ent approximation scheme possesses most of the desirable properties for convex approximation scheme, and exhibits some attractive advantages:

i) LME verifies the *weak Kronecker delta property* and zeroth- and first-order consistency. Figure 2.3(a) shows the behavior of the Local Max-Ent shape functions at the boundary of the domain. At the vertex, the shape functions

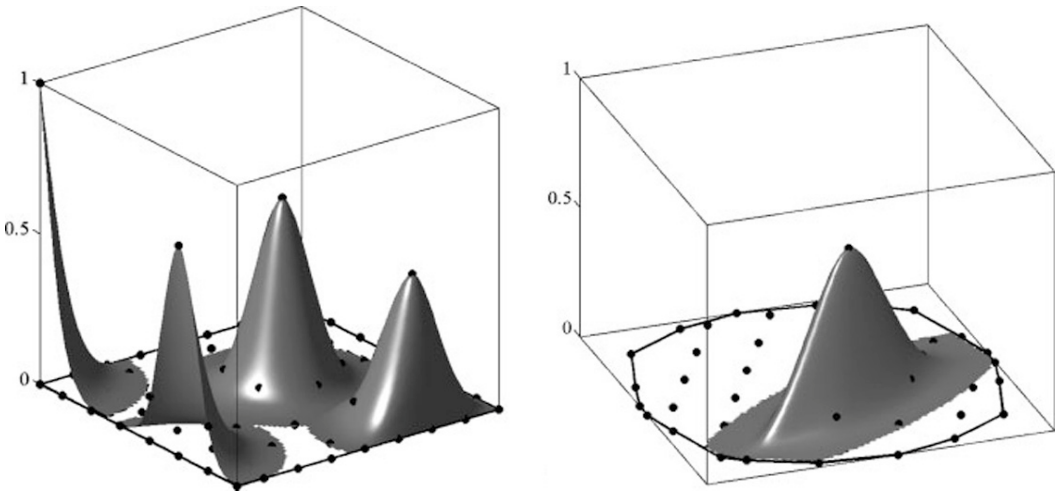

(a) Behavior of the Local Max-Ent shape functions at the boundary

(b) Example of anisotropic Local Max-Ent shape functions

Figure 2.3: Examples of the Local Max-Ent shape functions at the boundary of the domain.

satisfy the Kronecker delta property, and the interior shape functions have zero contribution on the boundary unlike the MLS approximation scheme.

ii) Locality of the shape functions introduces a seamless bridge between Finite Element shape functions and meshless approximations. The parameter β determines the support-width of the shape functions. In addition, it can be allowed to depend on position and adjusted adaptively in order to achieve varying degrees of locality, which gives great advantage for its use in solid and fluid interaction problems and extremely large deformation problems. Figure 2.4 shows the Local Max-Ent shape function and its partial derivatives for a node in a two-dimensional node set as a function of the dimensionless parameter $\gamma = \beta h^2$, where h is a measure of the nodal spacing and β is constant over the domain. It can be seen from this figure that the shape functions are smooth and their degree of locality is controlled by the parameter γ. For the maximum value of

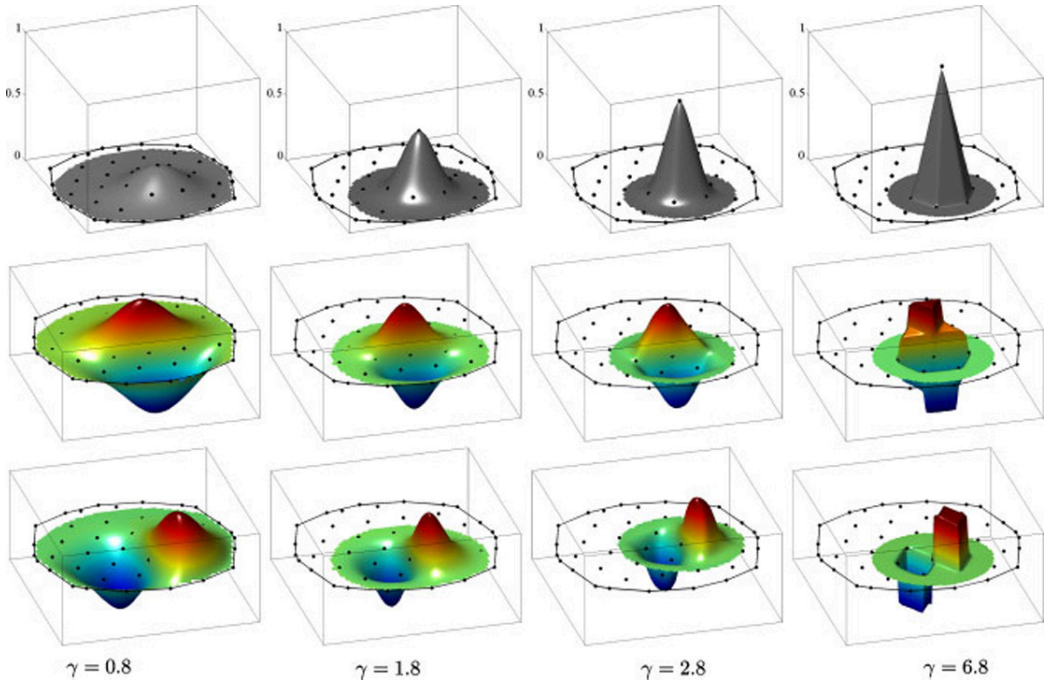

Figure 2.4: Example of *the Local Max-Ent* shape functions for a two-dimensional arrangement of nodes, and spacial derivatives (arbitrary scale) for several values of $\gamma = \beta h^2$.

$\gamma = 6.8$ shown in the figure the shape function ostensibly coincides with the Delaunay shape function.

iii) It is simple for the construction of anisotropic shape functions and high-order approximations.Different choice of measure of locality gives greater flexibility in the construction of new approximants. For example in figure 2.3(b), an anisotropic shape function is defined using an Euclidian distance of the form $d(\mathbf{x}, \mathbf{y}) = \sqrt{(\mathbf{x} - \mathbf{y}) \cdot G(\mathbf{x} - \mathbf{y})}$ for a constant metric tensor G. It is noted by Sukumar and Wright [48] that $f_\beta(\mathbf{p}, \mathbf{x})$ is identical to the relative entropy functional proposed in [26, 46], if a Gaussian (RBF) prior distribution, $m_a(\mathbf{x}) = \exp(-\beta|\mathbf{x} - \mathbf{x}_a|^2)$ is used. The authors also introduced a general way to extend the max-ent approximation scheme to high order by employing a generalization

of the Shannon-Jaynes entropy [47].

iv) Efficient procedure for calculating the shape functions is proposed. In practice, the evaluation of the local max-ent approximants at a given point $\mathbf{x} \in \text{conv}X$ does not require the solution of the (LME) as a constrained convex program involving N unknowns. In next section, we will show it is sufficient to solve an unconstrained minimization problem effectively, and the shape functions and derivatives will be the auxiliary outputs of the computation. On the other hand, the shape function will decay as $\exp(-\beta|\mathbf{x} - \mathbf{x}_a|^2)$, consequently only a small number of nodes contribute to the partition function, which greatly reduces the cost of the solution procedure.

2.2.4 Dual problem and computation of the shape functions

In principle, the problem (LME) is solved by the conventional Lagrange multipliers method. In this section, we will introduce a very effective approach for computing the shape functions and their spatial derivatives. On using shifted nodal coordinates $\mathbf{y}_a = \mathbf{x}_a - \mathbf{x}$ and using the zeroth-order consistency constrain (2.37c), it is possible to rewrite the first-order consistency condition (2.37d) as

$$\sum_{a=1}^{N} p_a(\mathbf{x}_a - \mathbf{x}) \equiv \sum_{a=1}^{N} p_a \mathbf{y}_a = 0\,. \tag{2.38}$$

This choice is more efficient and stable in numerical computations than the conditions appear in (LME). By introducing the Lagrange multipliers $\boldsymbol{\lambda} \in \Re^d$ and $\mu \in \Re$, the

Lagrangian $\mathcal{L} : \Re^N \times \Re \times \Re^d \mapsto \Re$ associated with the (LME) takes the form

$$\mathcal{L}(\mathbf{p}, \mu, \boldsymbol{\lambda}) = f_\beta(\mathbf{p}) + \mu(\sum_{a=1}^{N} p_a - 1) + \boldsymbol{\lambda} \cdot \sum_{a=1}^{N} p_a \mathbf{y}_a \,. \tag{2.39}$$

Now the Lagrange multipliers are ready to be determined by standard duality analysis, which also provide a practical way for calculating the shape functions. The first-order necessary conditions for the existence of Lagrange multipliers $\boldsymbol{\lambda}$ and μ, or the KKT conditions are

$$\frac{\partial \mathcal{L}}{\partial p_a}(p_a^*, \boldsymbol{\lambda}^*, \mu^*) = 0 \,, \tag{2.40a}$$

$$\sum_{a=1}^{N} p_a^* = 1 \,, \tag{2.40b}$$

$$\sum_{a=1}^{N} p_a^* \mathbf{x}_a = \mathbf{x} \,, \tag{2.40c}$$

for $\mathbf{x} \in \text{int}(\text{conv}X)$, where p_a^* is the solution for (LME), $\boldsymbol{\lambda}^*$ and μ^* are the optimal Lagrange parameters. From equation (2.39), by using conditions (2.40b) and (2.40c), the explicit expression for equation (2.40a) can be written as

$$0 = \beta |\mathbf{x} - \mathbf{x}_a|^2 + \log(p_a^*) + 1 + \mu^* + \boldsymbol{\lambda}^* \cdot (\mathbf{x}_a - \mathbf{x}) \quad a = 1, \ldots, N \,, \tag{2.41}$$

from which we obtain the solution of (LME) as

$$p_a^*(\mathbf{x}) = \frac{Z_a(\mathbf{x}, \boldsymbol{\lambda}^*)}{\exp(\mu^* + 1)} \,, \tag{2.42}$$

where

$$Z_a(\mathbf{x}, \boldsymbol{\lambda}) = \exp[-\beta|\mathbf{x} - \mathbf{x}_a|^2 + \boldsymbol{\lambda} \cdot (\mathbf{x} - \mathbf{x}_a)]\,, \tag{2.43}$$

and $Z(\mathbf{x}, \boldsymbol{\lambda}) = \sum_{a=1}^{N} Z_a(\mathbf{x}, \boldsymbol{\lambda})$ is known as the partition function in statistical mechanics. The Lagrange dual function of the primal problem (2.37) is given by

$$g(\mu, \boldsymbol{\lambda}) = \inf_{p_a \in \Re^+} \mathcal{L}(\mathbf{p}, \mu, \boldsymbol{\lambda}) = -\mu - \exp(-\mu - 1) \sum_{a=1}^{N} \exp[-\beta|\mathbf{x} - \mathbf{x}_a|^2 + \boldsymbol{\lambda} \cdot (\mathbf{x} - \mathbf{x}_a)]\,, \tag{2.44}$$

and the dual problem is

$$\max_{\{\boldsymbol{\lambda} \in \Re^d, \mu \in \Re\}} g(\mu, \boldsymbol{\lambda})\,. \tag{2.45}$$

The optimal Lagrange parameters $\boldsymbol{\lambda}^*$ and μ^* can be obtained as the solution of (2.45), and the Slater condition tells us the dual gap is zero. We can simplify the dual function by maximizing over the dual variable μ analytically. For fixed $\boldsymbol{\lambda}$, the objective function is maximized when the derivative with respect to μ equals zero, which gives

$$\mu^* = \log \sum_{a=1}^{N} \exp[-\beta|\mathbf{x} - \mathbf{x}_a|^2 + \boldsymbol{\lambda} \cdot (\mathbf{x} - \mathbf{x}_a)] - 1 \quad \text{or} \quad \log Z(\mathbf{x}, \boldsymbol{\lambda}) = \mu^* + 1\,. \tag{2.46}$$

Substituting this optimal value of μ back into the dual problem gives the reduced Lagrange dual problem,

$$\min_{\boldsymbol{\lambda} \in \Re^d} \log Z(\mathbf{x}, \boldsymbol{\lambda})\,, \tag{2.47}$$

which is an unconstrained geometric program (in a convex form), the function $F(\boldsymbol{\lambda}) \equiv \log Z(\mathbf{x}, \boldsymbol{\lambda})$ for fixed $\mathbf{x}$ is also introduced as a "potential" function for determining

the Lagrange parameters $\boldsymbol{\lambda}$. Convex optimization algorithms are suitable for computing these basis functions. Here we use a modified Newton-Raphson method. The stationary of the potential F requires its derivative equals zero,i.e.,for fixed $\mathbf{x}$

$$\mathbf{r}(\mathbf{x}, \boldsymbol{\lambda}) = \nabla_{\boldsymbol{\lambda}} F(\boldsymbol{\lambda}) = \sum_{a=1}^{N} \frac{1}{Z} \frac{\partial Z_a}{\partial \boldsymbol{\lambda}} = \sum_{a=1}^{N} p_a(\mathbf{x} - \mathbf{x}_a) = 0\,, \tag{2.48}$$

where we have used the equation (2.42) and the identity (2.46).

Suppose $\boldsymbol{\lambda}^k$ is the solution for equation (2.48) at the kth iteration, the update for the Lagrange multipliers is

$$\boldsymbol{\lambda}^{k+1} = \boldsymbol{\lambda}^k + \alpha^k \Delta\boldsymbol{\lambda}^k\,, \tag{2.49}$$

where α^k and $\Delta\boldsymbol{\lambda}^k$ are the step length and the descent direction at step k respectively. For the Newton-Raphson method usually the direction is chosen as

$$\Delta\boldsymbol{\lambda}^k = -(\mathbf{J}^{-1})^k \mathbf{r}^k\,, \tag{2.50}$$

where $\mathbf{J}$ is the Hessian matrix of F,for fixed $\mathbf{x}$,

$$\mathbf{J}(\mathbf{x}, \boldsymbol{\lambda}) = \nabla^2_{\boldsymbol{\lambda}} F(\boldsymbol{\lambda}) = \sum_{a=1}^{N} \frac{\partial p_a}{\partial \boldsymbol{\lambda}}\Big|_{\mathbf{x}} \otimes (\mathbf{x} - \mathbf{x}_a) = \sum_{a=1}^{N} p_a(\mathbf{x} - \mathbf{x}_a) \otimes (\mathbf{x} - \mathbf{x}_a) - \mathbf{r} \otimes \mathbf{r}\,. \tag{2.51}$$

Furthermore, the exact line search is used, in which α is chosen to minimize F along the ray $\{\boldsymbol{\lambda} + \alpha\Delta\boldsymbol{\lambda} | \alpha \geq 0\}$ or the exact step length is

$$\hat{\alpha} = \arg\min_{\alpha \in \Re^+} F(\boldsymbol{\lambda} + \alpha\Delta\boldsymbol{\lambda})\,. \tag{2.52}$$

The necessary condition for the minimization problem (2.52) takes the form

$$\sum_{a=1}^{N} c_a \hat{p}_a = 0\,, \tag{2.53}$$

where

$$c_a = \Delta\boldsymbol{\lambda} \cdot (\mathbf{x} - \mathbf{x}_a)\,, \tag{2.54a}$$

$$\hat{p}_a = \frac{\hat{Z}_a}{\hat{Z}}, \quad \text{where } \hat{Z}_a = \exp[-\beta|\mathbf{x} - \mathbf{x}_a|^2 + (\boldsymbol{\lambda} + \hat{\alpha}\Delta\boldsymbol{\lambda}) \cdot (\mathbf{x} - \mathbf{x}_a)]\,, \tag{2.54b}$$

$$\hat{Z} = \sum_{a=1}^{N} \hat{Z}_a\,. \tag{2.54c}$$

A line search (bisection or golden section search) is suitable to find the solution of equation (2.53). Since the step length is non-negative, the initial guess of the left end for bisection algorithm should be chosen as $\alpha = 0$. To illustrate the effectiveness of the modified Newton-Raphson method to solve equation (2.48) , the average number of iterations required for convergence with the criterion $||r(\mathbf{x}, \lambda_k)|| < Tol_{NR}$ is presented in table 2.1 for different values of γ and different tolerances. The node set of figure 2.4 is used in this example, and the fine grid of sample points used to generate these plots is used to compute the average. It is observed that, for a tolerance of 10^{-5}, between 2 and 3 iterations are sufficient over a broad range of values of the thermalization parameter β.As the athermal limit is reached (for large values of γ), the Newton-Raphson method needs more iterations for convergence. Nevertheless, F is asymptotically linear as $||\boldsymbol{\lambda}|| \to \infty$, and therefore the Hessian matrix becomes singular. In practice, at such situation a steepest descent method is convenient to lead

Table 2.1: Average number of Newton-Raphson iterations per sample point

γ	10^{-5}	10^{-10}	Machine precision
0.8	2.7	3.6	4.2
1.8	2.4	3.5	4.3
2.8	3.0	4.0	5.0
6.8	4.0	5.0	6.0

the solution out of the asymptotic region. That means we need to choose the search direction $\Delta\boldsymbol{\lambda} = -\mathbf{r}$. Again the exact line search is involved, but with the direction of the gradient of the potential F. Note that in the course of computing the Lagrange parameters, the shape functions are the auxiliary outputs. The explicit form of the derivatives of the shape functions with respect to the spatial coordinates $\mathbf{x}$ is given in reference [2] for a general $\beta(\mathbf{x})$. If β is constant, the remarkably simple expression,

$$\nabla p_a(\mathbf{x}) = -p_a \mathbf{J}^{-1}(\mathbf{x} - \mathbf{x}_a)\,, \tag{2.55}$$

is obtained as a special case,where no summation on a. By the principle for high-performance numerical computations, *using what you have*, we note that the derivative for a constant β can be simply calculated with the information output from the computation of the Lagrange multipliers.

Chapter 3

The Optimal Transportation Method (OTM)

In this chapter, the theoretical framework for the *Optimal Transportation Method* is developed by generalizing the Benamou-Brenier differential formulation of optimal transportation problems and leads to a multifield variational characterization of solid flows, including elasticity and inelasticity, equation of state, and general geometries in $\mathbb{R}^d$ and boundary conditions. We review the computational fluid mechanics solution to the optimal mass transfer problem and extend the structure to general solid flows.

3.1 The Mass Transportation Problem

The *Monge-Kantorovich* optimal transportation problem originally can be stated as follows: given two distributions with equal masses of a given material $g_0(x)$, $g_1(x)$,find a transport map ψ which carries the first distribution into the second and minimizes the transport cost

$$C(\psi) := \int_X |x - \psi(x)| g_0(x) dx \,. \tag{3.1}$$

The condition that the first distribution of mass is carried into the second can be written as

$$\int_{\psi^{-1}(b)} g_0(x)dx = \int_B g_1(y)dy \quad \forall B \subset X \ Borel\,, \tag{3.2}$$

or,by the change of variables formula, as

$$g_1(\psi(x))|\det\nabla\psi(x)| = g_0(x)\,. \tag{3.3}$$

More generally one can replace the functions g_0, g_1 by positive measures ρ_0, ρ_1 with equal mass, so that (3.2) reads $\rho_1 = \psi_\sharp\rho_0$, and replace the euclidean distance by a generic cost function $c(x, y)$, studying the problem

$$\min_{\psi_\sharp\rho_0=\rho_1} \int_X c(x, \psi(x))d\rho_0(x)\,, \tag{3.4}$$

where the infimum of the transport problem leads also to a c-dependent distance between measures with equal mass, known as *Kantorovich-Wasserstein* distance.

The optimal transport problem and the Kantorovich-Wasserstein distance have a very broad range of applications, for instance, Fluid Mechanics,Partial Differential Equations and Optimization. We begin by introducing a "Computational Fluid Mechanics"(CFM) type formulation for the MKP, considering the case of the motion of a fluid of non-interacting particles, which provides the simplest framework for discussing the connection between optimal transportation and the Lagrangian dynamics of a continuous distribution of mass. In particular, we draw on the theory of optimal transportation, specific aspects of which are summarized in §3.1.1, to formulate the

kinetic energy of the system and, by extension, its action directly in terms of its mass density. This defines a minimum principle whose minimizers are the time histories of the mass density. In §3.1.3 and §3.1.4, we also address matters of temporal and spatial discretization for the simple case of flows of non-interacting particles. These discretization schemes are extended to general solid flows in subsequent sections.

3.1.1 Computational fluid mechanics solution to the Monge-Kantorovich mass transfer

In this section we summarize the relevant aspects of the theory of optimal transportation that are required for subsequent developments. Optimal transportation theory derives its importance from the fact that it supplies a powerful and useful mathematical foundation for a number of areas of mechanics and physics. A thorough and rigorous account of the theory may be found, e.g., in the monographs of Evans [17] and Villani [53]. For simplicity, here and subsequently we formally use mass densities in lieu of more rigorous measure-theoretical notation, which is nevertheless evident from the expressions and can be found in the above-referenced monographs.

We begin by considering the flow of an inviscid fluid of non-interacting particles in $\mathbb{R}^n$ at zero temperature. The motion of the fluid over a time interval $[a, b]$ is governed by the coupled equations

$$\frac{\partial \rho}{\partial t} + \nabla \cdot (\rho \mathbf{v}) = 0 \,, \tag{3.5a}$$

$$\frac{\partial (\rho \mathbf{v})}{\partial t} + \nabla \cdot (\rho \mathbf{v} \otimes \mathbf{v}) = 0 \,, \tag{3.5b}$$

where ρ is the mass density of the fluid and $\mathbf{v}$ is the velocity field. Equation (3.5a) is the equation of conservation of mass and equation (3.5b) is the equation of conservation of linear momentum. We assume that the fluid has finite total mass

$$M = \int \rho dx, \tag{3.6}$$

and that mass does not "leak to infinity", i.e.,

$$\lim_{R\to\infty} \int_{\partial B_R} \rho \mathbf{v} \cdot n dx = 0\,, \tag{3.7}$$

where B_R is the ball of radius R. It then follows the total mass M the fluid remains unchanged through the flow. Indeed,

$$\dot{M} = \lim_{R\to\infty} \int_{B_R} \frac{\partial \rho}{\partial t} dx = -\lim_{R\to\infty} \int_{B_R} \nabla \cdot (\rho \mathbf{v}) dx = -\lim_{R\to\infty} \int_{\partial B_R} \rho \mathbf{v} \cdot n dx = 0\,. \tag{3.8}$$

Suppose that, in addition, we specify the initial and final mass densities, namely,

$$\rho(\mathbf{x}, a) = \rho_a(\mathbf{x})\,, \tag{3.9a}$$

$$\rho(\mathbf{x}, b) = \rho_b(\mathbf{x})\,. \tag{3.9b}$$

The problem thus becomes a *transportation problem* of finding the flow that transports the initial mass density ρ_a to the final one ρ_b.

The transportation problem just enunciated can be recast as an *optimal transportation* problem. Thus, Benamou and Brenier [9] noted that problem (3.5, 3.9)

admits the variational characterization:

$$\inf_{(\rho,\mathbf{v})\in X} A(\rho,\mathbf{v})\,, \tag{3.10a}$$

$$\text{subject to: } \frac{\partial\rho}{\partial t} + \nabla\cdot(\rho\mathbf{v}) = 0\,, \tag{3.10b}$$

where

$$A(\rho,\mathbf{v}) = \int_a^b K(\rho,\mathbf{v})\,dt \tag{3.11}$$

is the action over the time interval (a,b),

$$K(\rho,\mathbf{v}) = \int \frac{\rho}{2}|\mathbf{v}|^2\,dx \tag{3.12}$$

is the kinetic energy and the natural space of solutions is $X = \{(\rho,\mathbf{v}) \in C\big([a,b];L^1(\mathbb{R}^n;[0,\infty))\big)$ $\times\, C\big([a,b];L^2(\mathbb{R}^n;\mathbb{R}^n)\big)\}$. We recall that $L^1(\mathbb{R}^n)$ Lebesgue space of integrable functions over $\mathbb{R}^n$. Thus $\{d\mu = \rho\,dx,\ \rho \in L^1(\mathbb{R}^n;[0,\infty))\}$ is the set of measures that are absolutely continuous with respect to the Lebesgue measure. Physically, the restriction of ρ to $L^1(\mathbb{R}^n;[0,\infty))\big)$ ensures that every subset of $\mathbb{R}^n$ with a well-defined volume can be assigned a well-defined non-negative mass. In addition, $L^2(\mathbb{R}^n;\mathbb{R}^n)$ is the Lebesgue space of square-integrable vector-valued functions over $\mathbb{R}^n$. Physically, restriction of $\mathbf{v}$ to $L^2(\mathbb{R}^n;\mathbb{R}^n)$, in conjunction with the restriction of ρ to $L^1(\mathbb{R}^n;[0,\infty))$, ensures that the velocity fields have finite kinetic energy. Finally, $C\big([a,b];L^1(\mathbb{R}^n;[0,\infty))\big)$ and $C\big([a,b];L^2(\mathbb{R}^n;\mathbb{R}^n)\big)$ are the space of time-continuous functions taking values in $L^1(\mathbb{R}^n;[0,\infty))$ and $L^2(\mathbb{R}^n;\mathbb{R}^n)$, respectively.

We may formally verify that the minimization problem (3.10) is indeed equivalent to (3.5), (3.9). To this end, we enforce the constraint (3.5b) by means of a Lagrange multiplier, which leads to the extended action

$$A(\rho, \mathbf{v}, \phi) = \int_a^b \left\{ \int \left[\frac{\rho}{2} |\mathbf{v}|^2 + \big(\rho_{,t} + \nabla \cdot (\rho \mathbf{v})\big)\phi \right] dx \right\} dt \,, \tag{3.13}$$

where ϕ is the Lagrange multiplier. Stationary of A demands that

$$\begin{aligned} 0 = \delta A(\rho, \mathbf{v}, \phi) = \int_a^b \left\{ \int \left[\frac{\delta\rho}{2} |\mathbf{v}|^2 + \big(\delta\rho_{,t} + \nabla \cdot (\delta\rho \mathbf{v})\big)\phi \right] dx \right\} dt + \\ \int_a^b \left\{ \int \left[\big(\rho \mathbf{v} \cdot \delta\mathbf{v} + \nabla \cdot (\rho \delta\mathbf{v})\phi\big) \right] dx \right\} dt + \int_a^b \left\{ \int \left[\big(\rho_{,t} + \nabla \cdot (\rho\mathbf{v})\big)\delta\phi \right] dx \right\} dt \,. \end{aligned} \tag{3.14}$$

Integrating by parts with the aid of (3.7) and requiring stationarity with respect to all admissible variations we obtain

$$\frac{1}{2}|\mathbf{v}|^2 - \phi_{,t} - \nabla\phi \cdot \mathbf{v} = 0 \,, \tag{3.15a}$$

$$\rho\mathbf{v} - \rho\nabla\phi = 0 \,, \tag{3.15b}$$

$$\frac{\partial\rho}{\partial t} + \nabla \cdot (\rho\mathbf{v}) = 0 \,. \tag{3.15c}$$

The third of these equations is the continuity equation (3.5b). In addition, from (3.15b) it follows that

$$\mathbf{v} = \nabla\phi \quad \text{in } \operatorname{supp}\rho \,. \tag{3.16}$$

Thus, the stationary points of the action (3.13) correspond to potential flow. Using

(3.16), (3.15a) simplifies to

$$\frac{\partial \phi}{\partial t} + \frac{1}{2}|\mathbf{v}|^2 = 0\,. \tag{3.17}$$

Taking gradients, multiplying by ρ and using (3.15c) and (3.16) we obtain (3.5b), as required.

The Benamou and Brenier [9] variational characterization (3.10) of the transport problem (3.5), (3.9) admits a compelling reformulation within the context of the Monge-Kantorovich optimal transportation framework. Specifically Benamou and Brenier ([9], cf. also [53]) showed that the minimizers of the action (3.11) are given in terms of McCann's *displacement interpolation* [53]

$$\varphi(\mathbf{x}, t) = \frac{b-t}{b-a}\,\mathbf{x} + \frac{t-a}{b-a}\,T(\mathbf{x})\,, \tag{3.18}$$

through the relations

$$\mathbf{v}(\mathbf{x}, t) = \frac{\partial \varphi}{\partial t}(\varphi^{-1}(\mathbf{x}, t), t)\,, \tag{3.19a}$$

$$\rho(\mathbf{x}, t) = \rho_a\big(\varphi^{-1}(\mathbf{x}, t)\big) / \det\big(\nabla \varphi(\varphi^{-1}(\mathbf{x}, t), t)\big)\,, \tag{3.19b}$$

where $T = \varphi(\cdot, b)$ is the optimal transference mass of ρ_a into ρ_b in the sense of the cost function

$$I(T) = \int |T(\mathbf{x}) - \mathbf{x}|^2 \rho_a(\mathbf{x})\, dx\,, \tag{3.20}$$

i.e.,

$$\begin{aligned}\mathcal{T}_2(\rho_a,\rho_b) &\equiv \inf\left\{I(T):\ T \text{ measurable},\ \rho_a(\mathbf{x})=\rho_b(T(\mathbf{x}))\det(\nabla T(\mathbf{x}))\right\}\\ &= \inf\left\{(b-a)A(\rho,\mathbf{v}):\ (\rho,\mathbf{v})\in V(\rho_a,\rho_b)\right\}\,,\end{aligned} \tag{3.21}$$

where $V(\rho_a,\rho_b)$ is the set of pairs $(\rho,\mathbf{v})\in X$ such that $\cup_{t\in[a,b]}\mathrm{supp}\rho(\cdot,t)$ is bounded, (3.5a) is satisfied weakly in a distributional sense, $\rho(\cdot,a)=\rho_a$ and $\rho(\cdot,b)=\rho_b$. Here and subsequently, $\mathrm{supp}f$ denotes the support of a measurable function f.

The minimum cost of transportation (3.21) can be related to the Wasserstein distance,

$$d_W(\rho_a,\rho_b)=\left\{\inf_{\sigma\in\Gamma(\rho_a,\rho_b)}\int\int|\mathbf{x}-\mathbf{y}|^2\sigma(\mathbf{x},\mathbf{y})dxdy\right\}^{1/2}\,, \tag{3.22}$$

where the infimum is taken over the space of Radon measures of mass M with finite second moments and marginals

$$\int\sigma(\mathbf{x},\mathbf{y})dy=\rho_a(\mathbf{x})\,, \tag{3.23a}$$

$$\int\sigma(\mathbf{x},\mathbf{y})dx=\rho_b(\mathbf{y})\,. \tag{3.23b}$$

Then we have

$$\mathcal{T}_2(\rho_a,\rho_b)=d_W^2(\rho_a,\rho_b)\,, \tag{3.24}$$

i.e., the cost of transportation is given by the Wasserstein distance between the initial and final mass densities.

Recall that the manifold of probability densities on the Euclidean space $\mathbb{R}^n$ is

defined as

$$\mathcal{M} = \left\{ \rho : \mathbb{R}^n \to [0,\infty) \text{ measurable } | \int_{\mathbb{R}^n} \rho(\mathbf{x}) d\mathbf{x} = 1 \text{ and } \int_{\mathbb{R}^n} |\mathbf{x}|^2 \rho(\mathbf{x}) d\mathbf{x} < \infty \right\} . \tag{3.25}$$

This set is not a vector space and consequently the straightforward distances between two probability distributions are not a natural choice, which gives difficulty to take variations of the minimum cost of transportation $\mathcal{T}_2(\rho_a, \rho_b)$ with respect to ρ. A theorem of Ambrosio et al. [1] (see also Villani, Thm. 8.13) shows how to define the tangent space of the manifold $\mathcal{M}$. Thus, suppose that $\rho_a, \rho_b \in L^1(\mathbb{R}^n; [0,\infty))$ and have finite second moments. Let $\rho(\mathbf{x}, t)$, $t \in (b-\epsilon, b+\epsilon)$ be a path in $L^1(\mathbb{R}^n; [0,\infty))$ of mass densities with finite second moments such that $\rho(\cdot, 0) = \rho_b$ and

$$\frac{\partial \rho}{\partial t} + \nabla \cdot (\rho \xi) = 0 \,, \tag{3.26}$$

for some C^1, globally bounded, velocity field ξ. Then,

$$\frac{d\rho_t}{dt}|_{t=0} = -(\rho \nabla \cdot \xi + \nabla \rho \cdot \xi) = -\nabla \cdot (\rho \xi) \,. \tag{3.27}$$

This suggests the following characterization of the tangent space of $\mathcal{M}$ at ρ,

$$T_\rho \mathcal{M} = \{ s | s = -\nabla \cdot (\rho \xi) \text{ for some } \ \xi \in C_0^\infty(\mathbb{R}^n, \mathbb{R}^n) \} \,. \tag{3.28}$$

Consequently,

$$\frac{d}{dt}\mathcal{T}_2(\rho_a,\rho)_{|t=0} = 2\int \langle T(\mathbf{x})-\mathbf{x}, \xi(T(\mathbf{x}))\rangle d\rho_a(\mathbf{x})\,, \tag{3.29}$$

where T is the optimal transference mapping from ρ_a to ρ_b. Further, for some real functions on $\mathcal{M}$, for instance consider an energy functional of the type

$$F(\rho) = \int_{\mathbb{R}^n} \rho\psi d\mathbf{x}\,, \tag{3.30}$$

where ψ is a potential defined in $\mathbb{R}^n$, the variation of the functional with respect to ρ can be obtained as

$$\delta F = \frac{dF(\rho_t)}{dt}|_{t=0} = \int_{\mathbb{R}^n} \psi s d\mathbf{x} = -\int_{\mathbb{R}^n} \psi\nabla\cdot(\rho\xi)d\mathbf{x} = \int_{\mathbb{R}^n} \rho\nabla\psi\cdot\xi d\mathbf{x} = \int_{\mathbb{R}^n} \rho\delta\psi(\xi)d\mathbf{x}\,. \tag{3.31}$$

3.1.2 Discrete time Lagrangian dynamics

Before conducting the time discretization, it is necessary to give a brief introduction of the basic ideas in discrete time Lagrangian dynamics, which will be used all the way to give the semi-discretization of the action (3.11) [28, 34].

For conservative systems, one typically begins with a Lagrangian $L(\mathbf{q},\dot{\mathbf{q}})$ with $\mathbf{q} = (q_1, q_2, ..., q_n)^T$ as configuration space variables, and the Hamilton's principle requires the action stationary. We form the action functional by integrating the Lagrangian L along a curve $\mathbf{q}(t)$ and then compute variations of the action while

holding the endpoints of the curve $\mathbf{q}(t)$ fixed,

$$\begin{aligned}\delta S(\mathbf{q}) = \delta \int_a^b L(\mathbf{q}, \dot{\mathbf{q}}) dt &= \int_a^b \Big[\frac{\partial L}{\partial \mathbf{q}} \delta \mathbf{q} + \frac{\partial L}{\partial \dot{\mathbf{q}}} \delta \dot{\mathbf{q}}\Big] dt \\ &= \int_a^b \Big[\frac{\partial L}{\partial \mathbf{q}} - \frac{\partial}{\partial t}\big(\frac{\partial L}{\partial \dot{\mathbf{q}}}\big)\Big] \delta \mathbf{q} dt + \Big[\frac{\partial L}{\partial \dot{\mathbf{q}}} \delta \mathbf{q}\Big]_a^b,\end{aligned} \tag{3.32}$$

where we have used integration by parts. The boundary term is vanished because we assume that boundary is fixed, i.e., $\delta \mathbf{q}(0) = \delta \mathbf{q}(T) = 0$. Thus the stationary point of the action gives the well-known Euler-Lagrange equations associated to the action $S(\mathbf{q})$.

$$\frac{\partial L}{\partial \mathbf{q}}(\mathbf{q}, \dot{\mathbf{q}}) - \frac{\partial}{\partial t}\big(\frac{\partial L}{\partial \dot{\mathbf{q}}}(\mathbf{q}, \dot{\mathbf{q}})\big) = 0 \tag{3.33}$$

For forced or dissipative systems, one can apply the integral Lagrange-d'Alembert principle.

$$\delta A(\mathbf{q}) = \delta \int_a^b L(\mathbf{q}, \dot{\mathbf{q}}) dt + \int_a^b F(\mathbf{q}, \dot{\mathbf{q}}) \delta \mathbf{q} dt = 0 \tag{3.34}$$

Next we will show how discrete vatiational mechanics performs an analogue of the above derivation for the continuous Euler-Lagrange equations. Suppose rather than taking a continuous curve $\mathbf{q}(t)$ on the Riemannian manifold, consider a discrete curve of points $\{\mathbf{q}_k\}_{k=0}^N$ where $\mathbf{q}_0 = \mathbf{q}(0)$, $\mathbf{q}_N = \mathbf{q}(T)$, and a uniform time step $\Delta t = t_{k+1} - t_k$ (or variant time steps Δt_k), Fig 3.1.

We denote a discrete Lagrangian $L_d(\mathbf{q}_k, \mathbf{q}_{k+1}, \Delta t)$ as

$$L_d(\mathbf{q}_k, \mathbf{q}_{k+1}, \Delta t) = \int_{t_k}^{t_{k+1}} L(\mathbf{q}(t), \dot{\mathbf{q}}(t)) dt\,. \tag{3.35}$$

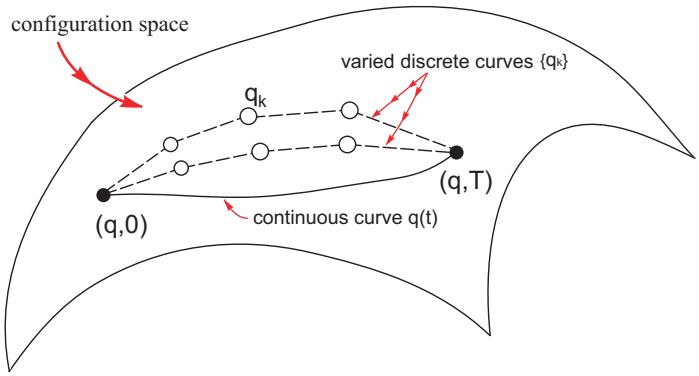

Figure 3.1: Time discrete Lagrangian dynamics.

Thus we can calculate the discrete action along this sequence by summing the discrete Lagrangian on each adjacent pair. Following the continuous derivation above, we compute variations of this action sum with the boundary points fixed,i.e., $\delta \mathbf{q}_0 = \delta \mathbf{q}_N = 0$. This gives

$$\begin{aligned}
\delta S_d(\mathbf{q}_1, \cdots, \mathbf{q}_{N-1}) &= \delta \sum_{k=0}^{N-1} L_d(\mathbf{q}_k, \mathbf{q}_{k+1}, \Delta t) \\
&= \sum_{k=0}^{N-1} \left[\frac{\partial L_d}{\partial \mathbf{q}_k}(\mathbf{q}_k, \mathbf{q}_{k+1}, \Delta t)\delta \mathbf{q}_k + \frac{\partial L_d}{\partial \mathbf{q}_{k+1}}(\mathbf{q}_k, \mathbf{q}_{k+1}, \Delta t)\delta \mathbf{q}_{k+1} \right] \\
&= \sum_{k=1}^{N-1} \left[\frac{\partial L_d}{\partial \mathbf{q}_k}(\mathbf{q}_{k-1}, \mathbf{q}_k, \Delta t) + \frac{\partial L_d}{\partial \mathbf{q}_k}(\mathbf{q}_k, \mathbf{q}_{k+1}, \Delta t) \right] \delta \mathbf{q}_k \,,
\end{aligned} \tag{3.36}$$

where we have used the point position $(\mathbf{q}_k, \mathbf{q}_{k+1})$ in the configuration space to approximate the velocity, for instance a simple finite difference rule for the derivative (the velocity vector replaced by $(\mathbf{q}_{k+1} - \mathbf{q}_k)/\Delta t$). If we now require the variations of the action be zero for any choice of $\delta \mathbf{q}_k$, then we obtain the discrete Euler-Lagrange

equations for each k

$$\frac{\partial L_d}{\partial \mathbf{q}_k}(\mathbf{q}_{k-1}, \mathbf{q}_k, \Delta t) + \frac{\partial L_d}{\partial \mathbf{q}_k}(\mathbf{q}_k, \mathbf{q}_{k+1}, \Delta t) = 0\,. \tag{3.37}$$

Henceforth if we take initial conditions $(\mathbf{q}_0, \mathbf{q}_1)$ then the discrete Euler-Lagrange equations define a recursive rule for calculating the sequence of $\{\mathbf{q}_k\}_{k=1}^{N-1}$, the map$(\mathbf{q}_{k-1}, \mathbf{q}_k) \mapsto (\mathbf{q}_k, \mathbf{q}_{k+1})$ is known as the discrete evolution map.

3.1.3 Time discretization

Next, we turn to the question of time discretization of the action (3.11). To this end, let $t_0 = a < t_1 < \cdots < t_N = b$ be a discretization of the time interval $[a, b]$. Recall that $(1/2)d_W^2(\rho_a, \rho_b)/(b-a)$ gives the exact minimum of the action $A(\rho, \mathbf{v})$ over the entire time interval $[a, b]$. Building on this identity we can define the semi-discrete action

$$A_d(\rho_1, \ldots, \rho_{N-1}) = \sum_{k=0}^{N-1} \frac{1}{2} \frac{\mathcal{T}_2(\rho_k, \rho_{k+1})}{t_{k+1} - t_k}\,, \tag{3.38}$$

which is expressed directly in terms of densities. If no further approximation is introduced we may expect the infimum of A_d over $\{\rho_1, \ldots, \rho_{N-1}\} \in [L^1(\mathbb{R}^n; [0, \infty))]^{N-1}$ to be again $(1/2)\mathcal{T}_2(\rho_a, \rho_b)/(b-a)$ and the scheme to be exact. The discrete motion consists of incremental transference maps $\varphi_{k \to k+1}$ transporting ρ_k into ρ_{k+1} over the time internal $[t_k, t_{k+1}]$ optimally with respect to the cost function (3.20).

The discrete equations of motion now follow by rendering the discrete action

stationary. Taking variations of (3.38) with respect to ρ_k with the aid of (3.29) gives

$$\langle \delta A_d, \xi_k \rangle = \int \left\{ \rho_k \left(\frac{\varphi_{k\to k+1}(\mathbf{x}) - \mathbf{x}}{t_{k+1} - t_k} + \frac{\varphi_{k\to k-1}(\mathbf{x}) - \mathbf{x}}{t_k - t_{k-1}} \right) \cdot \xi_k \right\} dx \,, \tag{3.39}$$

where we write

$$\varphi_{k\to k-1} = \varphi_{k-1\to k}^{-1} \,. \tag{3.40}$$

In (3.39) $\varphi_{k\to k+1}$ denotes the optimal transference mapping from ρ_k to ρ_{k+1} and, in particular, we have

$$\rho_{k+1} \circ \varphi_{k\to k+1} = \rho_k / \det \left(\nabla \varphi_{k\to k+1} \right) . \tag{3.41}$$

We note that these mass-density updates differ sharply from conventional Eulerian algorithms, which rely on some direct time discretization of the continuity equation. In particular, the mass-density updates (3.41) are geometrically exact. Integrating by parts (3.39) using (3.7) and enforcing stationarity with respect to to all variations ξ_k we obtain

$$\rho_k \left(\frac{\varphi_{k\to k+1} - \mathrm{id}}{t_{k+1} - t_k} + \frac{\varphi_{k\to k-1} - \mathrm{id}}{t_k - t_{k-1}} \right) = 0 \,. \tag{3.42}$$

Evidently, these equations are jointly satisfied by setting

$$\varphi_{k\to k+1}(\mathbf{x}) = \varphi(\varphi^{-1}(\mathbf{x}, t_k), t_{k+1}) \,, \tag{3.43}$$

where φ is given McCann's displacement interpolation (3.18), which shows that the discretization (3.39) is indeed exact, as expected.

3.1.4 Spatial discretization

Finally, we turn to the question of spatial discretization of the semi-discrete action (3.38). A natural and computationally convenient spatial discretization may be effected by considering mass densities of the type

$$\rho_{h,k}(\mathbf{x}) = \sum_{p=1}^{M} m_{p,k}\delta\big(\mathbf{x} - \mathbf{x}_{p,k}\big)\,, \tag{3.44}$$

where $\mathbf{x}_{p,k}$ represents the position at time t_k of a *material point* of mass m_p and $\delta\big(\mathbf{x} - \mathbf{x}_{p,k}\big)$ is the Dirac-delta distribution centered at $\mathbf{x}_{p,k}$. A fully discrete action may then be obtained by inserting representation (3.44) into (3.38), which defines a discrete transportation problem (cf., e.g., [17]).

We note that, by considering mass distributions of the form (3.44) we have expanded the original space of solutions $L^1(\mathbb{R}^n;[0,\infty))$ to a larger space of $\mathcal{M}(\mathbb{R}^n)$ of Radon measures. In computing the minimum cost of transportation $\mathcal{T}_2(\rho_{h,k},\rho_{h,k+1})$ between two consecutive discrete mass densities, the incremental optimal transference mappings $\varphi_{h,k\to k+1}$ transporting $\rho_{h,k}$ into $\rho_{h,k+1}$ are simply rearrangements of the point set $\{\mathbf{x}_{1,k},\ldots,\mathbf{x}_{M,k}\}$ into the point set $\{\mathbf{x}_{1,k+1},\ldots,\mathbf{x}_{M,k+1}\}$. In addition, the incremental mass conservation relation (3.41) must be understood in a weak or distributional sense, i.e., as the requirement that

$$\int \rho_k(\mathbf{x})\eta(\mathbf{x})\,dx = \int \rho_{k+1}(\mathbf{y})\eta\big(\varphi^{-1}_{k\to k+1}(\mathbf{y})\big)dy\,, \tag{3.45}$$

for all test functions η. For discrete mass distributions of the form (3.44), (3.45)

reduces to

$$\sum_{p=1}^{M} m_{p,k}\eta(\mathbf{x}_{p,k}) = \sum_{p=1}^{M} m_{p,k+1}\eta(\mathbf{x}_{p,k})\,, \tag{3.46}$$

which must be satisfied for all test functions η and, hence,

$$m_{p,k} = m_{p,k+1} = m_p\,, \tag{3.47}$$

i.e., the material points must have constant mass.

The fully discrete action now takes the form

$$A_h(\rho_{h,1},\ldots,\rho_{h,N-1}) = \sum_{k=0}^{N-1}\sum_{p=1}^{M} \frac{m_p}{2}\frac{|\mathbf{x}_{p,k+1}-\mathbf{x}_{p,k}|^2}{t_{k+1}-t_k}\,, \tag{3.48}$$

which is the semi-discrete action of a system of non-interacting mass particles. The corresponding discrete Euler-Lagrange equations are

$$\frac{\mathbf{x}_{p,k+1}-\mathbf{x}_{p,k}}{t_{k+1}-t_k} - \frac{\mathbf{x}_{p,k}-\mathbf{x}_{p,k-1}}{t_k-t_{k-1}} = 0\,, \tag{3.49}$$

or, equivalently,

$$\mathbf{x}_{p,k+1} = \mathbf{x}_{p,k} + (t_{k+1}-t_k)\frac{\mathbf{x}_{p,k}-\mathbf{x}_{p,k-1}}{t_k-t_{k-1}}\,, \tag{3.50}$$

which provides an update for the positions of the material points. In this update

$$\mathbf{v}_{p,k} \equiv \frac{\mathbf{x}_{p,k}-\mathbf{x}_{p,k-1}}{t_k-t_{k-1}} \tag{3.51}$$

may be regarded as the velocity of material point p at time t_k, whereupon the update

(3.50) takes the particularly simple form

$$\mathbf{x}_{p,k+1} = \mathbf{x}_{p,k} + (t_{k+1} - t_k)\mathbf{v}_{p,k}\,. \tag{3.52}$$

These updates simply define a *ballistic* motion of the material points from their initial positions $\mathbf{x}_{p,0}$ to their final positions $\mathbf{x}_{p,N}$.

3.2 Solid Flows

In this section, we extend the optimal transportation framework developed in the foregoing for systems of non-interacting particles to general solid flows. For these systems, inertia competes with free energy and viscosity in determining the flow of mass.

3.2.1 Elastic solids

We begin by considering the general elastic solid flow in $\mathbb{R}^n$. The motion of the solid flow over a time interval $[a, b]$ is governed by the coupled equations

$$\frac{\partial \rho}{\partial t} + \nabla \cdot (\rho \mathbf{v}) = 0\,, \tag{3.53a}$$

$$\frac{\partial (\rho \mathbf{v})}{\partial t} + \nabla \cdot (\rho \mathbf{v} \otimes \mathbf{v} - \boldsymbol{\sigma}) = \rho \mathbf{b}\,. \tag{3.53b}$$

where $\boldsymbol{\sigma}$ is the Cauchy stress tensor, $\mathbf{b}$ are body forces. As in the optimal transportation problem (3.5) we assume that mass does not leak to infinity, eq. (3.7), whence

it follows from (3.53a) that the total mass of the system remains constant throughout the flow. Again, we suppose that the initial and final mass densities are given, eqs. (3.9), whereupon the problem becomes a *transportation problem* of finding the flow that transports the initial mass density ρ_a to the final one ρ_b.

For simplicity, we assume the solid is homogenous and isotropic, which leads to the definition of Piola-Kirchhoff stress tensor

$$\mathbf{P} = \frac{\partial W(\mathbf{F})}{\partial \mathbf{F}}\,, \tag{3.54}$$

where $W(\mathbf{F})$ is the strain energy density per unit volume in the reference configuration and $\mathbf{F}$ is the deformation gradient. The cauchy stress tensor is related to the Piola-Kirchhoff stress tensor by

$$\boldsymbol{\sigma} = J^{-1}\mathbf{P}\mathbf{F}^T\,, \tag{3.55}$$

where J is the Jacobian of $\mathbf{F}$. We shall additionally assume that the body forces derive from a scalar potential ψ,i.e.,

$$\mathbf{b} = \nabla\psi\,. \tag{3.56}$$

If we define

$$\mathbf{f}(\mathbf{x},t) = \mathbf{F}(\varphi^{-1}(\mathbf{x},t),t) \quad \text{and} \quad J_f(\mathbf{x},t) = \det\mathbf{f} = J\circ\varphi^{-1}\,, \tag{3.57}$$

hence, the action of the flow differs from the bare action (3.11) in that the solid flow

now have free energy and moves under the action of body-force potential. Adding the corresponding terms to (3.11) the action now becomes

$$A(\mathbf{f},\mathbf{v}) = \int_a^b \left\{ \int \left[\frac{\rho}{2}|\mathbf{v}|^2 - \rho(w(\mathbf{f}) - \psi) \right] d\mathbf{x} \right\} dt\,, \tag{3.58}$$

where $\rho = \rho_0/J_f$ and $w(\mathbf{f})$ is the strain energy density per unit deformed mass. In analogy to the case of optimal transportation, we expect the flow to render the action (3.58) stationary–no longer necessarily a minimum–under the constraint of the continuity equation (3.53a), which defines the stationary-point problem

$$\delta A(\mathbf{f}, v) = 0\,, \tag{3.59a}$$

$$\text{subject to: } \rho = \frac{\rho_0}{J_f}\,, \tag{3.59b}$$

$$\frac{\partial \mathbf{f}}{\partial t} + \mathbf{v}\cdot\nabla\mathbf{f} = (\nabla\mathbf{v})\mathbf{f}\,. \tag{3.59c}$$

Note that (3.58b) is equivalent to the continuity equation (3.53a). This stationarity principle now replaces the Benamou and Brenier minimum principle (3.10). We may again formally verify that the stationary-point problem (3.59) is indeed equivalent to (3.9), (3.53) simply by replacing ρ by $\mathbf{f}$ from the first constraint and enforcing the second constraint by means of a Lagrange multiplier, which leads to the extended action

$$\begin{aligned} A(\mathbf{f},\mathbf{v},\boldsymbol{\lambda}) = \int_a^b \left\{ \int \left[\frac{\rho_0}{2J_f}|\mathbf{v}|^2 - \frac{\rho_0}{J_f}(w(\mathbf{f}) - \psi) \right] d\mathbf{x} \right\} dt + \\ \int_a^b \left\{ \int \left[\big(\frac{\partial \mathbf{f}}{\partial t} + \mathbf{v}\cdot\nabla\mathbf{f} - (\nabla\mathbf{v})\mathbf{f}\big) : \boldsymbol{\lambda} \right] d\mathbf{x} \right\} dt\,, \end{aligned} \tag{3.60}$$

where $\boldsymbol{\lambda}$ is the Lagrange multiplier and a second-order tensor. Stationary now demands that

$$
\begin{aligned}
&0 = \delta A(\mathbf{f}, \mathbf{v}, \boldsymbol{\lambda}) = \\
&\int_a^b \left\{ \int \left[\rho \mathbf{v} \cdot \delta \mathbf{v} - \rho \left((\frac{|\mathbf{v}|^2}{2} - w(\mathbf{f}) + \psi) \mathbf{f}^{-T} + \frac{\partial w(\mathbf{f})}{\partial \mathbf{f}} \right) : \delta \mathbf{f} \right] d\mathbf{x} \right\} dt + \\
&\int_a^b \left\{ \int \left[(\frac{\partial (\delta \mathbf{f})}{\partial t} + \mathbf{v} \cdot \nabla (\delta \mathbf{f}) + \nabla \mathbf{f} \cdot \delta \mathbf{v} - \nabla (\delta \mathbf{v}) \mathbf{f} - (\nabla \mathbf{v}) \delta \mathbf{f}) : \boldsymbol{\lambda} \right] d\mathbf{x} \right\} dt + \\
&\int_a^b \left\{ \int \left[(\frac{\partial \mathbf{f}}{\partial t} + \mathbf{v} \cdot \nabla \mathbf{f} - (\nabla \mathbf{v}) \mathbf{f}) : \delta \boldsymbol{\lambda} \right] d\mathbf{x} \right\} dt \, .
\end{aligned}
\tag{3.61}
$$

Integrating by parts with the aid of (3.7) and requiring stationarity for all admissible variations, we obtain the Euler-Lagrange equations associated to the extended action.

$$\rho v_i + \lambda_{jI} \frac{\partial f_{jI}}{\partial x_i} + \frac{\partial (\lambda_{iI} f_{jI})}{\partial x_j} = 0 \, , \tag{3.62a}$$

$$\rho (-\frac{|\mathbf{v}|^2}{2} + w(\mathbf{f}) - \psi) f_{Ji}^{-1} + \rho \frac{\partial w(\mathbf{f})}{\partial f_{iJ}} - \frac{\partial \lambda_{iJ}}{\partial t} - \frac{\partial (\lambda_{iJ} v_j)}{\partial x_j} - \frac{\partial v_j}{\partial x_i} \lambda_{jJ} = 0 \, , \tag{3.62b}$$

$$\frac{\partial f_{iJ}}{\partial t} + v_j \frac{\partial f_{iJ}}{\partial x_j} - \frac{\partial v_i}{\partial x_j} f_{jJ} = 0 \, . \tag{3.62c}$$

Recall the relation (3.55) between the cauchy stress tensor and the Piola-Kirchhoff stress tensor, we obtain

$$\rho \frac{\partial w(\mathbf{f})}{\partial \mathbf{f}} \mathbf{f}^T = \boldsymbol{\sigma} \, . \tag{3.63}$$

We multiply equation (3.62b) by $\mathbf{f}$ on the left and take divergence, on the other hand take time derivative on equation (3.62a), by using the identity (3.62c) finally we can simplify the Euler-Lagrange equations into the single form of Euler's equation of

motion (3.53b), as required.

3.2.2 Time discretization

The aim now is to formulate a time-discretized, or *semi-discrete*, approximate action for elastic solid flows that extends the semi-discrete action (3.38) for non-interacting flows. The additional terms to be taken into account in this extension concern the free energy of the solid and the body-force distribution. Using a trapezoidal rule approximation for the corresponding action terms gives a semi-discrete action of the form

$$A_d(\mathbf{f}_1,\ldots,\mathbf{f}_{N-1}) = \sum_{k=0}^{N-1}\left\{\frac{1}{2}\frac{\mathcal{T}_2(\rho_k,\rho_{k+1})}{(t_{k+1}-t_k)^2} - \frac{1}{2}[U(\mathbf{f}_k)+U(\mathbf{f}_{k+1})]\right\}(t_{k+1}-t_k)\,, \quad (3.64)$$

which is expressed directly in terms of densities. In this expression

$$U(\mathbf{f}) = \int \rho(w(\mathbf{f})-\psi)\,d\mathbf{x} \quad (3.65)$$

is the total internal energy of the solid. The discrete equations of motion now follow by rendering the semi-discrete (3.64) action stationary. Since ρ and $\mathbf{f}$ is exchangeable, and the tangent space of the manifold of probability densities is well defined, we will take variations of (3.64) with respect to ρ_k instead of $\mathbf{f}_k$ with the aid of (3.29) gives

$$\begin{aligned}\langle \delta A_d, \xi_k\rangle = \int \Bigg\{ &\rho_k\left(\frac{\varphi_{k\to k+1}(\mathbf{x})-\mathbf{x}}{t_{k+1}-t_k} + \frac{\varphi_{k\to k-1}(\mathbf{x})-\mathbf{x}}{t_k-t_{k-1}}\right)\cdot\xi_k \\ &- \frac{t_{k+1}-t_{k-1}}{2}\rho_k[w(\mathbf{f}_k)-\psi(\mathbf{x},t_k)]\nabla\cdot(\rho_k\xi_k)\Bigg\}\,d\mathbf{x}\,,\end{aligned} \quad (3.66)$$

where $\varphi_{k\to k+1}$ is a transference map transporting ρ_k into ρ_{k+1} optimally over the time internal $[t_k, t_{k+1}]$ and we adopt the notation (3.40). In particular, identity (3.41) holds. Integrating by parts (3.66) using (3.7) we obtain

$$\begin{aligned}\langle \delta A_d, \xi_k \rangle = \int \Bigg\{ \rho_k \left(\frac{\varphi_{k\to k+1}(\mathbf{x}) - \mathbf{x}}{t_{k+1} - t_k} + \frac{\varphi_{k\to k-1}(\mathbf{x}) - \mathbf{x}}{t_k - t_{k-1}} \right) \cdot \xi_k \\ - \frac{t_{k+1} - t_{k-1}}{2} [\nabla \cdot \boldsymbol{\sigma}(\mathbf{f}_k) + \rho_k \mathbf{b}_k] \cdot \xi_k \Bigg\} d\mathbf{x} \,,\end{aligned} \tag{3.67}$$

where we write $\mathbf{b}_k(\cdot) = \mathbf{b}(\cdot, t_k)$. Enforcing stationarity with respect to to all variations ξ_k we obtain

$$\frac{2\rho_k}{t_{k+1} - t_{k-1}} \left(\frac{\varphi_{k\to k+1} - \mathrm{id}}{t_{k+1} - t_k} + \frac{\varphi_{k\to k-1} - \mathrm{id}}{t_k - t_{k-1}} \right) - \nabla \cdot \boldsymbol{\sigma}_k = \rho_k \mathbf{b}_k \,, \tag{3.68}$$

where again we write $\boldsymbol{\sigma}_k(\cdot) = \boldsymbol{\sigma}(\cdot, t_k)$. A comparison of (3.68) and (3.42) shows that the discrete motion is now the result of the competition between inertia, represented by the first term in (3.68), which aims to transport ρ_k into ρ_{k+1} over the time internal $[t_k, t_{k+1}]$ optimally with respect to the cost function (3.20), and the internal energy of the flow, which introduces discrete percussions at the discrete times $t_0 < t_1 < \cdots < t_N$ causing the trajectory to deviate from the optimal transportation path.

Equation (3.68) defines a semi-discrete central-difference scheme that can be solved forward explicitly. This forward solution takes the form:

i) Initialization: Set $k = 0$, $\rho_0 = \rho_a$ and $\mathbf{f}_0 = \mathbf{f}_a$.

ii) Given ρ_k or $\mathbf{f}_k$, solve (3.68) for the incremental deformation mapping $\varphi_{k\to k+1}$,

with the result:

$$\varphi_{k\to k+1} = \mathrm{id} + (t_{k+1} - t_k) \left\{ \frac{\mathrm{id} - \varphi_{k\to k-1}}{t_k - t_{k-1}} + \frac{t_{k+1} - t_{k-1}}{2} \frac{\rho_k \mathbf{b}_k + \nabla \cdot \boldsymbol{\sigma}_k}{\rho_k} \right\} . \quad (3.69)$$

iii) Update the mass density according to identity (3.41).

iv) Reset $k \leftarrow k + 1$. If $k = N$ exit. Otherwise go to (ii).

This forward solution has the usual structure of explicit time-integration schemes in that the incremental deformation mapping $\varphi_{k\to k+1}$ is computed directly from the initial conditions at the beginning of the time step, including the velocity estimate

$$\mathbf{v}_k \equiv \frac{\mathrm{id} - \varphi_{k\to k-1}}{t_k - t_{k-1}} , \quad (3.70)$$

and the out-of-balance forces $\rho_k \mathbf{b}_k + \nabla \cdot \boldsymbol{\sigma}_k$. However, as noted earlier the time-integration algorithm (3.41), (3.69) differs from conventional Eulerian algorithms, which rely on some direct time-discretization of the continuity equation, in that the update of the mass density (3.41) is geometrically exact.

3.2.3 Spatial discretization

In order to obtain a fully discrete action for computations, we proceed to effect a spatial discretization of the semi-discrete action (3.64). In particular, we wish to carry over to the present setting the material-point formalism introduced in §3.1.4 for non-interacting fluids. Recall that, in that context, material points are introduced

by adopting concentrated mass densities of the form (3.44). The operation of inserting these mass densities into the semi-discrete action (3.38), or directly into the semi-discrete Euler-Lagrange equation (3.39), is mathematically well defined since for a non-interacting fluid the mass density enters the variation of the action linearly, eq. (3.39). By contrast, for a compressible fluid the mass density enters non-linearly in the variation of the semidiscrete action, eq. (3.66), and the insertion of representation (3.44) directly into (3.66) no longer makes mathematical sense.

In order to overcome this difficulty, we note that representation (3.44) combines two mathematically distinct operations that become blurred in the context of non-interacting fluids but that need to be carefully separated for general flows. The first operation is the approximation of the usual Lebesgue measure of volume $\mathcal{L}$ by discrete measures,

$$\mathcal{L}_{h,k} = \sum_{p=1}^{M} \upsilon_{p,k}\, \delta_{\mathbf{x}_{p,k}}\,, \tag{3.71}$$

concentrated at *material points* $\mathbf{x}_{p,k}$, each of which is assigned a discrete volume $\upsilon_{p,k}$. Thus, for any smooth function f we have

$$\int f d\mathcal{L}_{h,k} = \sum_{p=1}^{M} f(\mathbf{x}_{p,k})\, \upsilon_{p,k}\,. \tag{3.72}$$

In addition, the usual push-forward operation for measures,

$$\int \eta(\mathbf{y}) d\mathbf{y} = \int \eta\big(\varphi_{k\to k+1}(\mathbf{x})\big)\, \det\big(\nabla\varphi_{k\to k+1}(\mathbf{x})\big)\, dx\,, \tag{3.73}$$

now becomes

$$\sum_{p=1}^{M} \eta(\mathbf{x}_{p,k+1})\, \upsilon_{p,k+1} = \sum_{p=1}^{M} \eta\big(\varphi_{k\to k+1}(\mathbf{x}_{p,k})\big) \det\big(\nabla\varphi_{k\to k+1}(\mathbf{x}_{p,k})\big)\, \upsilon_{p,k}\,. \tag{3.74}$$

But material points are convected by the flow, i.e.,

$$\mathbf{x}_{p,k+1} = \varphi_{k\to k+1}(\mathbf{x}_{p,k})\,. \tag{3.75}$$

Inserting this identity in (3.74) and noting that η is arbitrary gives

$$\upsilon_{p,k+1} = \det\big(\nabla\varphi_{k\to k+1}(\mathbf{x}_{p,k})\big)\, \upsilon_{p,k}\,, \tag{3.76}$$

which defines the material-point volume update.

The second operation subsumed in representation (3.44) is the identification of discrete mass distributions as measures that are absolutely continuous with respect to the discrete volume measure $\mathcal{L}_{h,k}$, with Radon-Nykodim density $\rho_{h,k}$, in the same manner as continuous mass distributions are defined by measures that are absolutely continuous with respect to the usual Lebesgue measure $\mathcal{L}$ with density ρ_k. Owing to the discreteness of $\mathcal{L}_{h,k}$, the corresponding mass densities $\rho_{h,k}$ are defined simply by assigning mass density values $\rho_{p,k}$ to every material point, i.e.,

$$\rho_{h,k}(\mathbf{x}) = \sum_{p=1}^{M} \rho_{p,k}\upsilon_{p,k}\delta\big(\mathbf{x} - \mathbf{x}_{p,k}\big)\,, \tag{3.77}$$

Comparing (3.77) and (3.44) yields the identity

$$m_p = \rho_{p,k} \upsilon_{p,k} \,, \tag{3.78}$$

where have used (3.47). Equivalently,

$$\rho_{p,k} = \frac{m_p}{\upsilon_{p,k}} \tag{3.79}$$

relates the mass density at material point $\mathbf{x}_{p,k}$ with to its mass and volume.

The identities (3.75), (3.76) and (3.84) provide update formulae for the position, volume and mass density of the material points. However, it should be carefully noted that the gradient of the transference map $\varphi_{k\to k+1}$ appears explicitly in (3.76). Therefore, in contrast to the case of non-interacting fluids, where it suffices to track the motion of the material points, now the transference maps $\varphi_{k\to k+1}$ must be approximated by conforming interpolations of the form

$$\varphi_{h,k\to k+1}(\mathbf{x}) = \sum_{a=1}^{N} \mathbf{x}_{a,k+1} N_{a,k}(\mathbf{x}) \,, \tag{3.80}$$

where $\{\mathbf{x}_{a,k+1},\ a = 1, \ldots, N\}$ are coordinates of nodes on the configuration at time t_{k+1} and $N_{a,k}(\mathbf{x})$ are conforming shape functions defined over the configuration at

time t_k with the usual properties,

$$\sum_{a=1}^{N} N_{a,k}(\mathbf{x}) = 1\,, \tag{3.81a}$$

$$\sum_{a=1}^{N} \mathbf{x}_{a,k} N_{a,k}(\mathbf{x}) = \mathbf{x}\,, \tag{3.81b}$$

of exact interpolation of linear functions. For discrete transference maps of the form (3.80), the material-point update (3.75) becomes

$$\mathbf{x}_{p,k+1} = \sum_{a=1}^{N} \mathbf{x}_{a,k+1} N_{a,k}(\mathbf{x}_{p,k})\,, \tag{3.82}$$

and the deformation gradient can be updated by

$$\mathbf{f}_{p,k+1} = \nabla \varphi_{k\to k+1}(x_{p,k}) \mathbf{f}_{p,k}\,. \tag{3.83}$$

We note that the consistency conditions (3.81) leave considerable latitude in the choice of shape functions. For instance, in calculations we choose to initialize the material point volumes and densities by means of an initial triangulation of the domain. We additionally choose to employ meshless max-ent shape functions [2] computed from convected nodal coordinates. We shall say that the shape functions are *backward-compatible* if they satisfy the condition

$$\mathbf{x}_{p,k-1} = \sum_{a=1}^{N} \mathbf{x}_{a,k-1} N_{a,k}(\mathbf{x}_{p,k})\,. \tag{3.84}$$

Insertion of the preceding approximations into (3.64) yields the discrete action

$$
\begin{aligned}
A_h(\mathbf{f}_{h,1},\ldots,\mathbf{f}_{h,N-1}) = \sum_{k=0}^{N-1}\sum_{p=1}^{M} m_p \Bigg\{ \frac{1}{2}\frac{|\mathbf{x}_{p,k+1}-\mathbf{x}_{p,k}|^2}{(t_{k+1}-t_k)^2} \\
- \frac{1}{2}[\big(w(\mathbf{f}_{p,k})-\psi(\mathbf{x}_{p,k})\big)+\big(w(\mathbf{f}_{p,k+1})-\psi(\mathbf{x}_{p,k+1})\big)]\Bigg\}(t_{k+1}-t_k)\,,
\end{aligned}
\tag{3.85}
$$

where (3.84) is tacitly understood to be in force. Taking variations of A_h gives the discrete Euler-Lagrange equations

$$
\begin{aligned}
\langle \delta A_h, \xi_h\rangle = \sum_{k=0}^{N-1}\sum_{p=1}^{M} m_p \Bigg\{ \left(\frac{\mathbf{x}_{p,k+1}-\mathbf{x}_{p,k}}{t_{k+1}-t_k}+\frac{\mathbf{x}_{p,k}-\mathbf{x}_{p,k-1}}{t_k-t_{k-1}}\right)\cdot \xi_{h,k}(\mathbf{x}_{p,k}) \\
- \frac{t_{k+1}-t_{k-1}}{2}\left[\frac{\boldsymbol{\sigma}(\mathbf{f}_{p,k})}{\rho_{p,k}} : \nabla\xi_{h,k}(\mathbf{x}_{p,k}) + b_k(\mathbf{x}_{p,k})\cdot\xi_{h,k}(\mathbf{x}_{p,k})\right]\Bigg\},
\end{aligned}
\tag{3.86}
$$

where

$$
\xi_{h,k}(\mathbf{x}) = \sum_{a=1}^{N} \xi_{a,k} N_{a,k}(\mathbf{x}) \tag{3.87}
$$

are discrete admissible virtual displacements. We note that equation (3.86) can alternatively be obtained by inserting the spatial discretization into the semi-discrete Euler-Lagrange equations (3.66) directly. Enforcing stationarity with respect to all variations ξ_h we obtain

$$
\frac{2}{t_{k+1}-t_{k-1}}\left(M_k\frac{\mathbf{x}_{k+1}-\mathbf{x}_k}{t_{k+1}-t_k}-p_k\right) = f_k\,, \tag{3.88}
$$

where $\mathbf{x}_k \equiv \{\mathbf{x}_{1,k},\ldots,\mathbf{x}_{N,k}\}$ is the nodal coordinate array at time t_k,

$$
p_{k,a} = \sum_{p=1}^{M} m_p \frac{\mathbf{x}_{p,k}-\mathbf{x}_{p,k-1}}{t_k-t_{k-1}} N_{a,k}(\mathbf{x}_{p,k}) \tag{3.89}
$$

is linear momentum of node a at time t_k,

$$M_{k,ab} = \sum_{p=1}^{M} m_p N_{a,k}(\mathbf{x}_{p,k}) N_{b,k}(\mathbf{x}_{p,k})\, I \tag{3.90}$$

is the consistent mass matrix box for nodes a and b at time t_k, and

$$f_{k,a} = \sum_{p=1}^{M} [m_p b_k(\mathbf{x}_{p,k}) N_{a,k}(\mathbf{x}_{p,k}) - \upsilon_{p,k} \boldsymbol{\sigma}_k(\mathbf{f}_{p,k}) \nabla N_{a,k}(\mathbf{x}_{p,k})] \tag{3.91}$$

are the nodal out-of-balance forces. In the special case of backward-compatible shape functions (3.84), using identity (3.81b) eq. (3.88) bcomes

$$\frac{2}{t_{k+1} - t_{k-1}} M_k \left(\frac{\mathbf{x}_{k+1} - \mathbf{x}_k}{t_{k+1} - t_k} - \frac{\mathbf{x}_k - \mathbf{x}_{k-1}}{t_k - t_{k-1}} \right) = f_k \,, \tag{3.92}$$

which is a central-difference scheme.

The above equations define a finite-dimensional semi-discrete central-difference scheme that can be solved forward explicitly. This forward solution takes the form:

i) Initialization: Set $k = 0$, initialize material point volumes, densities, shape functions.

ii) Given $\mathbf{x}_{k-1}$, $\mathbf{x}_k$, ρ_k, solve (3.88) for the updated nodal coordinates, with the result:

$$\mathbf{x}_{k+1} = \mathbf{x}_k + (t_{k+1} - t_k) M_k^{-1} (p_k + \frac{t_{k+1} - t_{k-1}}{2} f_k) \,. \tag{3.93}$$

iii) Update the material point coordinates, volumes, mass densities according to

the identities:

$$\mathbf{x}_{p,k+1} = \varphi_{h,k->k+1}(\mathbf{x}_{p,k})\,, \tag{3.94a}$$

$$\upsilon_{p,k+1} = \upsilon_{p,k+1} \det \nabla\varphi_{h,k->k+1}(\mathbf{x}_{p,k})\,, \tag{3.94b}$$

$$\rho_{p,k+1} = \frac{m_p}{\upsilon_{p,k+1}}\,, \tag{3.94c}$$

$$\mathbf{f}_{p,k+1} = \nabla\varphi_{k\to k+1}(x_{p,k})\mathbf{f}_{p,k}\,. \tag{3.94d}$$

iv) Calculate shape functions $N_{a,k+1}(\mathbf{x}_{p,k+1})$ and derivatives $\nabla N_{a,k+1}(\mathbf{x}_{p,k+1})$

v) Reset $k \leftarrow k+1$. If $k = N$ exit. Otherwise go to (ii).

Again, this forward solution has the usual structure of explicit time-integration schemes in that the updated nodal coordinates are computed directly from the initial conditions at the beginning of the time step.

3.2.4 Inelastic solids

In addition to the preceding field equations of the motion for the elastic solid flows, we require a general constitutive framework within which to describe the inelastic processes of material. It is essential for the purpose of the optimal transportation structure that the resulting stress update algorithm derive from an incremental potential, or energy density, so that the incremental displacements be governed by a minimum principle. To this end, we adopt a standard constitutive update algorithm proposed by Radovitzky and Ortiz [40].

Assume the existence of a Helmholtz free energy density $A(\mathbf{F}, \mathbf{Q})$ per unit undeformed volume where $\mathbf{Q}$ is some suitable collection of internal variables, the first Piola-Kirchhoff stress tensor can be decomposed as an addition,

$$\mathbf{P} = \mathbf{P}^e + \mathbf{P}^v \,, \tag{3.95}$$

into an equilibrium part $\mathbf{P}^e$ and a viscous part $\mathbf{P}^v$. The equilibrium stress follows from Coleman's relation as

$$\mathbf{P}^e = A_{,\mathbf{F}}(\mathbf{F}, \mathbf{Q}) \,. \tag{3.96}$$

Likewise the viscosity law $\mathbf{P}^v$ is supposed to derive from a potential if there exists a function $\phi(\dot{\mathbf{F}}, \mathbf{F}, \mathbf{Q})$ such that

$$\mathbf{P}^v = \phi_{,\dot{\mathbf{F}}}(\dot{\mathbf{F}}, \mathbf{F}, \mathbf{Q}) \,. \tag{3.97}$$

In order to determine the evolution of the internal variables, suitable kinetic equations must be supplied. Assuming that the rate of the internal processes is determined solely by the local thermodynamic state, the general form of the kinetic equation is

$$\dot{\mathbf{Q}} = f(\mathbf{F}, \mathbf{Q}) \,. \tag{3.98}$$

Additionally,

$$\mathbf{Y} = -A_{,\mathbf{Q}}(\mathbf{F}, \mathbf{Q}) \tag{3.99}$$

are the thermodynamic 'forces' conjugate to $\mathbf{Q}$. The kinetic relations are said to

derive from an inelastic potential if there exists a differentiable function $\Psi(\mathbf{Y}, \mathbf{Q})$ such that

$$\dot{\mathbf{Q}} = \Psi_{,\mathbf{Y}}(\mathbf{Y}, \mathbf{Q})\,. \tag{3.100}$$

Furthermore, introduce the dual potential $\Psi^*(\dot{\mathbf{Q}}, \mathbf{Q})$ by recourse to the Legendre transformation

$$\Psi^*(\dot{\mathbf{Q}}, \mathbf{Q}) = \mathbf{Y} \cdot \dot{\mathbf{Q}} - \Psi(\mathbf{Y}, \mathbf{Q})\,. \tag{3.101}$$

Then, one has

$$\mathbf{Y} = \Psi^*_{,\dot{\mathbf{Q}}}(\dot{\mathbf{Q}}, \mathbf{Q})\,, \tag{3.102}$$

which constitutes a restatement of the kinetic equations (3.100). Suppose within a generic time interval $[t_k, t_{k+1}]$, let the initial state $(\mathbf{F}_k, \mathbf{Q}_k)$ and the updated deformations $\mathbf{F}_{k+1}$ be given, finally we can define the incremental energy density as

$$\begin{aligned} W(\mathbf{F}_{k+1}; \mathbf{F}_k, \mathbf{Q}_k) = (t_{k+1} - t_k)\phi\left(\frac{\mathbf{F}_{k+1} - \mathbf{F}_k}{t_{k+1} - t_k}; \mathbf{F}_k\right) \\ + \min_{\mathbf{Q}_{k+1}} \left\{ A(\mathbf{F}_{k+1}, \mathbf{Q}_{k+1}) - A(\mathbf{F}_k, \mathbf{Q}_k) + (t_{k+1} - t_k)\Psi^*\left(\frac{\mathbf{Q}_{k+1} - \mathbf{Q}_k}{t_{k+1} - t_k}; \mathbf{Q}_k\right)\right\}\,. \end{aligned} \tag{3.103}$$

Minimization with respect to $\mathbf{Q}_{k+1}$ gives the condition

$$\mathbf{Y}_{k+1} = \Psi^*_{,\dot{\mathbf{Q}}}\left(\frac{\mathbf{Q}_{k+1} - \mathbf{Q}_k}{t_{k+1} - t_k}; \mathbf{Q}_k\right)\,. \tag{3.104}$$

In accordance with (3.102), and the variation of W with respect to $\mathbf{F}_{k+1}$ implies that

$$\mathbf{P}_{k+1} = \frac{\partial W(\mathbf{F}_{k+1}; \mathbf{F}_k, \mathbf{Q}_k)}{\partial \mathbf{F}_{k+1}} = \frac{\partial W_k(\mathbf{F}_{k+1})}{\partial \mathbf{F}_{k+1}}\,, \tag{3.105}$$

where $W_k(\mathbf{F}_{k+1})$ denotes $W(\mathbf{F}_{k+1}; \mathbf{F}_k, \mathbf{Q}_k)$.

Redefine the incremental energy density as a functional of the gradient of the incremental deformation per unit deformed volume

$$\begin{aligned} w_k(\nabla\varphi_{k\to k+1}) = (t_{k+1}-t_k)\phi\left(\frac{\nabla\varphi_{k\to k+1}}{t_{k+1}-t_k}\right) \\ + \min_{\mathbf{q}_{k+1}}\left\{A_k(\nabla\varphi_{k\to k+1}, \mathbf{q}_{k+1}) + (t_{k+1}-t_k)\Psi^*\left(\frac{\mathbf{q}_{k+1}-\mathbf{q}_k}{t_{k+1}-t_k}; \mathbf{q}_k\right)\right\}\,. \end{aligned} \tag{3.106}$$

where $\mathbf{q}(x,t) \equiv \mathbf{Q}\circ\varphi^{-1}$.

As shown by Radovitzky and Ortiz in [40], there exists a potential energy

$$\Phi[\varphi_{k\to k+1}] = \int\left\{\frac{\rho_k}{2}\frac{\left|\varphi_{k\to k+1}-\varphi^{\text{pre}}_{k\to k+1}\right|^2}{(t_{k+1}-t_k)^2} + w_k(\nabla\varphi_{k\to k+1}) - \rho_k\psi(\mathbf{x}, t_k)\right\}d\mathbf{x}\,. \tag{3.107}$$

such that its minimizer actually is the solution for the equivalent static problem from $t_k \to t_{k+1}$,

$$\rho_k\frac{\varphi_{k\to k+1}-\varphi^{\text{pre}}_{k\to k+1}}{(t_{k+1}-t_k)^2} - \nabla\cdot\boldsymbol{\sigma}_k = \rho_k\mathbf{b}_k\,, \tag{3.108}$$

where $\varphi^{\text{pre}}_{k\to k+1} = \text{id} + (\text{id} - \varphi_{k\to k-1})$. The equation (3.108) is equivalent to the time discrete motion equation (3.68) for elastic solid flows and shows the result of the competition between the inertia and the internal energy of the flow but with dissipations.

Hence analogously to (3.85), now the total discrete action for a general inelastic solid flow becomes

$$A_h(\mathbf{f}_{h,1},\ldots,\mathbf{f}_{h,N-1}) = \sum_{k=0}^{N-1}\sum_{p=1}^{M} m_p \Big\{ \frac{1}{2}\frac{|\mathbf{x}_{p,k+1}-\mathbf{x}_{p,k}|^2}{(t_{k+1}-t_k)^2} + \frac{1}{2}\left[\big(w_{k-1}(\mathbf{f}_{p,k})-\psi(\mathbf{x}_{p,k})\big)+\big(w_k(\mathbf{f}_{p,k+1})-\psi(\mathbf{x}_{p,k+1})\big)\right] \Big\}(t_{k+1}-t_k)\,. \tag{3.109}$$

Consequently nothing needs to be changed for the algorithm except now the stress updates are given by the minimization of the incremental energy density and additional updates needed for the internal variables. This solution takes the form

i) Initialization: Set $k = 0$, initialize material point volumes, densities, shape functions.

ii) Given $\mathbf{x}_{k-1}$, $\mathbf{x}_k$, ρ_k and $\mathbf{f}_k$, solve (3.88) for the updated nodal coordinates, with the result:

$$\mathbf{x}_{k+1} = \mathbf{x}_k + (t_{k+1}-t_k)M_k^{-1}(p_k + \frac{t_{k+1}-t_{k-1}}{2}f_k)\,, \tag{3.110}$$

where $\boldsymbol{\sigma}_k$ in f_k is computed from the minimization of the incremental energy density functional $w_{k-1}(\mathbf{f}_{p,k})$.

iii) Update the material point coordinates, volumes, mass densities according to

the identities:

$$\mathbf{x}_{p,k+1} = \varphi_{h,k->k+1}(\mathbf{x}_{p,k})\,, \tag{3.111a}$$

$$\upsilon_{p,k+1} = \upsilon_{p,k+1} \det \nabla\varphi_{h,k->k+1}(\mathbf{x}_{p,k})\,, \tag{3.111b}$$

$$\rho_{p,k+1} = \frac{m_p}{\upsilon_{p,k+1}}\,, \tag{3.111c}$$

$$\mathbf{f}_{p,k+1} = \nabla\varphi_{k\to k+1}(x_{p,k})\mathbf{f}_{p,k}\,. \tag{3.111d}$$

plus variational constitutive updates to update internal variables $\mathbf{q}_{k+1}$.

iv) Calculate shape functions $N_{a,k+1}(\mathbf{x}_{p,k+1})$ and derivatives $\nabla N_{a,k+1}(\mathbf{x}_{p,k+1})$

v) Reset $k \leftarrow k+1$. If $k = N$ exit. Otherwise go to (ii).

Chapter 4

Analysis of the Optimal Transportation Method

In this chapter, we study the convergence and stability of the *Optimal Transportation Method*. A compressive isothermal plane shockwave problem with a closed-form exact analytical solution is demanded to verify the rate of convergence of the velocity field and density field computed from *OTM*. The problem is simulated in one dimension and two dimension as well as a fully three dimensional calculation. The stability of *OTM* is also studied by a simple tension/compression test for a one-dimensional elastic bar.

4.1 Study of Convergence

A verification test of the *OTM* is provided by the problem of a compressive isothermal plane shockwave traveling down a highly compressible material [40]. The accuracy and rates of convergence of *OTM* may be exhibited by this benchmark example.

4.1.1 Governing equations of compressible viscous material

Consider a reference configuration of a continuous body $B_0 \subset \mathbb{R}^d$ at $t = 0$ undergoing a motion described by a time-dependent deformation mapping $\boldsymbol{\varphi} : B_0 \times [0, T] \mapsto \mathbb{R}^d$. Material particles in the reference configuration are denoted by $\mathbf{X} \in B_0$ mapping to points $\mathbf{x} = \boldsymbol{\varphi}(\mathbf{X}, t)$ in the deformed configuration $B_t = \boldsymbol{\varphi}(B_0, t)$. Then the motion of the body is subject to the solution of a general initial value problem in Lagrangian form,i.e.,

$$\mathbf{F}(\mathbf{X}, t) = \nabla_0 \boldsymbol{\varphi}(\mathbf{X}, t)\,, \qquad \text{in } B_0 \times [0, T]\,, \tag{4.1a}$$

$$\rho_0 \ddot{\boldsymbol{\varphi}} = \nabla_0 \cdot \mathbf{P} + \rho_0 \mathbf{B}\,, \qquad \text{in } B_0 \times [0, T]\,, \tag{4.1b}$$

$$\boldsymbol{\varphi}(X, t) = \bar{\boldsymbol{\varphi}}(X, t)\,, \qquad \text{on } (\partial B_0)_1 \times [0, T]\,, \tag{4.1c}$$

$$\mathbf{P} \cdot \mathbf{N} = \bar{\mathbf{T}}\,, \qquad \text{on } (\partial B_0)_2 \times [0, T]\,, \tag{4.1d}$$

$$\boldsymbol{\varphi}(X, 0) = \boldsymbol{\varphi}^{(0)}(\mathbf{X})\,, \qquad \text{in } B_0\,, \tag{4.1e}$$

$$\dot{\boldsymbol{\varphi}}(\mathbf{X}, 0) = \dot{\boldsymbol{\varphi}}^{(0)}(\mathbf{X})\,, \qquad \text{in } B_0\,, \tag{4.1f}$$

where∇_0 denotes the partial derivatives with respect to $\mathbf{X}$, $\mathbf{F}$ is the deformation gradient, $\dot{\boldsymbol{\varphi}}$ and $\ddot{\boldsymbol{\varphi}}$ are the material velocity and acceleration respectively, ρ_0 is the reference mass density, $\mathbf{P}$ is the first Piola-Kirchhoff stress tensor, and $\mathbf{B}$ denotes the body force in the reference configuration. The boundary of domain B_0 is $\partial B_0 = (\partial B_0)_1 \cup (\partial B_0)_2$ and $(\partial B_0)_1 \cap (\partial B_0)_2 = \emptyset$, where $(\partial B_0)_1$ is the Dirichlet boundary and prescribed the displacement boundary conditions $\bar{\boldsymbol{\varphi}}$, and $\bar{\mathbf{T}}$ is the external forces along the Neumann boundary $(\partial B_0)_2$. Equation (4.1b) gives the conservation of the

linear momentum of the body. The Cauchy stress tensor follows from $\mathbf{P}$ in the form

$$\boldsymbol{\sigma} = J^{-1}\mathbf{P}\mathbf{F}^{T}\,, \tag{4.2}$$

where

$$J = \det(\mathbf{F}) \tag{4.3}$$

is the Jacobian of the deformation.

The compressible Newtonian fluids provide the foremost example of a material with viscosity. In this case the Newtonian viscosity law possesses a potential structure (3.97) as the constitutive framework introduced in §3.2.4, and the viscous potential is given by

$$\phi = \eta J \mathbf{d}^{\mathrm{dev}} \cdot \mathbf{d}^{\mathrm{dev}}\,, \tag{4.4}$$

where

$$\mathbf{d} = \mathrm{sym}(\dot{\mathbf{F}}\mathbf{F}^{-T}) \tag{4.5}$$

is the rate of deformation tensor, $\mathbf{d}^{\mathrm{dev}}$ is its deviatoric component and η is the viscosity of the fluid. It follows

$$\mathbf{P}^{v} = \frac{\partial \phi}{\partial \dot{\mathbf{F}}} = J\boldsymbol{\sigma}^{v}\mathbf{F}^{-T}\,, \tag{4.6}$$

where

$$\boldsymbol{\sigma}^{v} = 2\eta\mathbf{d}^{\mathrm{dev}} \tag{4.7}$$

is the viscous part of the Cauchy stress tensor. Such that the constitutive equation

of a Newtonian fluid is given by

$$\boldsymbol{\sigma} = p(J)\mathbf{I} + 2\eta\mathbf{d}^{\text{dev}}\,, \tag{4.8}$$

where for a compressible fluid we assume p is dependent only on the volumetric part of the deformation,that means the free energy assumed to depend on deformation only through the Jacobian of the deformation, i.e,

$$A = A(J, T)\,, \tag{4.9}$$

which follows from (3.96)

$$p(J) = J^{-1}\mathbf{P}^e\mathbf{F}^T = J^{-1}A_{,\mathbf{F}}\mathbf{F}^T = A_{,J}\,. \tag{4.10}$$

4.1.2 Analytical solution for isothermal plane-shock propagation

Next we specialize the above relations to a plane-shock geometry, see Fig. 4.1. Although

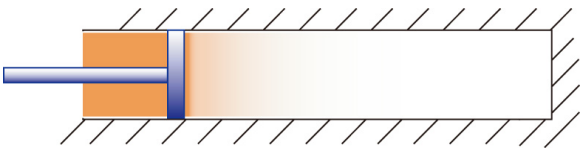

Figure 4.1: Isothermal compressive plane-shock geometry.

the tests concern compressive waves traveling down a shock tube, for solids we carry out the analysis in Lagrangian setting. Suppose in three-dimensional Euclidean

space, the coordinates of any material particles in the reference configuration be $\mathbf{X} = (X_1, X_2, X_3)^T$, let X_1 be the components in the direction of propagation of the shock. Assume that the deformation is uniaxial and fully described by the motion $\boldsymbol{\varphi}(\mathbf{X}, t) = (\varphi_1(X_1, t), X_2, X_3)^T$. The corresponding deformation gradient therefore is of the form

$$\mathbf{F} = \begin{pmatrix} \varphi_{1,1} & 0 & 0 \\ 0 & 1 & 0 \\ 0 & 0 & 1 \end{pmatrix} \tag{4.11}$$

and the Jacobian of the deformation is identical to the first component of $\mathbf{F}$

$$J = \varphi_{1,1}\,. \tag{4.12}$$

The equation of conservation of linear momentum of the propagation of the plane-shock reduces to

$$\rho_0 \ddot{\varphi}_1 = P_{11,1}\,, \tag{4.13}$$

where P_{11} follows from the Newtonian fluid constitutive equations (3.95),(4.6) and (4.8) in the form

$$P_{11} = p(\varphi_{1,1}) + 2\eta d_{11}^{\mathrm{dev}}\,. \tag{4.14}$$

Here we only consider the isothermal case such that the free energy A is not dependent on the temperature either. A particular choice of the free energy may be

$$A(J) = \frac{K}{4}\big(J^2 - 2\log(J) - 1\big)\,, \tag{4.15}$$

where K is the bulk modulus of the undeformed material, which gives

$$p(J) = \frac{K}{2}(J - J^{-1})\,. \tag{4.16}$$

The rate of deformation evaluates to

$$\mathbf{d} = \mathrm{sym}(\dot{\mathbf{F}}\mathbf{F}^{-1}) = \begin{pmatrix} \frac{\dot{\varphi}_{1,1}}{\varphi_{1,1}} & 0 & 0 \\ 0 & 0 & 0 \\ 0 & 0 & 0 \end{pmatrix}, \tag{4.17}$$

and its deviatoric part to

$$\mathbf{d}^{\mathrm{dev}} = \mathbf{d} - \frac{1}{3}\mathrm{tr}(\mathbf{d})\mathbf{I} = \begin{pmatrix} \frac{2\dot{\varphi}_{1,1}}{3\varphi_{1,1}} & 0 & 0 \\ 0 & -\frac{\dot{\varphi}_{1,1}}{3\varphi_{1,1}} & 0 \\ 0 & 0 & -\frac{\dot{\varphi}_{1,1}}{3\varphi_{1,1}} \end{pmatrix}. \tag{4.18}$$

Inserting these expressions into (4.13) leads to the governing equation

$$\rho_0 \ddot{\varphi}_1 = \Big[p(\varphi_{1,1}) + \frac{4\eta}{3}\frac{\dot{\varphi}_{1,1}}{\varphi_{1,1}}\Big]_{,1}, \tag{4.19}$$

and the analytical solution takes the form

$$\frac{\varphi_1(X_1,t) - X_1}{L} = f\big(\frac{X_1 - Ct}{L}\big)\,, \tag{4.20}$$

where

$$f(\frac{X_1 - Ct}{L}) = \big[\frac{J^+ + J^-}{2} - 1\big]\frac{X_1 - Ct}{L} + (J^+ - J^-)\big\{\log\big[\cosh\big(\frac{X - Ct}{2L}\big)\big] - \log 2\big\}\,, \tag{4.21a}$$

$$C = \sqrt{\frac{K}{2\rho_0}\big(1 + \frac{1}{J^- J^+}\big)}\,, \tag{4.21b}$$

$$L = \frac{8\eta C}{3K}\frac{J^- J^+}{J^+ - J^-}\,, \tag{4.21c}$$

to which we introduced the boundary conditions,

$$\lim_{X \to \pm\infty} J(X) = J^{\pm}\,. \tag{4.22}$$

Note C is some propagation velocity and L is a measure of the width of the shock. Hence the explicit expressions for the density field, deformation mapping and velocity field reveal as

$$\rho(X_1, t) = \rho_0 / J\,, \tag{4.23a}$$

$$\varphi_1(X_1, t) = X_1 + \big[\frac{J^+ + J^-}{2} - 1\big](X_1 - Ct) + L(J^+ - J^-)\big\{\log\big[\cosh\big(\frac{X_1 - Ct}{2L}\big)\big] - \log 2\big\}\,, \tag{4.23b}$$

$$\dot{\varphi}_1 = \frac{C}{2}\big\{2 - (J^+ + J^-) - (J^+ - J^-)\tanh\big(\frac{X_1 - Ct}{2L}\big)\big\}\,. \tag{4.23c}$$

The evolution of the analytical density field $\rho_(X_1, t)$, the displacement field $u_1(X_1, t) = \varphi_1 - X_1$, the velocity $\dot{\varphi}_1$ and the acceleration $\ddot{\varphi}_1$ are shown in Fig. 4.2 for the following

parameters

Table 4.1: Parameters used in simulations of isothermal compression wave

ρ_0	K	η	J^+	J^-
1.0	1.0	0.0025	1.0	0.1

In this case, the analytic computed value for the shock velocity is

$$C = \sqrt{\frac{K}{2\rho_0}\big(1 + \frac{1}{J^- J^+}\big)} = 2.3452\,, \tag{4.24}$$

and the corresponding computed shock thickness is

$$L = \frac{8\eta C}{3K}\frac{J^- J^+}{J^+ - J^-} = 1.737 \times 10^{-3}\,. \tag{4.25}$$

4.1.3 Dynamic convergence tests

The problem is solved numerically using *OTM*. An explicit time integration is subsequently carried out. The integration parameters for the explicit Newmark's algorithm is set to be $\beta = 0$ and $\gamma = \frac{1}{2}$. In this case, a stable time step is chosen as a fraction of the minimum between the Courant limit and an estimated time step [40]

$$\Delta t = f * \min\big\{\frac{h_{\min}}{C}, \frac{\rho_0 h_{min}^2}{\eta}\big\}\,, \tag{4.26}$$

where $f \sim 0.1 - 0.2$ and $h_{\min}$ is the minimum nodal space. The length of the domain of the analysis is $l = 25L$, where L is the width of the shock. We start the simulation

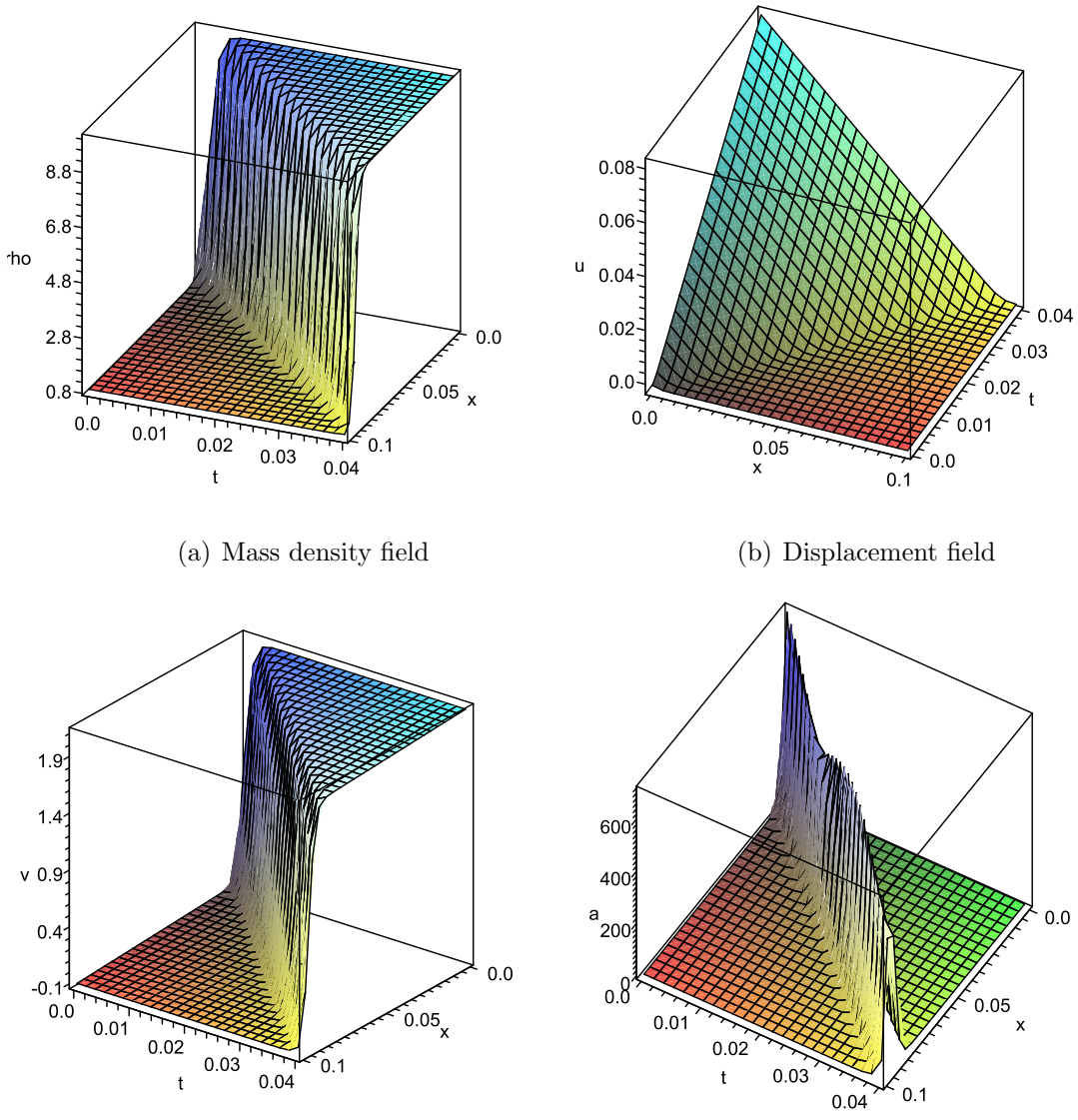

(a) Mass density field

(b) Displacement field

(c) Velocity field

(d) Acceleration field

Figure 4.2: Evolution of the velocity, displacement, density, and acceleration fields from the analytical solutions for isothermal compressive shockwave.

as the center of the shock wave reaches the entry. The problem is modeled after the analytical solutions derived in §4.1.2, such that the initial and boundary conditions can be calculated from equations (4.23). Fig. 4.3 shows the numerical results for the evolution of the velocity and displacement fields of the isothermal shock wave propagation in the tube calculated with the parameters in table 4.1. The accuracy

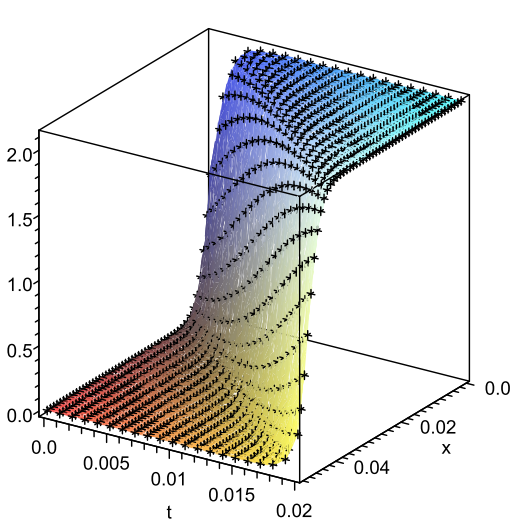

(a) Velocity field

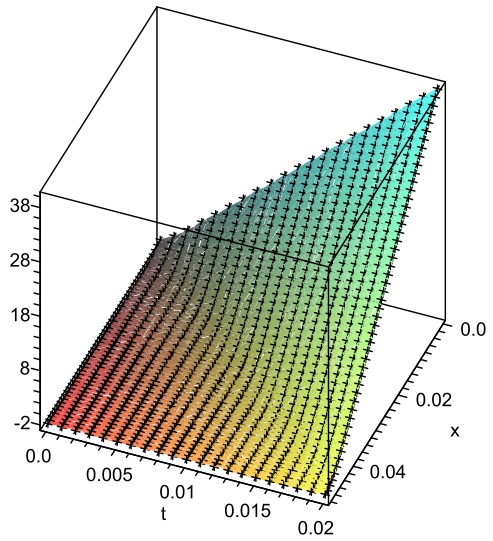

(b) Displacement field

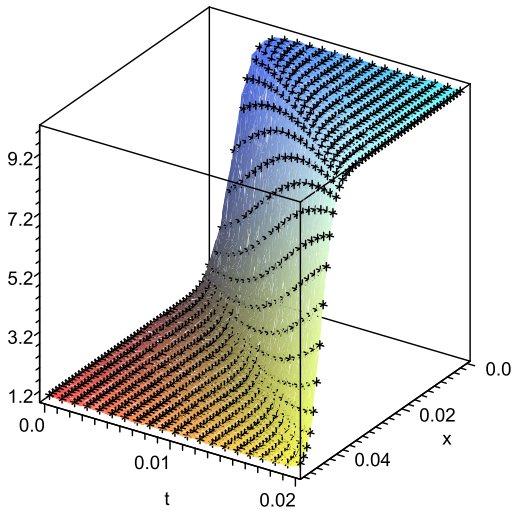

(c) Density field

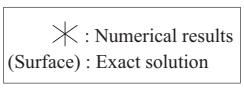

(d)

Figure 4.3: Comparison of the numerical results and exact solutions for the velocity, displacement, and density fields of the isothermal compressive shockwave.

and rates of convergence of the OTM may be exhibited with the aid of conventional convergence plots. Fig. 4.5 and Fig. 4.4 show the convergence curves obtained in the isothermal case with explicit time integrator. The error is measured using the norm defined in space $C\big([a,b];L^1(\mathbb{R}^n;[0,\infty))\big)$ for difference between the exact solutions and the OTM solutions of the density, and the one in $C\big([a,b];L^2(\mathbb{R}^n;\mathbb{R}^n)\big)$ for the velocity difference, namely

$$||\rho-\rho_h|| = \max_{t\in[a,b]}\Big\{\int_{B_0}||\rho-\rho_h||dX\Big\}, \tag{4.27a}$$

$$||v-v_h|| = \max_{t\in[a,b]}\Big\{\big(\int_{B_0}||v-v_h||^2dX\big)^{\frac{1}{2}}\Big\}. \tag{4.27b}$$

From this benchmark example it can be observed even with small number of degree of freedoms the OTM is quite accurate, the error measures remain below 10^{-7} throughout the simulation. The convergence test of the velocity field shows the OTM is better than quadratic convergence. The same problem is also simulated in 2D and 3D. Fig. 4.7 shows the shock wave propagation in the reference and deformed configuration in 2D. In the 3D case, total 2907 nodes and 14,700 material points are used, see Fig. 4.9, which shows a sequence of snapshots of the evolution of the deformed configuration when the shockwave traveling down a cylinder.

4.2 Stability

The stability of particle methods is an essential problem as well as the accuracy and robustness. As Belytschko et al. [5] pointed out, there are two major distinct

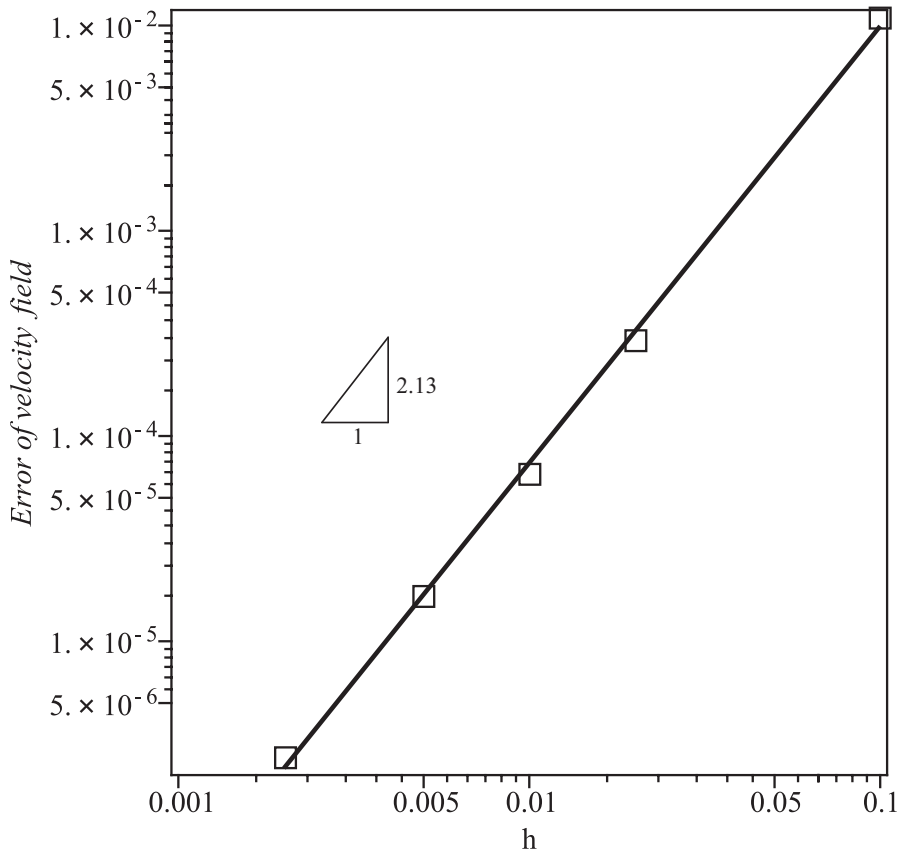

Figure 4.4: Convergence of the velocity field in one dimension. The rate is indicated by the value 2.13.

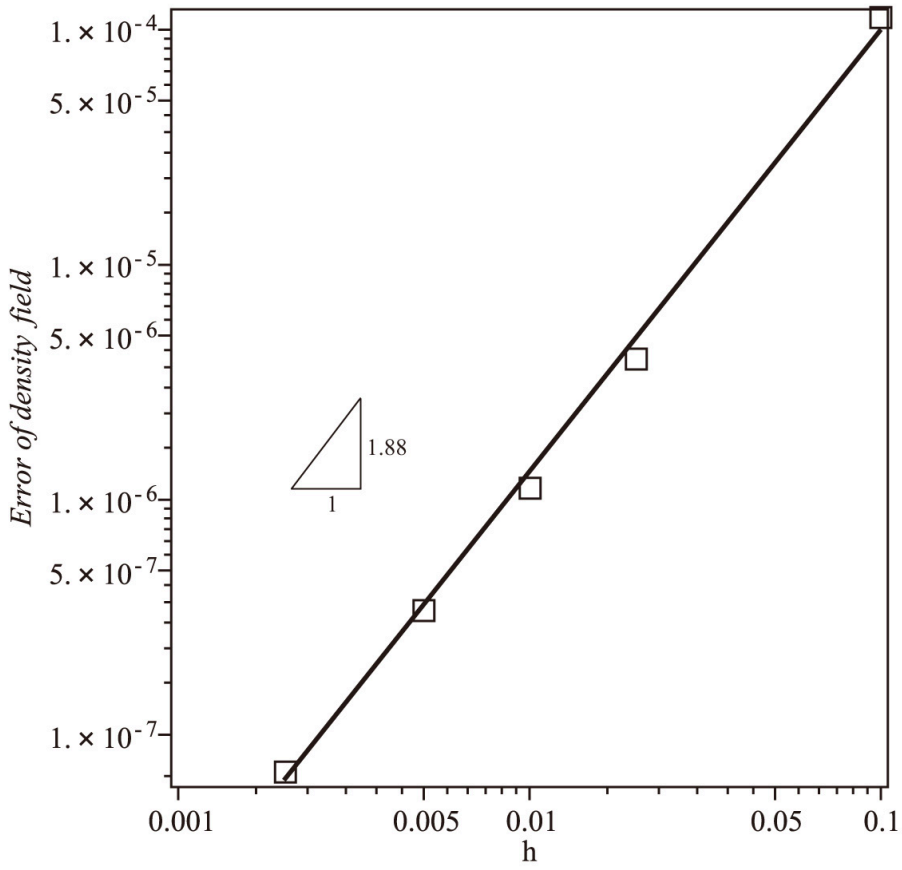

Figure 4.5: Convergence of the density field in one dimension. The rate is indicated by the value 1.88.

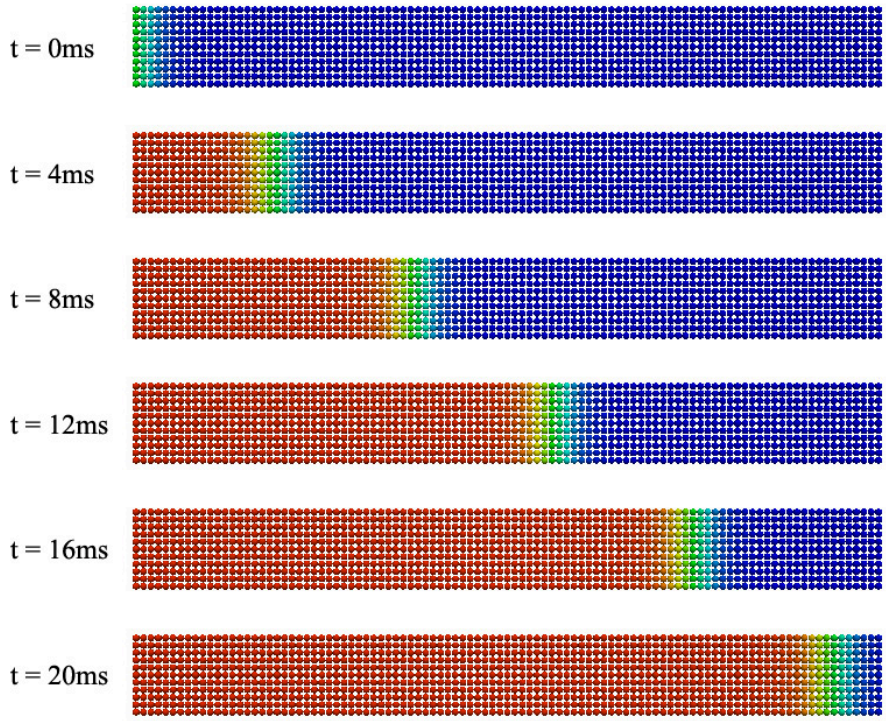

Figure 4.6: Propagation of a compressive isothermal shockwave in two dimensions. Velocity field at different moment. Reference configuration.

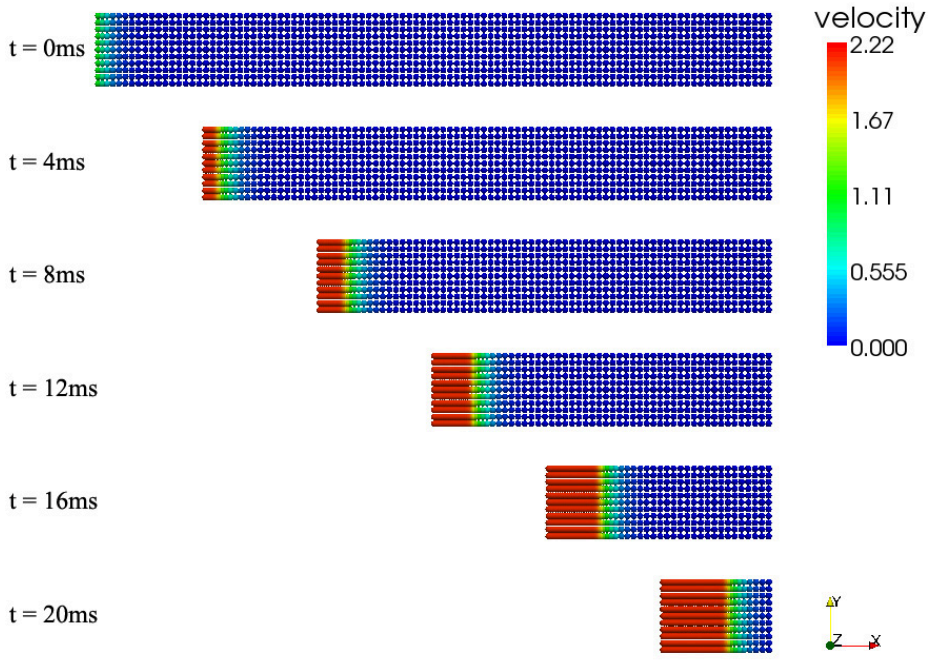

Figure 4.7: Propagation of a compressive isothermal shockwave in two dimensions. Velocity field at different moment. Deformed configuration.

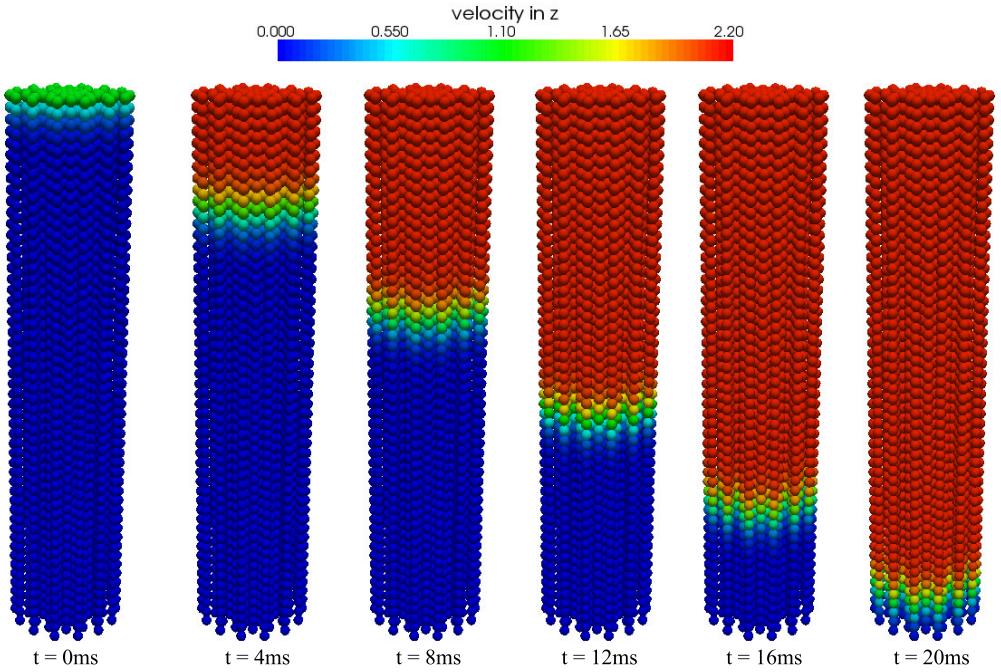

Figure 4.8: Propagation of a compressive isothermal shockwave down a cylinder. Velocity field at different moment. Reference configuration.

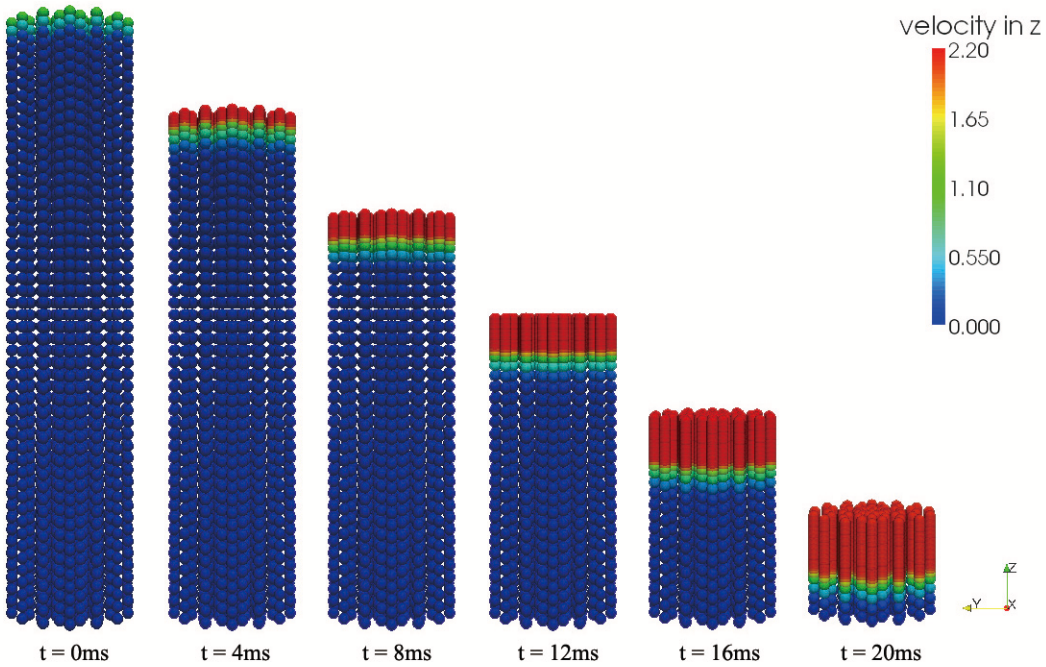

Figure 4.9: Propagation of a compressive isothermal shockwave down a cylinder. Velocity field at different moment. Deformed configuration.

numerical instabilities in meshless methods: (i) a high-frequency instability which results from the rank deficiency of the discrete divergence operator; (ii) a tensile instability which results from the interaction of the second derivative of kernel and the tensile stress, it occurs even in one-dimensional plane response.In this section, we will try to verify the OTM does not exhibit any of these instabilities based on the general stability analysis of particle methods by Belytschko et al. [5] and an excellent one-dimensional elastic tension and compression test.

4.2.1 General stability analysis

The tensile instability was first identified by Swegle [50] by a von Neumann stability analysis of the one-dimensional equation in SPH. Subsequently, Dyka et al. [15],[16] motivated by similar difficulties in finite elements, where under integration of the Galerkin form leads to spurious singular modes, recommended the insertion of additional quadrature points, called stress points to remove the instability due to rank deficiency.In [5], Belytschko et al. investigated a unified stability analysis for the meshless methods based on the eigenvalues of the dynamic system.

The semi-discretized free vibration equation for an undamped case can be written in the form

$$m_I \ddot{\mathbf{u}}_I = f_I^{\text{ext}} - f_I^{\text{int}}, \tag{4.28}$$

where m_I and $\mathbf{u}_I$ are the lumped mass and displacement of node I respectively, f_I^{ext} and f_I^{int} are the external and internal nodal force. Considering the Fourier form of a

perturbation in displacement,

$$\hat{\mathbf{u}}_I = g \exp(i\kappa I \Delta X - i\omega t)\,. \tag{4.29}$$

The perturbed equation is

$$m_I \ddot{\hat{\mathbf{u}}}_I = \hat{f}_I^{\text{ext}} - \hat{f}_I^{\text{int}}\,. \tag{4.30}$$

The eigenvalues ω^2 of the characteristic eigenproblem in (4.30) govern the stability of any dynamic systems. Then the stability of the system can thus be analyzed based on these eigenvalues. For instance the response is unstable if the imaginary part of ω is negative.

Recall that usually the kernel function is a function of the distance from the node,i.e.,

$$W_I(\mathbf{X}) = W(s,h) \quad \text{where } s = \begin{cases} ||X - X_I|| & \text{for Lagrangian kernel}\,, \\ ||x - x_I|| & \text{for Eulerian kernel}\,. \end{cases} \tag{4.31}$$

Belytschko et al. [5] observes that when the meshless method employs an Eulerian kernel, if the stress is positive, the imaginary part of the eigenvalues will be negative and results in the tensile instability identified by Swegle [50]. But with a Lagrangian kernel it does not exhibit the tensile instability regardless of the magnitude of the tensile stress since the eigenvalue now is independent on the stress. Fig. 4.10 shows an example of the stability region for Eulerian and Lagrange kernels. Further investigations for the numerical integration schemes in meshless methods including nodal

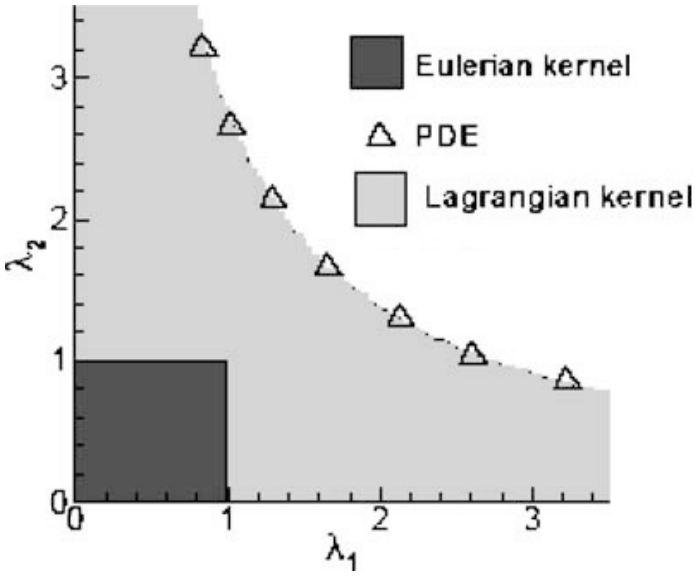

Figure 4.10: Example of the stable domain for the Eulerian and Lagrangian kernel compared to the stable domain for the PDE.

integration and stress point integration are conducted by this simple von Neumann analysis. It shows that the nodal integration, due to the rank deficiency of the discretization, exhibits a spurous singular mode since for a specific wave number the eigenvalue vanishes even with a Lagrangian kernel. However base on the result eigenvalues, the stress point integration scheme removes this problem by sampling the integrals at more quadrature points which usually are located at the barycenter of the Vorinio tessellation of the nodes. According to a similar analysis, since the *Optimal transportation* method uses an incremental updated Lagrangian kernel and an integration technique based on material points, we can show it therefore completely avoids the tensile instability and those due to the rank deficiency.

4.2.2 Numerical verification

In this section we will verify that the *OTM* does not exhibit any of these instabilities even with a nonuniform distribution of nodes by using a simple 1D elastic bar example. This example is also exploited by Dyka [15] to prove the stress point integration scheme removes the tensile instability in SPH. Fig. 4.11 depicts a simple elastic bar fixed at the left end B, free at the right end A. The right quarter of the bar is given an initial velocity of $v_0 = 5$m/s(tensile loading). Standard SPH methods cannot solve this problem due to tension instability that immediately developed. A spurious mode occurs when solving this problem by the EFG method with nodal integration due to the rank deficiency.

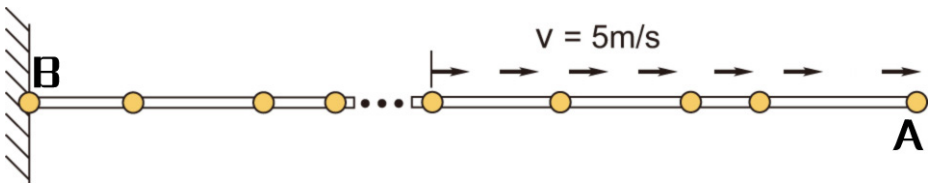

Figure 4.11: One-dimensional elastic bar fixed at point B given an initial velocity.

The problem is solved using the *OTM* with a general distribution of 100 particles. The bar is 0.1333m in length and made of Neohookean material. The material parameters are $\lambda = 115.3846$Gpa, $\mu = 76.9231$Gpa, $\rho = 7833$kg/m^3, and the wave speed can be calculated as $c = 5053.02$m/s. The explicit Newmark time integrator is used with a stable time step $\Delta t = 2.5 \times 10^{-8}$s. Fig. 4.12 indicates the displacement results of the right end A of the bar from standard finite element and the *OTM*. Fig. 4.13 compares the velocity field of point A from the standard FEM and the *OTM*. We note from this excellent test of stability in both tension and compression that the

major instabilities in particle method do not occur in *OTM*. No corrections or any kind of stabilization terms are needed for the extensive use of *OTM* for engineering problems.

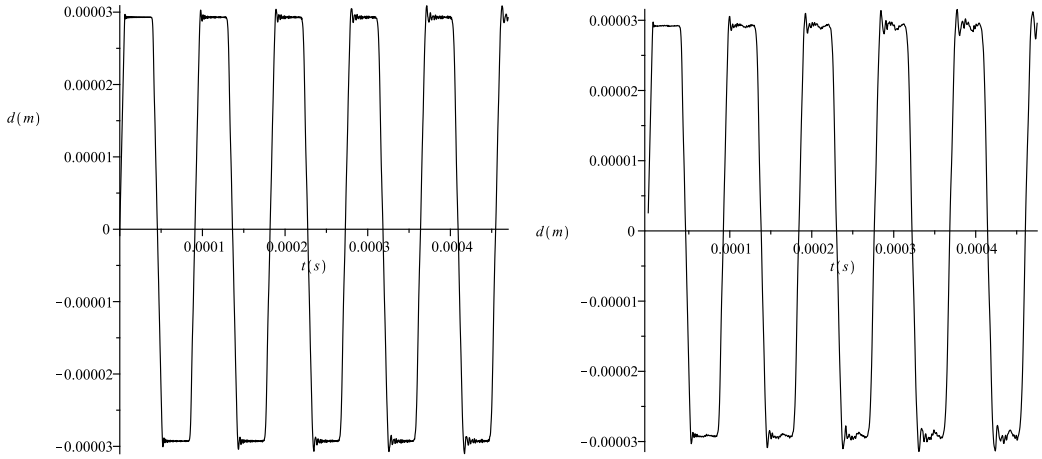

(a) FEM results (b) *OTM* results

Figure 4.12: Displacement history of the right end of the bar.

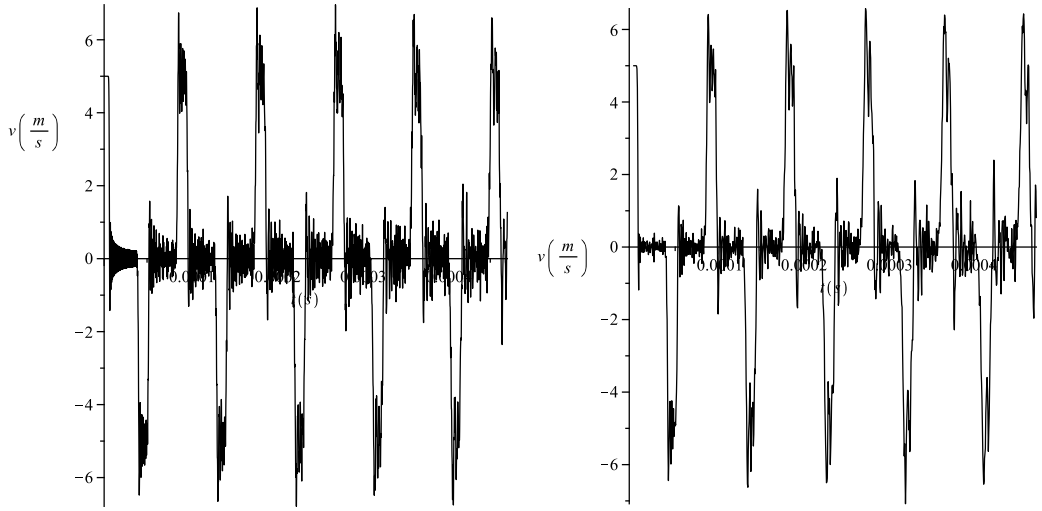

(a) FEM results (b) *OTM* results

Figure 4.13: Velocity history of the right end of the bar.

Chapter 5

Applications of the Optimal Transportation Method

A collection of applications designed to assess the performance, robustness, versality and capabilities of the *Optimal Transportation Method* is presented in this chapter. The first example is the Taylor-anvil impact test, which is a standard benchmark example to demonstrate the accuracy and effectiveness of numerical methods for capture strongly non-linear dynamic material behaviors. Next a series of full 3D meshless simulations for high velocity impact are presented. In order to simulation contact problems in meshless methods, we propose a novel meshless dynamic contact algorithm. The emphasis is in establishing the robustness and efficiency of *OTM* for handling solid flows with extremely large deformation, fast, transient loading and hydrodynamic phenomena.

5.1 Taylor Bar Impact Test

During World War II Taylor [51] proposed an analysis on specimens deformed at very high rates of strain to find the dynamic compressive strength of a material.

These experiments involved the propagation of plastic deformation as a wave process. Fig. 5.1 shows a specimen deformed dynamically, such as the one produced by the impact of the cylinder against a rigid wall. A cylinder projectile of length L impacts a target at a velocity U. At this moment, an elastic wave is faster than the plastic wave and moves at a wave speed C. This elastic compressional wave travels until it reaches the back surface of the projectile, reflects there, and then returns as a release wave. Then it returns toward the plastic wave, it interacts with it, and this marks the end of the deformation process. The stress within the region that has plastically deformed is assumed to be constant and equal to the yield stress of the material with that strain rate.

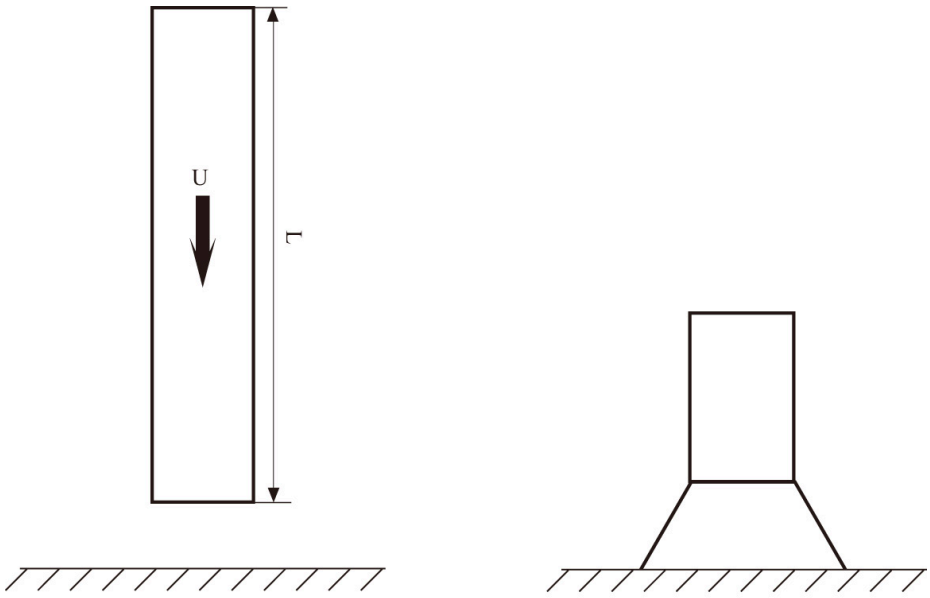

Figure 5.1: Dynamic deformation of a cylindrical specimen impact against a rigid wall.

The Taylor Impact test has become a standard procedure to verify the constitutive behavior of materials, and furnishes a convenient benchmark test to illustrate the capability of the numerical algorithms to simulate highly non-linear deformation of

elastoplastic bodies. To demonstrate the effectiveness and accuracy of our *Optimal Transportation* method for finite inelastic solid flows, the benchmark example of a Taylor anvil-impact test is used.

The rod is made of copper and initially has a radius of 3.2 mm and a length of 32.4 mm, which impacts normally a rigid, frictionless wall at 227 m/s, see Fig. 5.2. The material is assumed to be elastoplastic, von Mises J2 plasticity with linear isotropic hardening. The material constants are given as density $\rho = 8930$ kg/m^3, Young's modulus $E = 117$ Gpa, Poisson's ratio $\nu = 0.35$, initial yield stress $\sigma_y = 400$ Mpa and plastic modulus $E_t = 100$ Mpa. A full three-dimensional simulation is carried out to 80 μs,i.e., after this moment, the kinetic energy is totally transformed into plastic deformation.

The deformed configurations are shown in Fig. 5.3 at times t =20μs, 40μs and 80μs. In order to demonstrate the distribution of effective plastic strain and von Mises stress inside the body at different moments, in Fig. 5.4 and 5.5 we take a slice from the rod and show the exact distribution of these fields at times t =20 μs, 40μs and 80μs respectively. It is evidenced that the *Optimal transportation* method successfully captured the highly non-linear behaviour of the metal. Note that in the plastic region, the material points are trying to reorganize their neighbors and exhibit a very interesting self-adaptive capability.

This problem has also been investigated by many different numerical methods. For comparison, in Table 5.1 the final length of the rod, the final mushroom radius, the maximum effective strain and von Mises stress obtained by different methods are

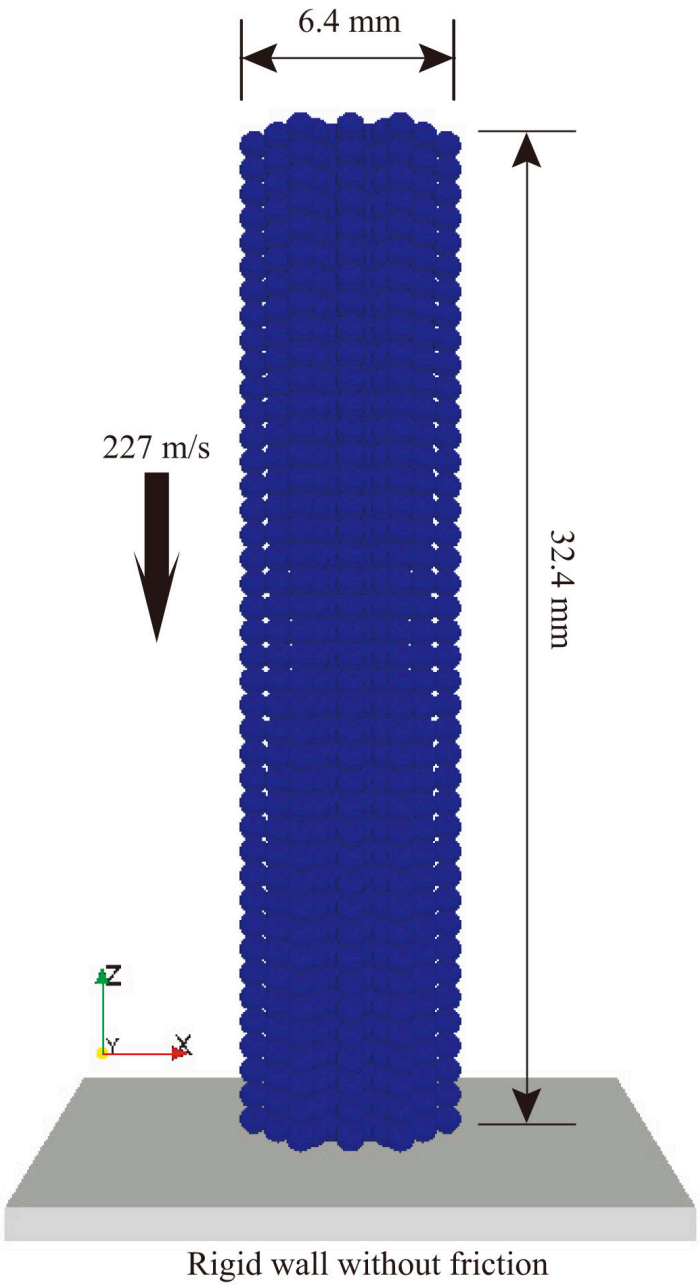

Figure 5.2: Taylor anvil impact test: initial condition and model parameters.

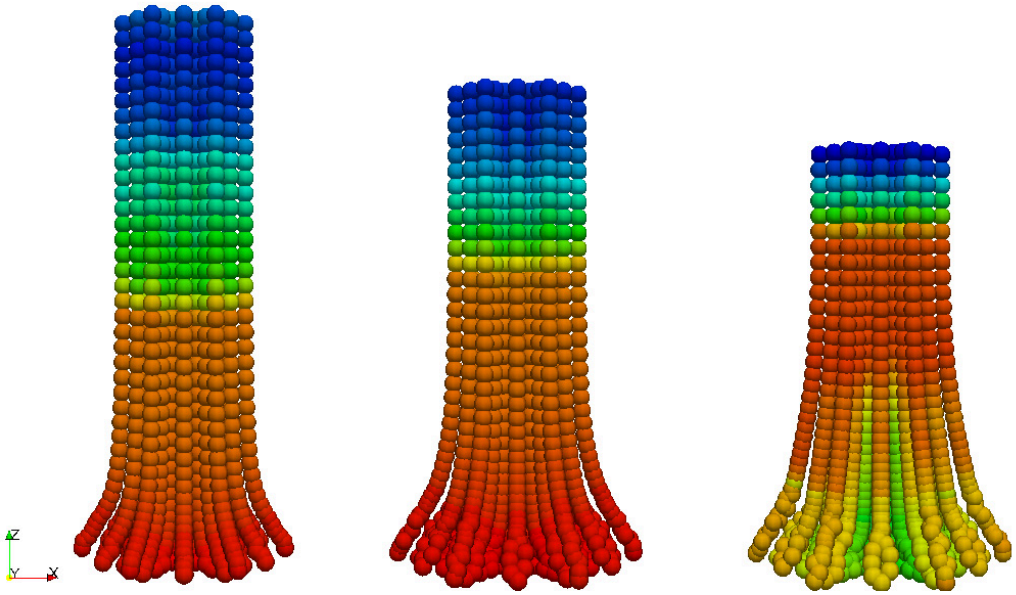

Figure 5.3: Taylor anvil impact test snapshots at 20, 40 and 80 μs.

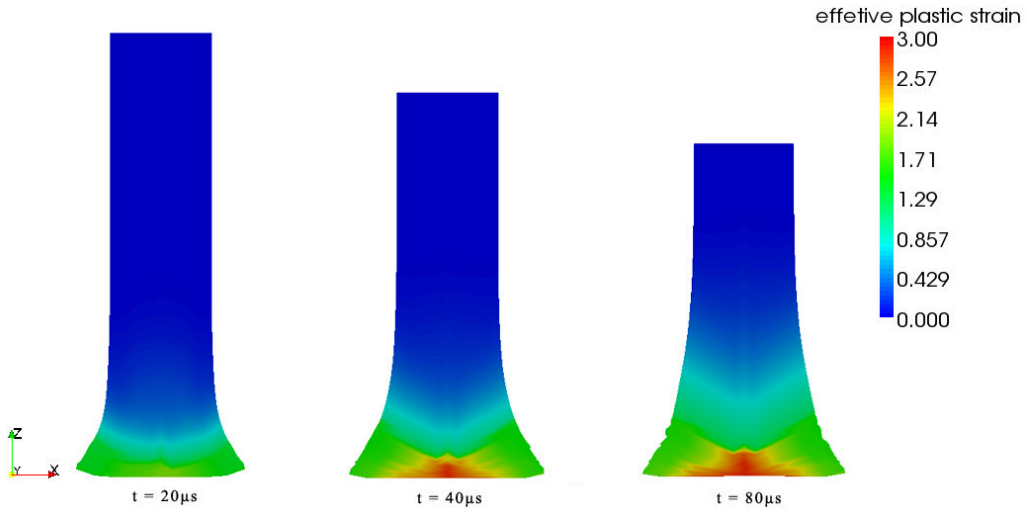

Figure 5.4: Distribution of the effective plastic strain in the rod at 20, 40 and 80 μs.

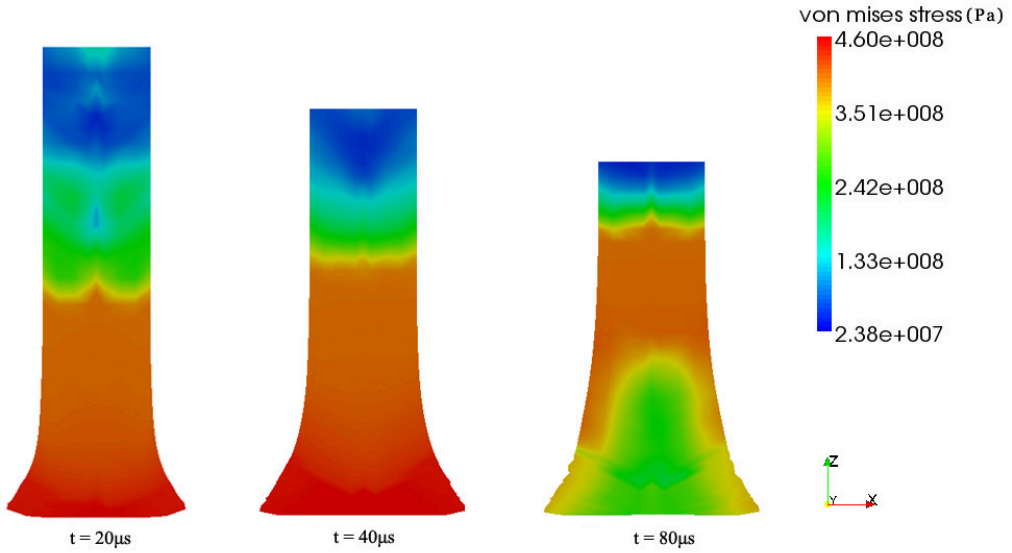

Figure 5.5: Distribution of the von Mises stress in the rod at 20, 40 and 80 μs.

listed. Fig. 5.6 shows the time history of the height of the rod. Note all the other results are calculated in the axisymmetric case. As expected the *Optimal transportation* method obtained an excellent agreement with the finite element results.

Table 5.1: Taylor anvil impact test:comparison of results

	Final length(mm)	Final mushroom radius(mm)	Max. effective plastic strain	Max. von Mises stress(Mpa)
Kamoulakis [25]	21.47-21.66	7.02-7.12	2.47-3.24	472-476
Zhu and Cescotto [55]	21.26-21.49	6.89-7.18	2.75-3.03	419-477
Camacho and Ortiz [11]	21.42-21.44	7.21-7.24	2.97-3.25	
OTM	21.43	6.8	3.0	474

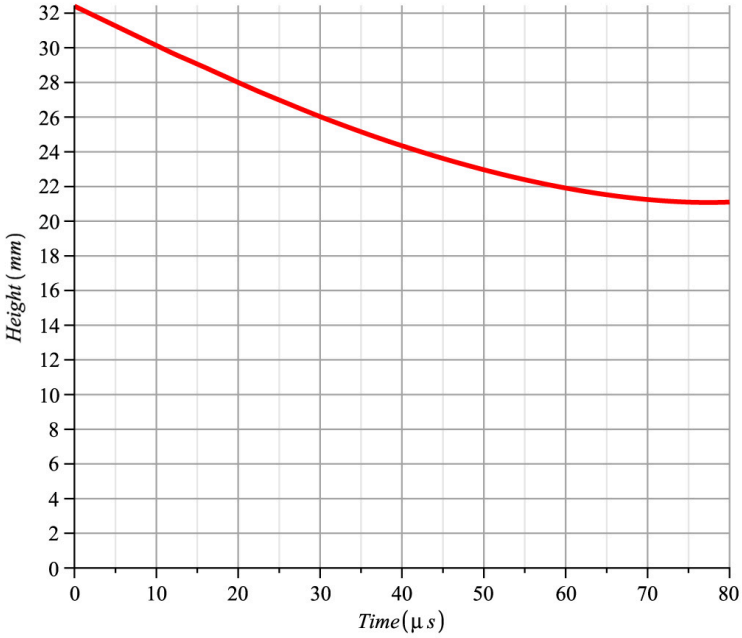

Figure 5.6: Time history of the height of the rod in Taylor impact.

5.2 High Velocity Impact Problems

5.2.1 Meshless Dynamic Contact algorithm

In impact problems Moving interfaces between media play an important role. In most cases, the contact region is unknown in advance and has to be detected during the computation. For the numerical calculations using Lagrangian grid methods, the boundaries of bodies are represented by a set of d-dimensional boundary cells. The contact is identified either by the penetration of "alien" boundary nodes through "friendly" boundary cells in the preliminary calculation, in which the contact is not taken into account, or by the approach of the boundaries to a prescribed small distance which the fact is detected by the pairwise check of the mutual positions of boundary nodes and cells. The search for the contact region results in a list of con-

tact pairs, which introduce the contact or buffer elements. Then the calculation of the contact velocities and forces can be conducted by using Lagrange multipliers or penalty functions to introduce the non-penetration condition into the variational equation. However, for meshless methods, the boundaries are represented only by nodes, boundary edges or surfaces do not exist any longer. Therefore it's much more challenging to avoid the penetration of different media. In this section, we propose a novel and effective contact algorithm, which introduces no extra computational costs more than the computations for a single body.

In the *Optimal Transportation Method*, all the bodies are discretized by material points which carry the lumped mass of the media. The position and neighbors of the material points are updated every time steps. We consider each material point as the center of a d-dimensional sphere in $\mathbb{R}^d$ with the preset search range as the radius. Suppose the entire node set of the problem domain is the candidate support of each material point, consequently nodes from different media become acceptable for the neighbor of the material points. Before demonstrating the meshless contact detection, we introduced two definitions of the neighbor of particles. Suppose we have multibodies Ω_α, $\alpha \in \mathcal{A} \equiv \{A, B, ...\}$ is the body set, define the node set of Ω_α as $S_\alpha = \{\mathbf{x}_a \in \Omega_\alpha\}$ and the material point set as $\mathcal{M}_\alpha = \{\boldsymbol{\theta}_q \in \Omega_\alpha\}$, then we have the total node set $S = \cup_{\alpha\in\mathcal{A}} S_\alpha$ and the total material point set $\mathcal{M} = \cup_{\alpha\in\mathcal{A}} \mathcal{M}_\alpha$. The first neighbor of $\forall \mathbf{X} \in \{S \cup \mathcal{M}\}$ can be defined as

$$\mathcal{N}(\mathbf{X}) = \{\mathbf{x}_a \in S \mid |\mathbf{x}_a - \mathbf{X}| \leq R\}, \tag{5.1}$$

where $R \in \mathbb{R}$ is the search range,which specifies how close is the node $\mathbf{x}_a$ that will contribute to $\mathbf{X}$. Note $\mathbf{x}_a \in \mathcal{N}(\mathbf{x}_a)$.

For contact detection, if the nodes from Ω_A come into the search range or first neighbor of the material point in $\mathcal{M}_B$ where $B \cap A = \emptyset$, it means the contact between A and B is going to happen. However it is possible to set a large individual search range for each material point, even body A and B are far away, the nodes from Ω_A still can enter the support domain of material points in $\mathcal{M}_B$. Thus in order to eliminate this artifact, we need more information to determine whether the bodies are physically close to each other. Then we define the second neighbor for each material point $\forall \boldsymbol{\theta}_q \in M_\alpha$ as

$$\mathcal{N}^*(\boldsymbol{\theta}_q) = \{\mathbf{x}_a \in S \mid \mathbf{x}_a \in \bigcup_{\mathbf{x}_b \in \{S_\alpha \cap \mathcal{N}(\boldsymbol{\theta}_q)\}} \mathcal{N}(\mathbf{x}_b)\}. \tag{5.2}$$

Note that the search range for any material points and nodes can be different, actually the smaller search range for the first neighbor of nodes gives the more accurate contact detection,Fig. 5.7. We say the node belongs to the support of a material point if and only if it belongs to its second neighbor. Instead of checking the distance between contact-cell pairs and applying an artificial force to the contacting elements for impenetrability, the constitutive law of the contacting bodies will automatically avoid the penetration, since nodes in Ω_A getting into second neighbor of material points in $\mathcal{M}_B$ now become part of Ω_B, but with relative movements between Ω_A and Ω_B. On the other hand, new neighbor nodes are inserted into the support of the material point, deformations may have been introduced into the material point,

which lead to stresses, strains and forces recalculated by the constitutive law of the body. The meshless contact algorithm greatly reduces the time required in the search

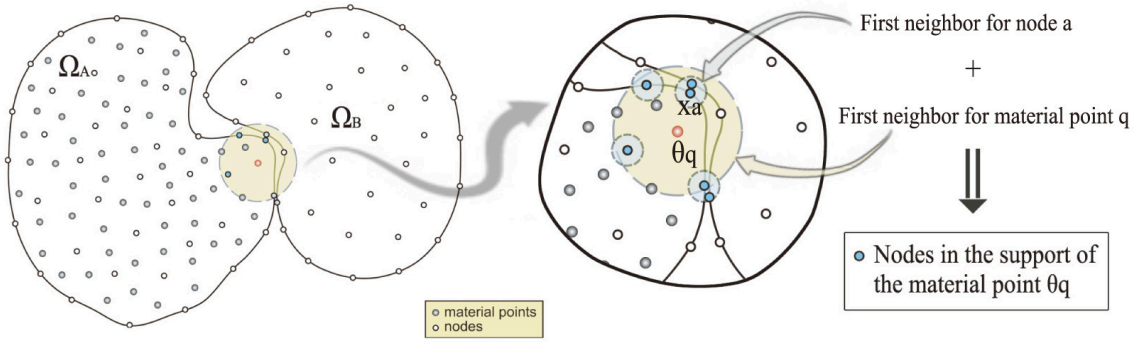

Figure 5.7: Meshless dynamic contact detection algorithm.

for penetration over conventional search algorithms, since a range searching involving only points in $\mathbb{R}^d$ is required. There are many fast search algorithms and efficient data structures for the aid of range query [10], for instance Kd trees, octrees and cell array algorithms. Because the size and shape of the queries are roughly constant and known in advance in our simulations, we use the cell array algorithm, which provide almost constant time search speed and $o(N)$ for construction, where N is the number of nodes. As the boundaries are represented only by nodes, if contact interface is known, the new meshless contact algorithm works very well with refined nodal space and appropriate search range in the vicinity of contact. Otherwise the entire boundary has to be well defined to avoid penetrations.

To test the efficiency and accuracy of our new meshless impact algorithm, we present an example of a complex dynamic contact system, where six two-dimensional sugar cubes contact with each other at different moment and different angles or non-smooth contacts. Since we do not introduce any constraints or gap functions (the

contact will automatically happen based on the geometric conditions), the constitutive law will generate force based on the relative movements of nodes in the support of each material point, we are able to capture not only the normal forces but also the friction on the contact interfaces. Each cube with density $\rho = 7833\ kg/m^3$ has the dimension as $1m \times 1m$ and discretized by 145 nodes, see Fig. 5.8. The initial velocities are $v_1 = 2$ m/s, $v_2 = -2$ m/s and $v_4 = 4$ m/s, the rests are static. Neo-Hookean constitutive relation with the *lamé* constants $\lambda = 115.38$ Gpa and $\mu = 76.92$ Gpa is applied for each of the bodies.

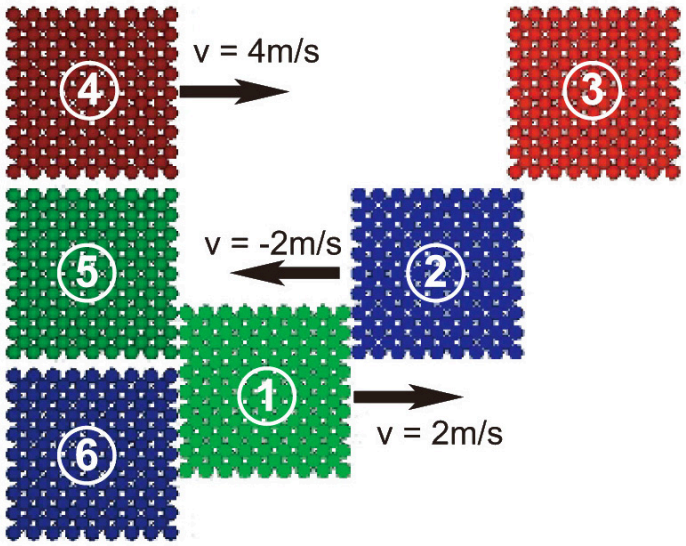

Figure 5.8: Six cubes impact example.

Explicit Newmark time integration is used. Again a fraction of the Courant limit is used to determine the stable time step. Here the problem is solved with a time step $\Delta t = 5\mu s$, the response is computed up to 2.5 s. The motion at $t = 35$ms, 0.125s, 0.4s and 0.95s are shown in Fig. 5.12. The history of the energy, momentum of every

cube in x direction and momentum of each cube in y direction are given in Fig. 5.9, Fig. 5.10 and Fig. 5.11 respectively. It is evidenced that all the fields are perfectly conserved during the impact by using the novel meshless contact algorithm.

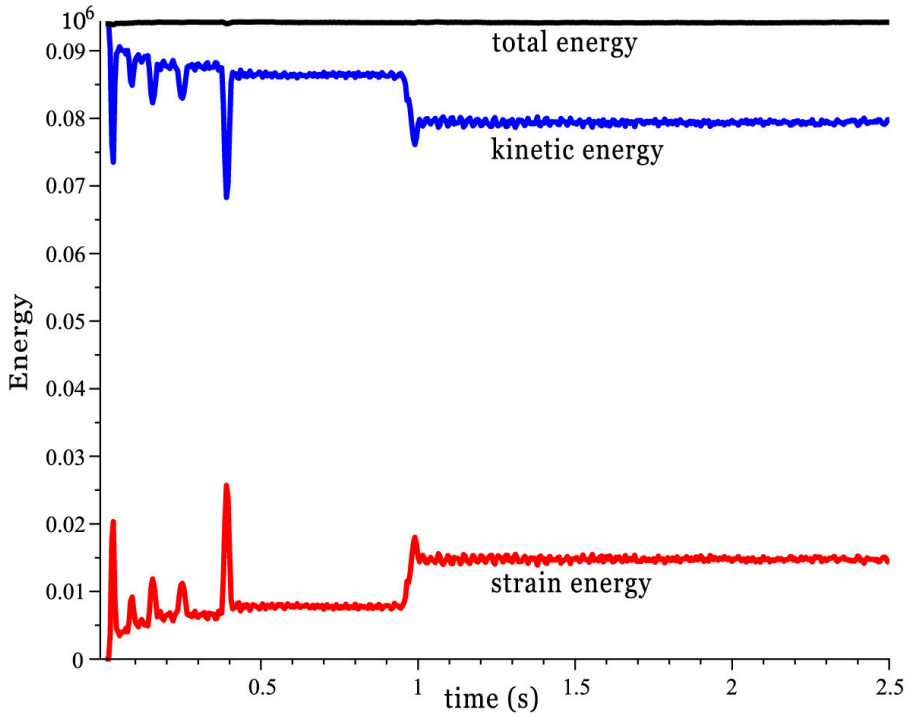

Figure 5.9: Energy conservation for six cubes impact.

5.2.2 Constitutive model

The boundary layer that develops between bodies in contact may be expected to undergo very large plastic deformations. In addition, the particles themselves may undergo large plastic deformations as sufficiently high impact velocities. In order to account for these effects, we adopt a standard formulation of finite-deformation plasticity based on a multiplicative decomposition of the deformation gradient into

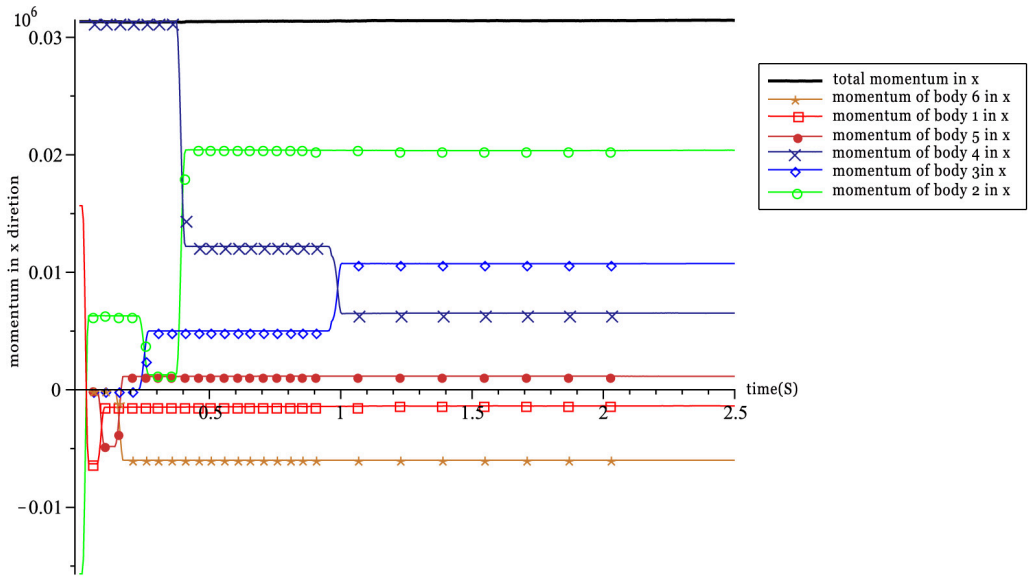

Figure 5.10: Momentum conservation in x direction for six cubes impact.

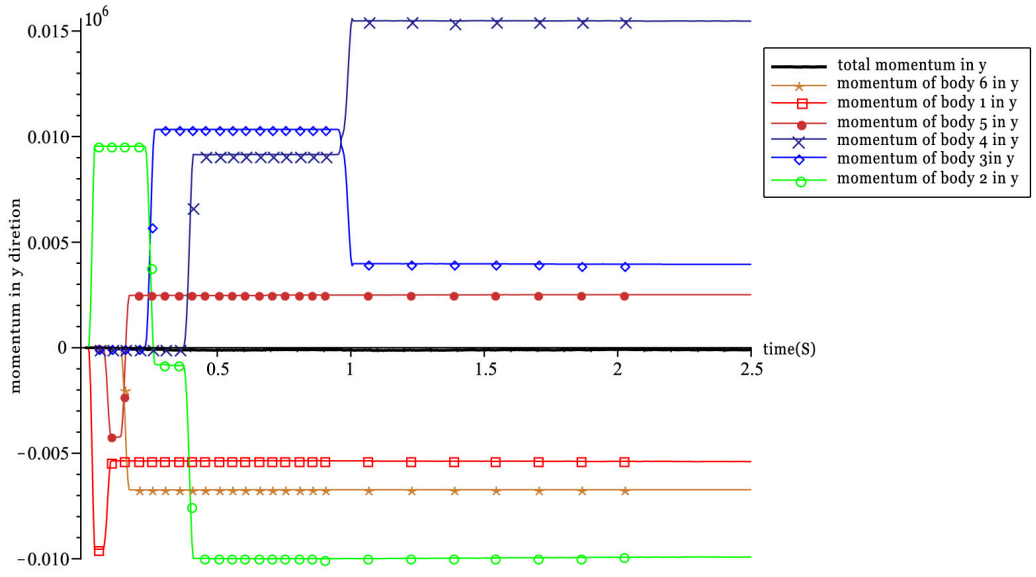

Figure 5.11: Momentum conservation in y direction for six cubes impact.

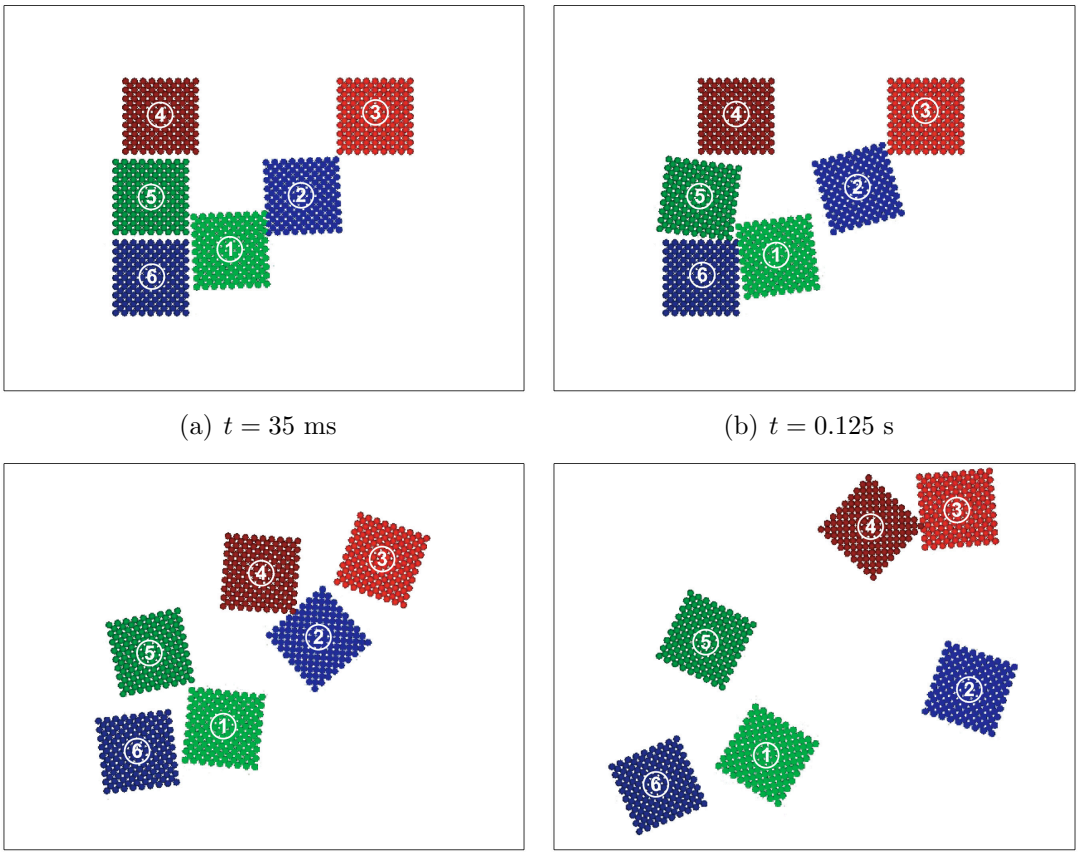

(a) $t = 35$ ms

(b) $t = 0.125$ s

(c) $t = 0.4$ s

(d) $t = 0.95$ s

Figure 5.12: Motion of the six cubes impact.

elastic and plastic components [12, 38, 11] (see Fig. 5.13),i.e.,

$$\mathbf{F} = \mathbf{F}^e\mathbf{F}^p\,. \tag{5.3}$$

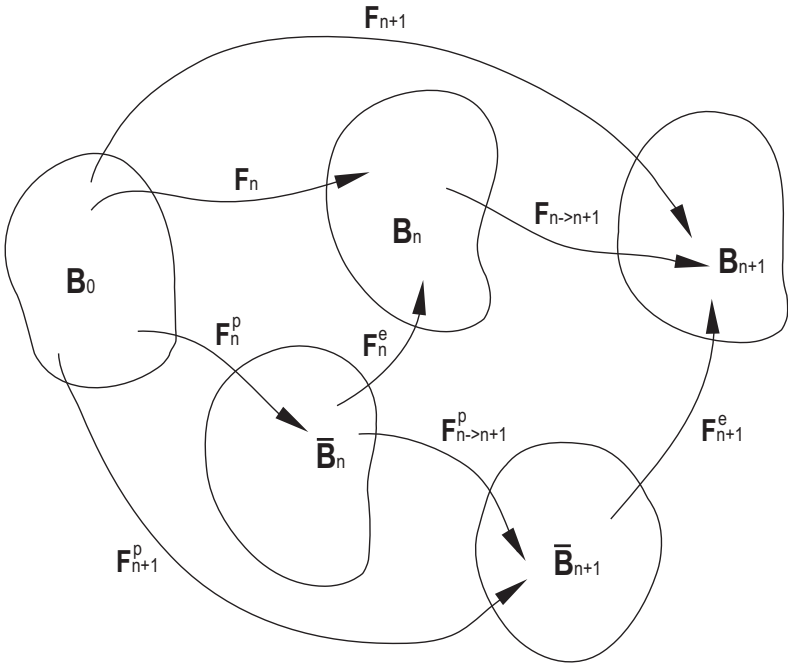

Figure 5.13: Decomposition of the deformation gradient into elastic and plastic components.

We further assume that J_2-plasticity prevails. In a typical ballistic impact event, very high strain rates may be attained at which the flow stress may exhibit a strong rate-sensitivity. In our calculations we employ the conventional power law in conjunction with Johnson and Cook's [23] power thermal softening law,

$$\dot{\epsilon}^p = \begin{cases} \dot{\epsilon}^p_0 \left[\left(\frac{\bar{\sigma}}{g(\epsilon^p)} \right)^m - 1 \right], \text{ if } \bar{\sigma} > g(\epsilon^p)\,, \\ 0\,, \text{ otherwise} \end{cases} \tag{5.4a}$$

$$g(\epsilon^p) = \sigma_y \left[1 - \left(\frac{T - T_0}{T_m - T_0} \right)^\alpha \right] \left(1 + \frac{\epsilon^p}{\epsilon^p_0} \right)^{1/n}\,. \tag{5.4b}$$

Here, $\bar{\sigma}$ is the effective Mises stress; ϵ^p the effective plastic strain; $\dot{\epsilon}^p$ the effective plastic strain rate; ϵ_0^p a reference plastic strain; $\dot{\epsilon}_0^p$ a reference plastic strain rate; m the rate sensitivity exponent; n the hardening exponent; g the flow stress; σ_y the initial yield stress; T_0 a reference temperature; T_m the melting temperature and α the thermal softening exponent.

Thus the incremental energy density introduced in (§3.103) reduces to

$$W_k(\mathbf{F}_{k+1}) = \min_{\Delta\epsilon^p} \left\{ A(\mathbf{F}_{k+1}\mathbf{F}_{k+1}^{p-1}, \epsilon_{k+1}^p) - A(\mathbf{F}_k\mathbf{F}_k^{p-1}, \epsilon_k^p) + \Delta t \Psi^* \left(\frac{\Delta\epsilon^p}{\Delta t} \right) \right\} , \tag{5.5}$$

where the free energy has the form,

$$A(\mathbf{F}\mathbf{F}^{p-1}, \epsilon^p) = W^e(\mathbf{F}\mathbf{F}^{p-1}) + W^p(\Delta\epsilon^p) , \tag{5.6}$$

and assuming the elastic energy density W^e of the form

$$W^e = f(J^e) + \mu ||\boldsymbol{\epsilon}^{e,\mathrm{dev}}||^2 , \tag{5.7}$$

with J^e as the Jacobian of the elastic deformation gradient $\mathbf{F}^e$ and

$$\boldsymbol{\epsilon}^e = \frac{1}{2} \log(\mathbf{C}^e) , \tag{5.8}$$

playing the role of an equivalent elastic strain tensor, where $\mathbf{C}^e$ is the corresponding elastic right Cauchy-Green deformation tensor $\mathbf{C}^e = \mathbf{F}^{eT}\mathbf{F}^e$.

The temperature increase experienced by the particles and the target plate may

be considerable due to the plastic working of the solid in the course of an impact event. Under these conditions, the rate of heat supply due to the plastic work is estimated as

$$s = \beta \dot{W}^p \,, \tag{5.9}$$

where $\dot{W}^p$ is the plastic power per unit deformed volume and β is the Taylor-Quinney coefficient [52].

5.2.3 Numerical results

We begin by analyzing a relationship between the Depth of Penetration (DOP) and the impact velocity consisting of an elastoplastic aluminum plate struck by an elastic-plastic steel sphere with high/hyper velocity. A full three-dimensional simulation of this setup is the most challenging problem for numerical methods, and has not been able to fulfill by the conventional Finite Element Method with adaptive meshing and commonly used meshless methods. The plate under consideration is 10mm in radius and 10mm thick, the projectile is a sphere with 1.7mm in diameter and travels at velocities in the range 0.5 to 3.0km/s at the normal impact direction.

The target and penetrator geometry used in the simulations is presented in Fig. 5.14. The constitutive model for the plate and projectile is explained in preceding section, and the material parameters can be found in Table 5.2 and 5.3. The discretization of the plate and sphere contains in total 29,064 material points and 5,500 nodes. A series of 8 full three-dimensional simulations with impact velocity from 0.5 to 3.0km/s fulfilled by the *OTM* and our new meshless contact algorithm were used to study the

penetration versus impact velocity curve for a highly deformable spherical projectile striking an elastoplastic plate.

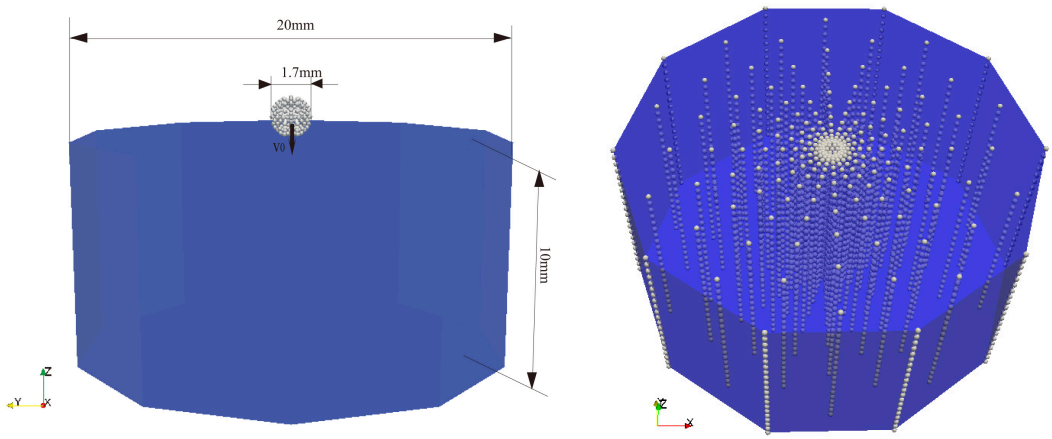

(a) Geometry of the model and discretization of the projectile

(b) Discretization of the plate

Figure 5.14: Meshless model used in the analysis of impact of a deformable steel sphere into an elastoplastic aluminum plate.

Table 5.2: Mechanical material constants used in the analysis of impact of a deformable steel sphere into an elastoplastic aluminum plate

Material	$\rho(\text{kg}/m^3)$	E(Gpa)	ν	σ_y(Gpa)	ϵ_0^p	n
High-strength steel	7850	200	0.29	1.50	0.001	22
6061-T6 Al	2700	69	0.33	0.276	0.001	13.5

Table 5.3: Thermal constants used in the analysis of impact of a deformable steel sphere into an elastoplastic aluminum plate

Material	c(J/kg/K)	k(W/m/K)	T_0(K)	T_m(K)	α	β
High-strength steel	477	38	300	1777	1.17	0.9
6061-T6 Al	896	167	300	853	0.5	0.9

Details of the penetration behavior are illustrated in Fig. 5.15-5.21. In Fig. 5.15-5.18 the deformed configurations are shown at the moment when nearly all of the

initial kinetic energy dissipated as plastic work. When the impact velocity increases, highly non-linear large deformation happens in the steel sphere at early ages. Consequently as expected, the crater shape becomes sharper and out-of-surface deformation on the plate surface becomes larger. Fig. 5.19-5.21 shows the history of the impact for very high velocity impact. It is evidenced that the plastic wave reaches the bottom of the plate as the velocity is higher than $1500m/s$. The plot of the normalized depth of penetration versus impact velocity and The time of penetration versus impact velocity are shown in Fig. 5.22 and Fig. 5.23, respectively. Such 3D impact simulations involving highly deformable projectile with thermal effects have not been done by other methods, especially Finite Element Method, so we do not have any comparison from other numerical experiments. However from the Anderson-Walker model [54] and Rubin's general formulation [44] for deformable projectile, the shape of the curve from *OTM* compares very well with their results. Furthermore, when we increase the impact velocity, it may be observed the penetration depth asymptotically approaches that predicted by the hydrodynamic theory. Again the *OTM* shows great capability for simulations involving extremely large deformation, fast, transient loading and hydrodynamic phenomena.

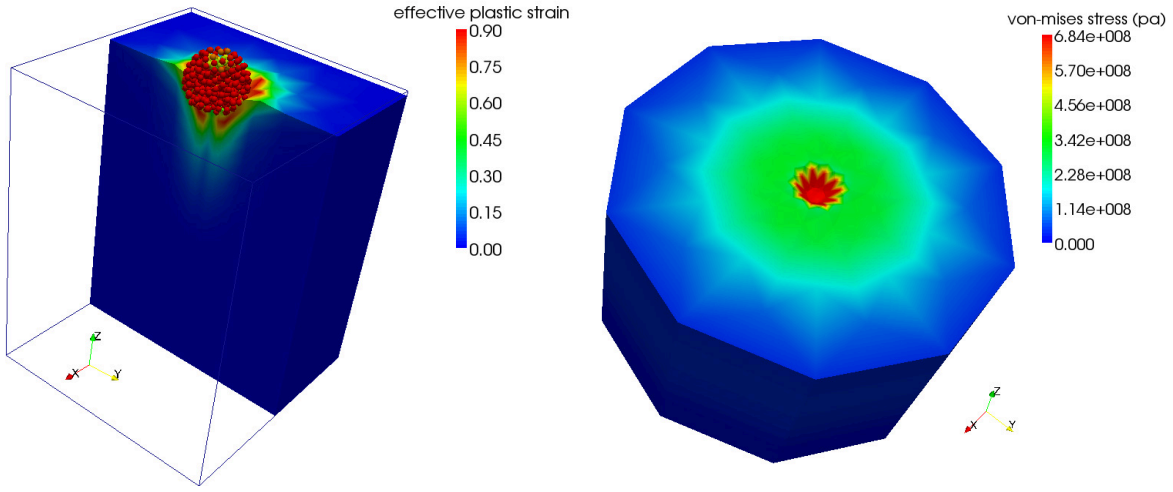

(a) Close-up of the deformed configuration with distribution of the effective plastic strain

(b) Crater shape on the plate and distribution of von-Mises stress at $t = 2.92\ \mu s$

Figure 5.15: Deformed configuration at the momentum when nearly all the initial kinetic energy dissipated as plastic work in the impact of a deformable steel sphere onto an elastoplastic aluminum plate with velocity 500 m/s at normal direction.

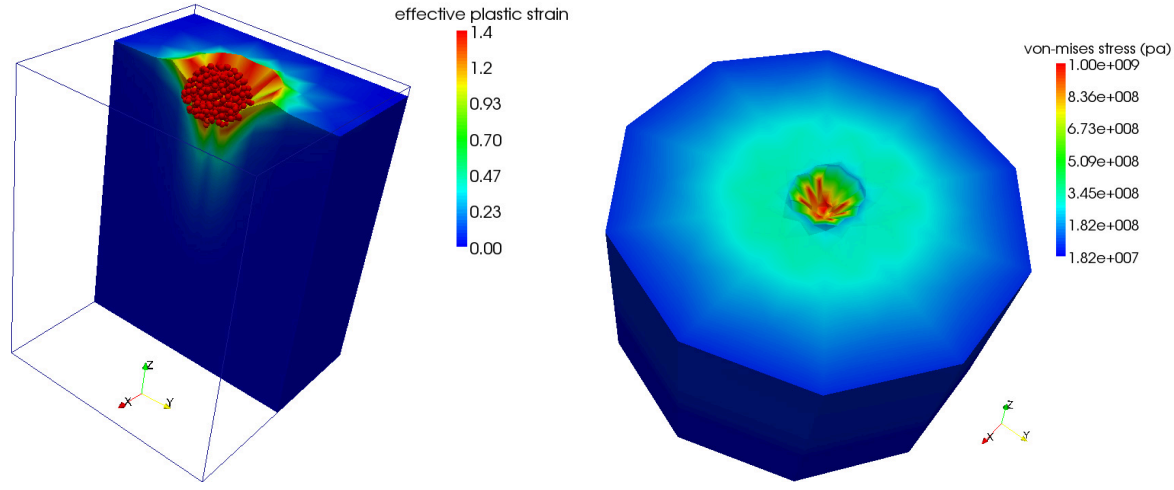

(a) Close-up of the deformed configuration with distribution of the effective plastic strain

(b) Crater shape on the plate and distribution of von-Mises stress at $t = 3.2\ \mu s$

Figure 5.16: Deformed configuration at the momentum when nearly all the initial kinetic energy dissipated as plastic work in the impact of a deformable steel sphere onto an elastoplastic aluminum plate with velocity 750 m/s at normal direction.

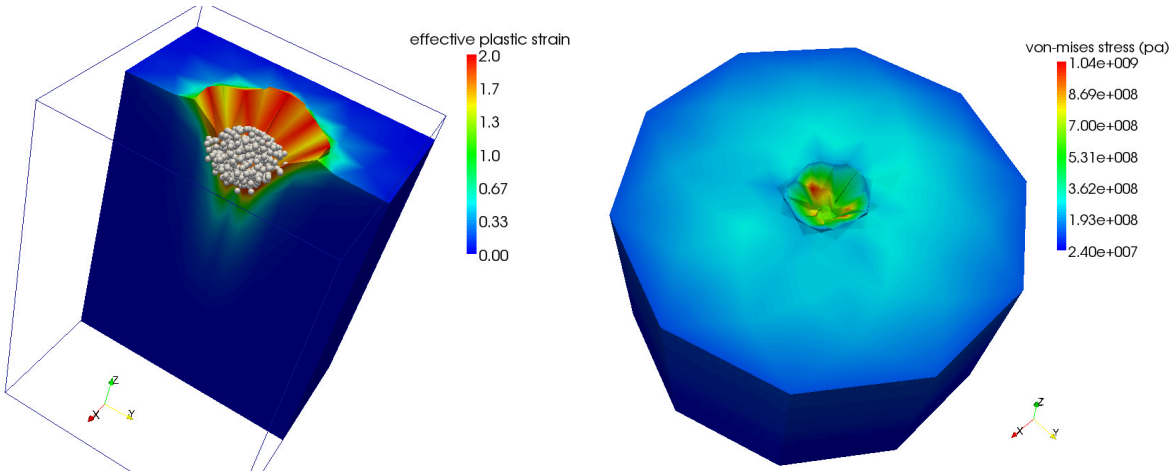

(a) Close-up of the deformed configuration with distribution of the effective plastic strain

(b) Crater shape on the plate and distribution of von-Mises stress at $t = 3.54\ \mu s$

Figure 5.17: Deformed configuration at the momentum when nearly all the initial kinetic energy dissipated as plastic work in the impact of a deformable steel sphere onto an elastoplastic aluminum plate with velocity 1000 m/s at normal direction.

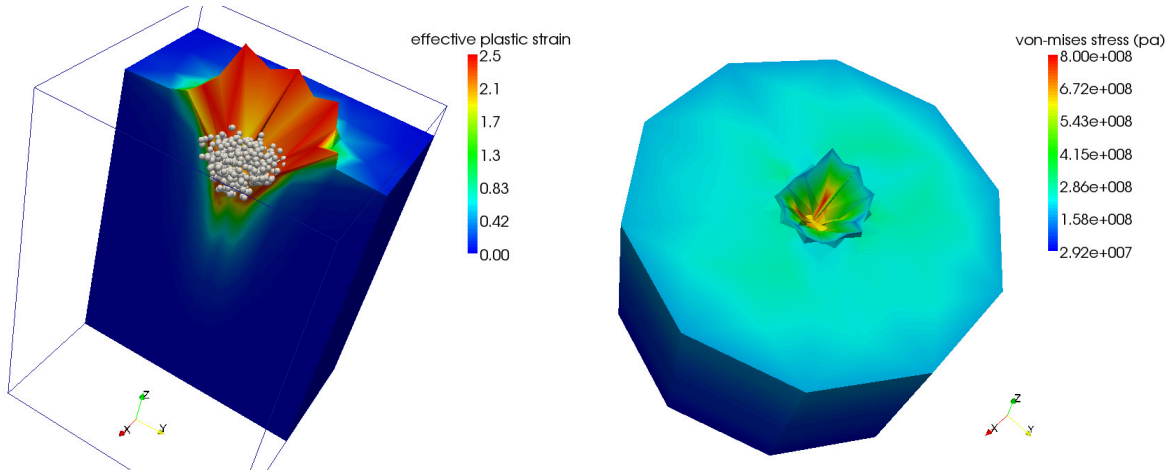

(a) Close-up of the deformed configuration with distribution of the effective plastic strain

(b) Crater shape on the plate and distribution of von-Mises stress at $t = 3.84\ \mu s$

Figure 5.18: Deformed configuration at the momentum when nearly all the initial kinetic energy dissipated as plastic work in the impact of a deformable steel sphere onto an elastoplastic aluminum plate with velocity 1250 m/s at normal direction.

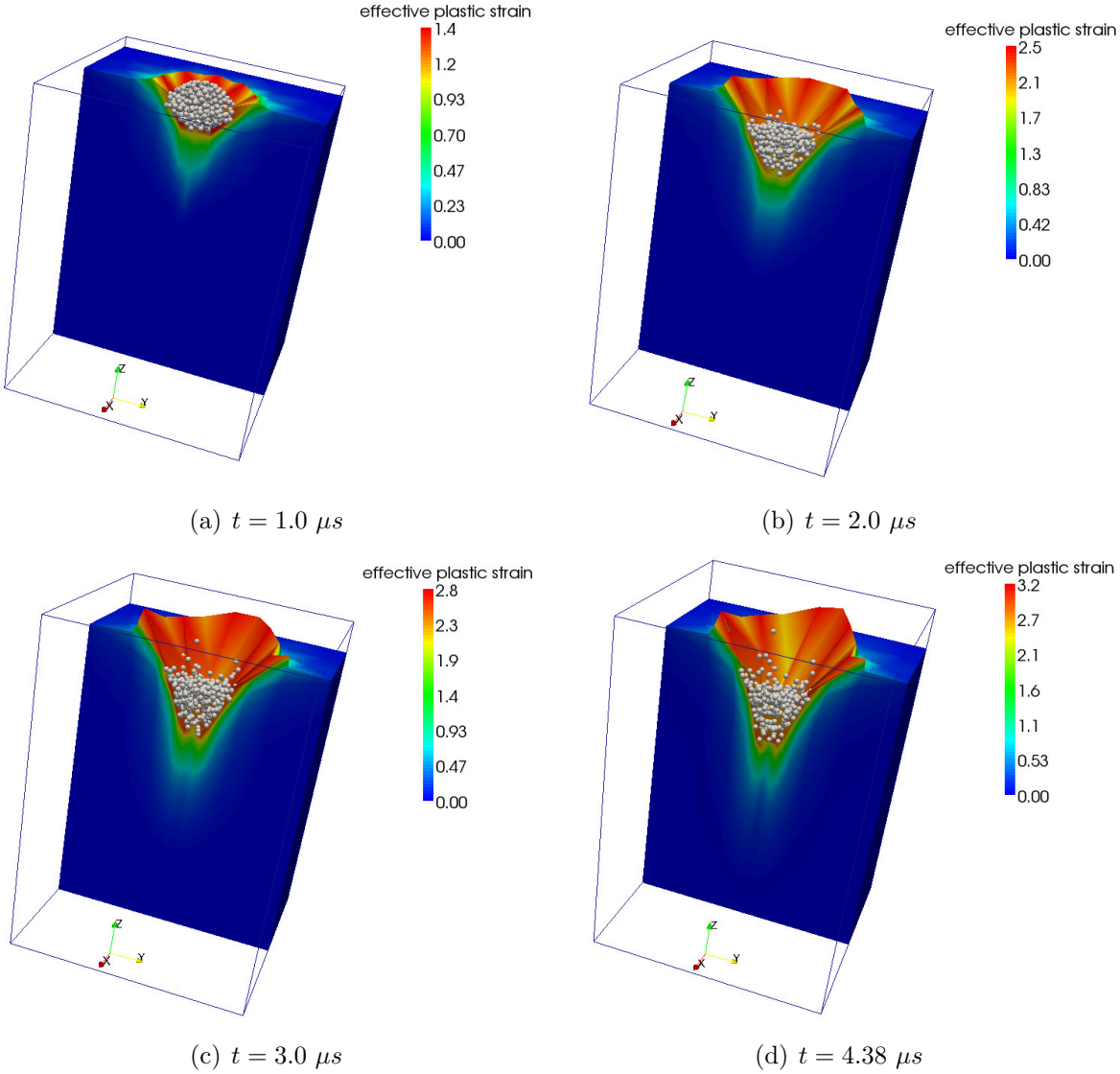

(a) $t = 1.0\ \mu s$ (b) $t = 2.0\ \mu s$

(c) $t = 3.0\ \mu s$ (d) $t = 4.38\ \mu s$

Figure 5.19: Evolution of the deformed configuration with distribution of the effective plastic strain at different moment in the impact of a deformable steel sphere onto an elastoplastic aluminum plate with velocity 1500 m/s at normal direction.

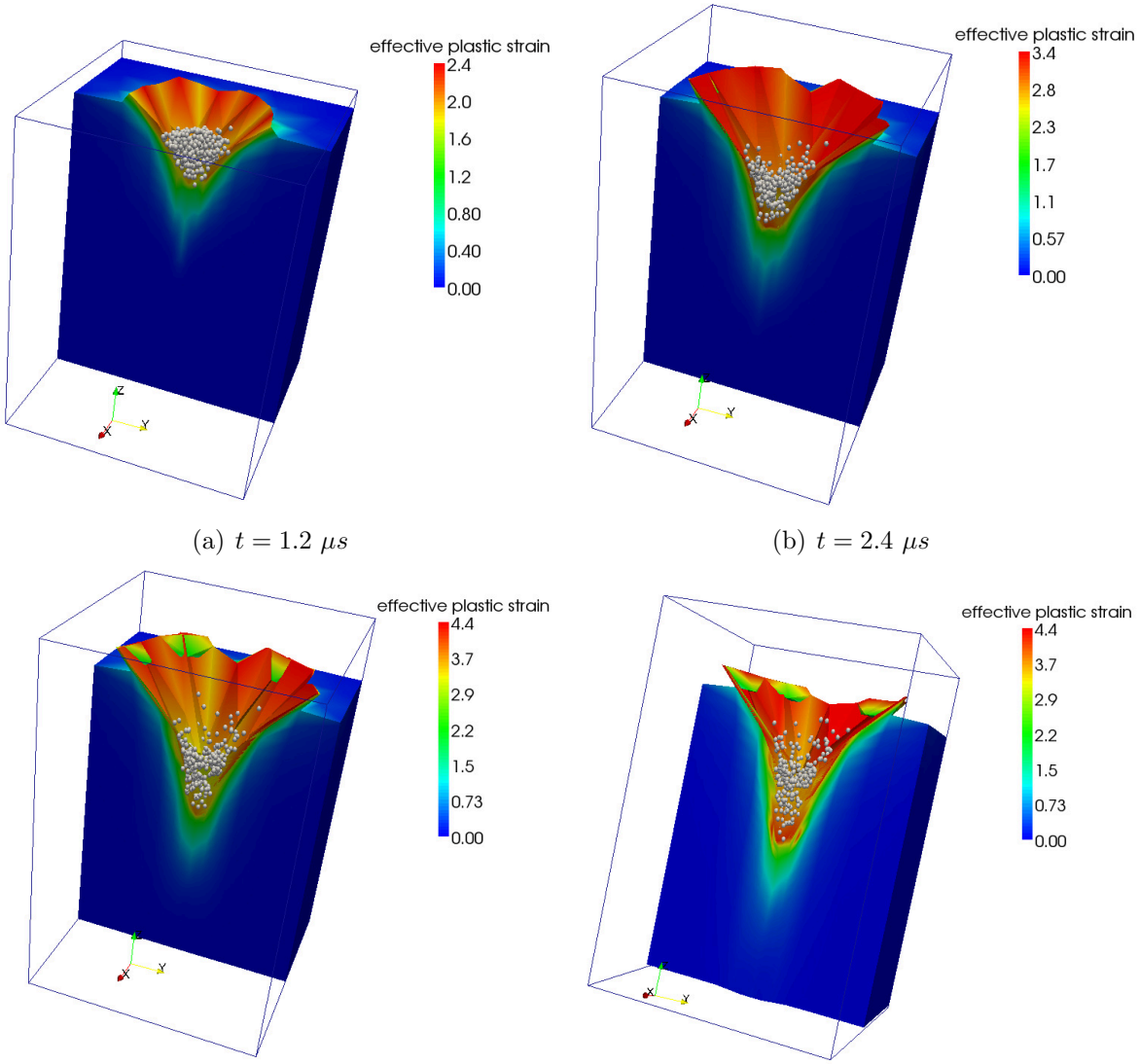

(a) $t = 1.2\ \mu s$ (b) $t = 2.4\ \mu s$

(c) $t = 3.6\ \mu s$ (d) $t = 5.1\ \mu s$

Figure 5.20: Evolution of the deformed configuration with distribution of the effective plastic strain at different moment in the impact of a deformable steel sphere onto an elastoplastic aluminum plate with velocity 2000 m/s at normal direction.

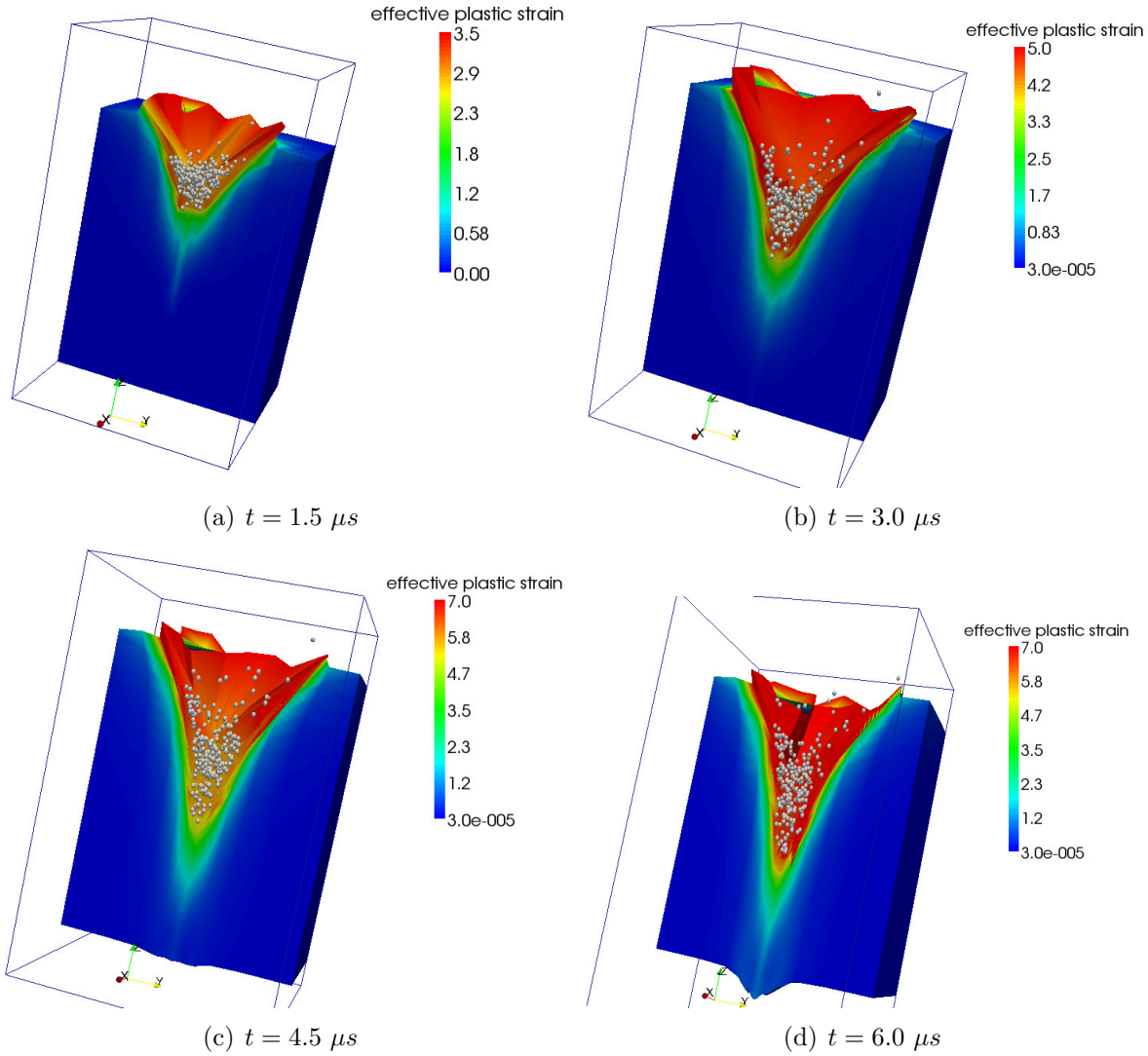

(a) $t = 1.5\ \mu s$ (b) $t = 3.0\ \mu s$

(c) $t = 4.5\ \mu s$ (d) $t = 6.0\ \mu s$

Figure 5.21: Evolution of the deformed configuration with distribution of the effective plastic strain at different moment in the impact of a deformable steel sphere onto an elastoplastic aluminum plate with velocity 2500 m/s at normal direction.

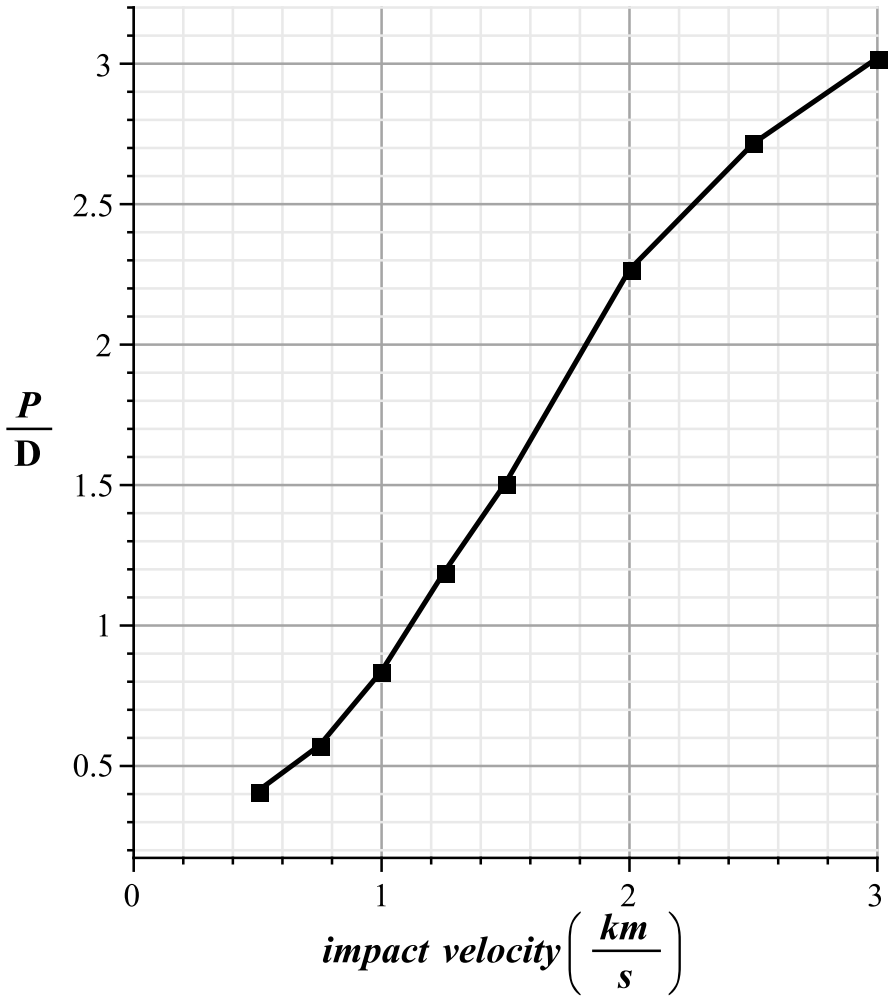

Figure 5.22: Normalized depth of penetration versus impact velocity for a deformable high-strength steel sphere onto an elastic-plastic aluminum plate.

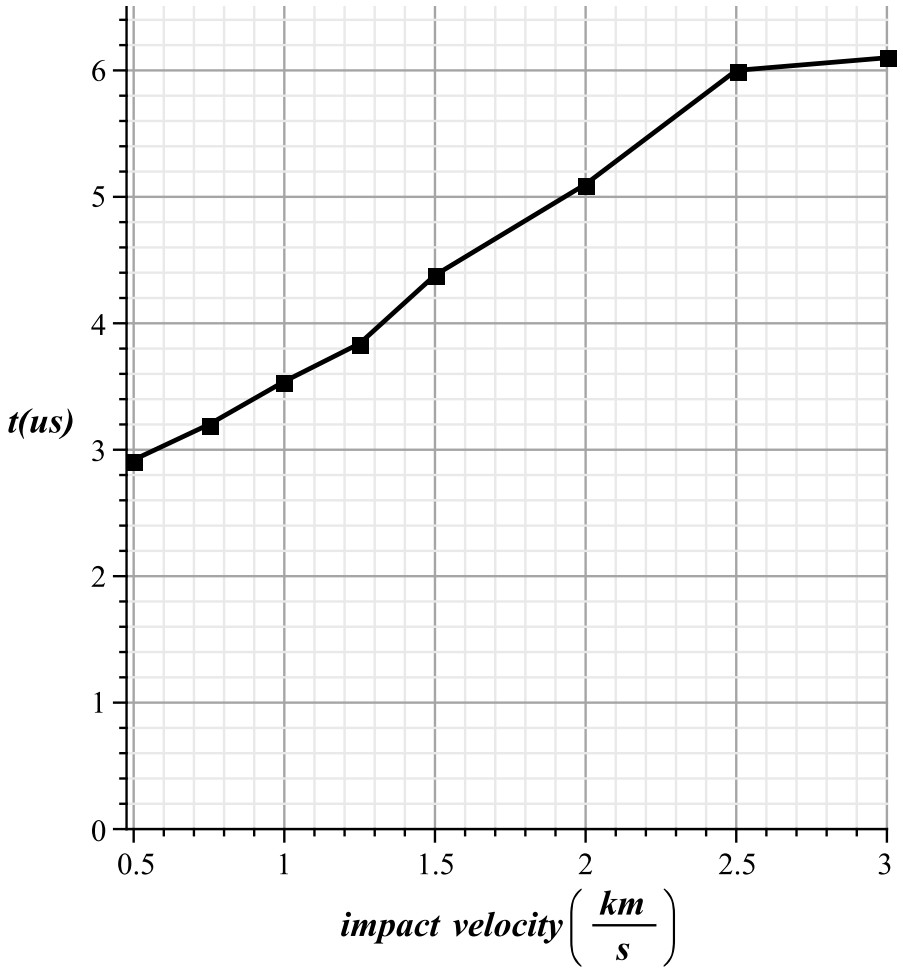

Figure 5.23: Time elapsed before the total dissipation of initial kinetic energy for a deformable high-strength steel sphere onto an elastic-plastic aluminum plate.

Chapter 6

Conclusions and Future Work

In this work a Lagrangian scheme called the *Optimal Transportation Method* (OTM) for the simulation of general solid flows is developed through an integration of optimal transportation theory with meshless interpolation and material point integrations.

Our work is mainly focused on simulations of general solid flows involving extremely large deformation, fast, transient loading and hydrodynamic phenomena. For this purpose, the meshless methods are an excellent alternative to the conventional grid-based methods. The *OTM* is a Lagrangian particle method, which reserves all the advantages of absence of a mesh. Furthermore, by employing the *local max-ent approximation scheme*, it overcomes the difficulty for imposition of essential boundary conditions in most of the meshless methods.

The theoretical framework developed for the *OTM* in this thesis generalized the Benamou-Brenier differential formulation of optimal transportation problems and leads to a multifield variational characterization of solid flows, including inelasticity, equation of state, and general geometries in $\mathbb{R}^d$ and boundary conditions. An extended action from the bare action in Optimal Transportation theory is proposed for elastic and inelastic solid flows, such that the Euler's equation of motion of gen-

eral solid flows can be recast in the formalism of gradient flows with respect to the optimal transportation differential structure. Further the Euler-Lagrange equations associated with the action are verified to be identical to the Euler's equations of motion and continuity equations. The governing variational principle of the framework lends itself ideally to discretization by a combination of conforming interpolation of the velocity field and pointwise sampling of the local material state. Hence a time discrete, iterative variational scheme whose solutions converge to the solution of the Euler's equation of motion is constructed by following the strategy used in the optimal transportation structure. The spatial discretization of the semi-discrete action is carried over by the insertion of material points into the semi-discrete Euler-Lagrange equation. Then a fully discrete action for computations is obtained and a finite-dimensional semi-discrete central difference scheme is defined such that the motion of the solid flows can be solved forward explicitly.

To this end, we have demonstrated the accuracy, convergence, stability, versatility and great capability of the *Optimal Transportation Method* with the aid of demanding convergence tests, a series of fully 3D meshless simulations of different applications. Particularly in order to efficiently simulate the high/hyper-velocity impact problems, we proposed a new meshless contact algorithm, which conserves the energy and momentum of the dynamic system exactly. On the other hand, since only a range query for points is required in the course of the computation, lots of efficient algorithms and data structures are available for different purpose. In our simulation, we use the cell-array algorithm, which provides almost constant search speed and $o(N)$ construction

time. From the 3D calculations, it is evidenced that *OTM* has a great potential for solving lots of practical engineering problems difficult for other numerical methods.

Many possible directions might be taken in the future to further the scope of application of this methodology. Immediate steps would be the extension of the method to h-adaptivity. For simulations involving hydrodynamic phenomena, fracture/fragmentation usually appears in the course of impact, thus principles in fracture mechanics should be counted for the reset of the support of each material points. This could be done by setting up the invisibility of nodes to the material points by some physical criteria. The application to fully coupled thermomechanical problems should be another potential direction. From the numerical analysis point of view, parallel implementations might be devised.

Bibliography

[1] L. Ambrosio. Lecture notes on optimal transport problems. In *Mathematical Aspects of Evolving Interfaces,Lecture Notes in Math.*, volume 1812, pages 1–52. Springer-Verlag, Berlin/New York, 2003.

[2] M. Arroyo and M. Ortiz. Local maximum-entropy approximation schemes: A seamless bridge between finite elements and meshfree methods. *Int. J. Numer. Meth. Eng.*, 65:2167–2202, 2006.

[3] I. Babuška and J. Melenk. The partition of the unity finite element method. Technical Report BN-1185, Institute for Physical Science and Technology, 1995.

[4] S. Beissel and T. Belytschko. Nodal integration of the element-free galerkin method. *Comput. Meth. Appl. Mech. Eng.*, 139:49–74, 1996.

[5] T. Belytschko, Y. Guo, W. K. Liu, and S. P. Xiao. A unified stability analysis of meshless particle methods. *Int. J. Numer. Meth. Eng.*, 48:1359–1400, 2000.

[6] T. Belytschko, Y. Krongauz, J. Dolbow, and C. Gerlach. On the completeness of meshfree particle methods. *Int. J. Numer. Meth. Eng.*, 43:785–819, 1998.

[7] T. Belytschko, Y. Krongauz, D. Organ, M. Fleming, and P. Krysl. Meshless methods: An overview and recent development. *Comput. Meth. Appl. Mech. Eng.*, 139:3–47, 1996.

[8] T. Belytschko, Y. Y. Lu, and L. Gu. Element-Free Galerkin Methods. *Int. J. Numer. Meth. Eng.*, 37:229–256, 1994.

[9] J. D. Benamou and Y. Brenier. A numerical method for the oprimal time-continuous mass transport and related problems. in: Monge-Ampere equation: applications to geometry and optimization. *Contemp. Math.*, 226:1–11, 1999.

[10] J. L. Bentley and J. H. Friedman. Data structures for range searching. *Comput. Surv.*, 11:397–409, 1979.

[11] G. T. Camacho and M. Ortiz. Adaptive lagrangian modelling of ballistic penetration of metallic targets. *Computer Methods in Applied Mechanics and Engineering*, 142:269–301, 1997.

[12] A. Cuitino and M. Ortiz. A material-independent method for extending stress update algorithms from small-strain plasticity to finite plasticity with multiplicative kinematics. *Eng. Comput.*, 9:437–451, 1992.

[13] J. Dolbow and T. Belytschko. Numerical integration of the galerkin weak form in meshfree methods. *Comput. Mech.*, 23:219–230, 1999.

[14] C. A. Duarte and J. T. Oden. h-p clouds–An h-p meshless method. *Numer. Meth. Part. Differ. Equat.*, 12:673–705, 1996.

[15] C. T. Dyka and R. P. Ingel. An approach for tension instability in smoothed particle hydrodynamics (SPH). *Comput. Struc.*, 57:573–580, 1995.

[16] C. T. Dyka, P. W. Randles, and R. P. Ingel. Stress points for tension instability in SPH. *Int. J. Numer. Meth. Eng.*, 40:2325–2341, 1997.

[17] L. C. Evans. *Partial diffrential equations and Monge-Kantorovich mass transfer.* Department of Mathematics, University of California, Berkeley (course notes available online), September 2001.

[18] R. A. Gingold and J. J. Monaghan. Smoothed particle hydrodynamics: Theory and application to non-spherical stars. *Mon. Not. R. Astron. Soc.*, 181:375–389, 1977.

[19] W. Herrmann, L. D. Bertholf, and S. L. Thompson. Computational methods for stress wave propagation in nonlinear solid mechanics. Technical Report SAND-74-5397, Sandia National Laboratories, 1974.

[20] A. Huerta, T. Belytscko, S. Fernandez-Mendez, and T. Rabczuk. Meshfree methods. *Encyclopedia of Computational Mechanics*, 10:279–309, 2004.

[21] E. T. Jaynes. Information theory and statistical mechanics. *Phys. Rev.*, 106(4):620–630, 1957.

[22] G. R. Johnson and S. R. Beissel. Normalized smoothing functions for SPH impact computations. *Int. J. Numer. Meth. Eng.*, 39:2725–2741, 1996.

[23] G. R. Johnson and W. H. Cook. Fracture characteristics of three metals subjected to various strains, strain rates, temperatures and pressures. *Eng. Fract. Meek*, 21(1):31–48, 1985.

[24] R. Jordan, D. Kinderlehrer, and F. Otto. The variational formulation of the Fokker-Planck equation. *SIAM J. Math. Anal.*, 29:1–17, 1998.

[25] A. Kamoulakos. A simple benchmark for impact. *Benchmark*, pages 31–35, 1990.

[26] S. Kullback. *Information Theory and Statistics*. Wiley, New York, NY, 1959.

[27] P. Lancaster and K. Salkauskas. Surface generated by moving least square methods. *Math. Comput.*, 37:141–158, 1980.

[28] A. Lew, J. E. Marsden, M. Ortiz, and M. West. Variational time integrators. *Int. J. Numer. Meth. Eng.*, 60:153–212, 2004.

[29] S. Li and W. K. Liu. Meshfree nad particle methods and their applications. *Appl. Mech. Rev.*, 55(4), 2002.

[30] T. Liszka and J. Orkisz. The finite difference method at arbitrary irregular grids and its application in applied mechanics. *Comput. Struct.*, 11:83–95, 1980.

[31] W. K. Liu, Y. Chen, R. A. Uras, and C. T. Chang. Generalized multiple scale reproducing kernel particle method. *Comput. Meth. Appl. Mech. Eng.*, 139:91–157, 1996.

[32] W. K. Liu, S. Jun, and Y. F. Zhang. Reproducing kernel particle methods. *Int. J. Numer. Meth. Eng.*, 20:1081–1106, 1995.

[33] L. B. Lucy. A numerical approach to the testing of the fission hypothesis. *Astrophys J.*, 82:1013, 1977.

[34] J. E. Marsden and M. West. *Discrete mechanics and variational integrators*, volume 10. Cambridge University Press, Cambridge, MA, 2001.

[35] J. J. Monaghan. Why particle methods work. *SIAM J. Sci. Stat. Comput.*, 3:422, 1982.

[36] J. J. Monaghan. Smoothed particle hydrodynamics. *Annu. Rev. Astron. Astrophys.*, 30:543–574, 1992.

[37] B. Nayroles, G. Touzot, and P. Villon. Generalizing the finite element method: Diffuse approximation and diffuse elements. *Comput. Mech.*, 10:307–318, 1992.

[38] M. Ortiz and L. Stainier. The variational formulation of viscoplastic constitutive updates. *Comput. Meth. Appl. Mech. Eng.*, 171:419–444, 1999.

[39] N. Perrone and R. Kao. A general finite difference method for arbitrary meshes. *Comput. Struct.*, 5:45–58, 1975.

[40] R. Radovitzky and M. Ortiz. Error estimation and adaptive meshing in strongly nonlinear dynamic problems. *Comput. Meth. Appl. Mech. Eng.*, 172:203–240, 1999.

[41] V. T. Rajan. Optimality of the Delaunay triangulation in $\mathbb{R}^d$. *Discrete Comput. Geom.*, 12:189–202, 1994.

[42] P. W. Randles and L. D. Libersky. Smoothed particle hydrodynamics: Some recent improvements and applications. *Comput. Meth. Appl. Mech. Eng.*, 139:375–408, 1996.

[43] P. W. Randles and L. D. Libersky. Normalized SPH with stress points. *Int. J. Numer. Meth. Eng.*, 48:1445–1462, 2000.

[44] M. B. Rubin and A. L. Yarin. A generalized formula for the penetration depth of a deformable projectile. *Int. J. Impact Eng.*, 27:387–398, 2002.

[45] C. E. Shannon. A mathematical theory of communication. *Bell Sys. Tech. J.*, 27(3):379–423, 1948.

[46] J. E. Shore and R. W. Johnson. Axiomatic derivation of the principle of maximum entropy and the principle of minimum cross-entropy. *IEEE Trans. Inform. Theor.*, 26(1):26–36, 1980.

[47] J. Skilling. The axioms of maximum entropy. *In Maximum-Entropy and Bayesian Methods in Science and Engineering, Erickson GJ, Smith CR (eds), Foundations*, 1:173–187, 1988.

[48] N. Sukumar and R. W. Wright. Overview and construction of meshfree basis functions: From moving least squares to entropy approximants. *Int. J. Numer. Meth. Engng.*, 70:181–205, 2007.

[49] D. Sulsky, Z. Chen, and H. L. Schreyer. A particle method for history-dependent materials. *Comput. Meth. Appl. Mech. Eng.*, 118:179–186, 1994.

[50] J. W. Swegle. Smoothed particle hydrodynamics stability analysis. *J. Comput. Phys.*, 116:123–134, 1995.

[51] G. Taylor. The use of flat-ended projectiles for determining dynamic yield stress. I. theoretical considerations. *Proc. Roy. Soc. Lond. Math. Phys. Sci.*, 194:289–299, 1948.

[52] G. I. Taylor and H. Quinney. The plastic distortion of metals. *Philos. Trans. Roy. Soc. London*, 230:323–362, 1931.

[53] C. Villani. *Topics in optimal transportation theory, Graduate Studies in Mathematics*, volume 58. American Mathematical Society, Providence, Rhode Island, USA, 2003.

[54] J. D. Walker and C. E. JR. Anderson. A time-dependent model for long-rod penetration. *Int. J. Impact Eng.*, 16(1):19–48, 1995.

[55] Y. Y. Zhu and S. Cescotto. Unified and mixed formulation of the 4-node quadrilateral elements by assumed strain method: Application to thermomechanical problems. *Int. J. Numer. Meth. Eng.*, 38:685–716, 1995.